Towards superconducting spintronics with RuO2 and CrO2 nanowires
Prateek, K.

Towards Superconducting Spintronics
with
RuO$_2$ and CrO$_2$ Nanowires

Proefschrift

ter verkrijging van
de graad van doctor aan de Universiteit Leiden,
op gezag van rector magnificus prof.dr.ir. H. Bijl,
volgens besluit van het college voor promoties
te verdedigen op vrijdag 8 december 2023
klokke 11:15 uur

door

Kumar Prateek
geboren te Muzaffarpur, India
in 1986

Promotor:

Prof. dr. J. Aarts

Promotiecommissie:

Prof. dr. G. Koster	Universiteit Twente
Dr. C. Cirillo	Università degli Studi di Salerno, Italy
Prof. dr. K. E. Schalm	
Dr. K. Lahabi	
Prof. dr. S. J. van der Molen	

About the cover: The cover shows the SEM image of a CrO_2 based Jospehson junction device studied in thesis. The two arrows represent the equal spin triplet pairings.

Cover design: Kumar Prateek

To my grandparents

Contents

1

Introduction

Traditional electronic devices depend on the transport of electric charge carriers, specifically electrons, within a semiconductor such as silicon to perform their functions. Over the past five decades, there has been remarkable progress in semiconductor technology, characterized by significant advancements in performance and continuous efforts towards achieving greater miniaturization. Since the 1970s, there has been a trend observed in which the number of transistors in an integrated circuit (IC) doubles approximately every two years, an empirical observation that is commonly referred to as Moore's law. As the possibilities of silicon-based electronics reach their limits, physicists are actively exploring the potential of utilizing the inherent 'spin' property of electrons, in addition to their charge, to develop a new generation of devices known as 'spintronic' devices.

The term spintronics was first coined as an abbreviation for SPIN TRansport electrONICS. The origins of spintronics may be traced back to a series of discoveries and advancements in solid-state physics and electronics going even back to the 1970s, when Robert Meservey and Peter Tedrow conducted tunneling measurements on junctions between very thin superconducting aluminium films and ferromagnetic nickel films in a high magnetic field [1, 2]. Their experiments revealed a spin-dependent nature of the tunneling current. These experiments marked the first efforts to study spin-dependent electron transport phenomena. In 1975, Michel Julliere added to this groundwork by conducting initial experiments on magnetic tunnel junctions [3]. Another important milestone was the observation of spin-polarized electron injection from a ferromagnetic metal to a normal metal by Johnson and Silsbee in 1985 [4]. These early experiments laid the foundation for the development of spintronics. In 1988, Albert Fert and Peter Grünberg independently

discovered Giant Magnetoresistance [5, 6]. In the 1990s, research in the field expanded to include other spin-based phenomena such as tunnel magnetoresistance (TMR) [7–11] and the manipulation of the spin of individual electrons using the technique of spin injection. In 2007, researchers demonstrated efficient electrical spin injection from a ferromagnetic metal contact into silicon, producing a large electron spin polarization in the silicon [12, 13]. These developments led to the creation of new types of devices such as spin valves and magnetic tunnel junctions, which are now widely used in data storage applications such as hard disk drives.

Spintronics offers several advantages over traditional electronics, including energy efficiency, higher storage density, improved durability, versatility etc [14]. There is a variety of spintronic devices that exploit the spin of electrons to store and process information, such as Magnetic Random Access Memory (MRAM), Spin Transfer Torque Random Access Memory (STT-RAM) [15], Spin Hall Effect (SHE) devices [16], and Spin-Orbit Torque (SOT) devices [17]. In recent years, research in spintronics has focused on the development of new materials and devices with suitable magnetic properties, such as a high degree of spin polarization and a high Curie temperature (T_C) — the temperature above which the material ceases to be a ferromagnet - that can be used in a variety of applications beyond data storage, including high-speed computing, energy-efficient electronics, and quantum computing. Of particular interest are magnetic materials that exhibit a very high spin polarization at the Fermi level. Prominent example of such materials include metallic oxides such as CrO_2, $La_{0.3}Sr_{0.7}MnO_3$ (LSMO); and Heusler alloys with the general composition X_2YZ (X = Co, Fe, Y = Mn, Z = Al, Si, Ge, Al, Sb). These Half-metals (HM) are a special type of ferromagnet that display 100% spin polarization due to their band structure, with one spin channel exhibiting metallic behavior due to finite electron density of states at the Fermi level, while the other spin channel behaves as an insulator (or semiconductor) due to an energy gap[18].

While spintronics technology has the potential to revolutionize the field of electronics, there are several challenges that are currently holding back its commercial use. In particular one of the biggest challenges is the large amount of dissipation that is generated by current-driven processes at the nanoscale [19, 20]. To address some of these shortcomings, a new field has emerged which combines spintronics with superconductivity, giving rise to superspintronics. Superconductors are, by nature, dissipationless. We can have dissipationless spin polarized currents which can exploit the intrinsically low switching energies and high switching frequencies of spintronics. Moreover, it is of great interest for the possibility of introducing quantum coherence phenomena in spintronic devices. Traditionally considered competing phenomena, when artificially juxtaposed, a wealth of physics at the interface between superconductors and ferromagnets emerges. Spin-polarised Cooper

pairs are capable of surviving inside a ferromagnet over much longer distances than the regular (spin-singlet, anti-parallel) pairs. This new type of Cooper pair is the building block for super-spintronics; leading to a dissipationless spin-current combined with spintronic devices.

The idea of combining superconductivity and ferromagnetism was first discussed in the seminal work in 1956 by Ginzburg. His theoretical analysis revealed that suppression of superconductivity could happen due to so called orbital effect : in the presence of magnetic field, the Lorentz force is exerted differentially on two electrons with opposite spin in Cooper pair. Furthermore, the Zeeman interaction, which arises from the coupling between spins and a magnetic field, promotes a parallel alignment of the spins. This implies that when the magnetic field is sufficiently high, the pairs of electrons become energetically unstable because one electron in the pair will undergo a spin-flip scattering process. Although rare, some unconventional superconductors with coexisting ferromagnetic order have been found like UGe [21], URhGe [22] and UCoGe [23].

The coexistence of superconductivity and ferromagnetism can also be engineered using conventional superconductors (S) and a ferromagnet (F) to create S/F hybrids. Due to the exchange-field E_{ex} of F, the up-spin and down-spin electrons of a Cooper-pair acquire a phase difference upon passing through a S/F interface. Consequently, Cooper pairs arrange themselves in a so called FFLO (Fulde-Ferrel-Larkin-Ovchinnikov) state within F. The coexistence of the spin-singlet $|\uparrow\downarrow - \downarrow\uparrow\rangle$ and spin-triplet components $|\uparrow\downarrow + \downarrow\uparrow\rangle$, both with zero spin projection, is observed. This mixed state gives rise to novel physical phenomena. Nevertheless, it is limited to a few nanometers inside the ferromagnetic material, rendering it somewhat impractical for most applications. The typical length scale over which the superconducting state survives inside the ferromagnet is given by the coherence length (in dirty limit) [1], $\xi_F = \sqrt{\hbar D_F/E_{ex}}$ where, $\hbar$ is the reduced Planck's constant, D_F is the electronic diffusion constant in F and E_{ex} is the exchange energy.

There is a way to overcome this problem of short range superconductivity in the F layer by exploiting anti-symmetrical pairing of the wave function describing the Cooper pair in the time domain. Although a Cooper pair behaves as a boson, its fundamental constituents are fermions, and therefore obey Pauli's exclusion principle. This means that the total wave function, which is a product of the spatial-orbital part, spin part and time (or frequency) has to be antisymmetric under an overall exchange of two electrons. Basically, allowing uncertainty in time as well as in space, and allowing 'negative times' or frequencies, an extra symmetry can be built into the wave function : even in frequency yields conventional s- or d-wave

---

[1] in the dirty limit : $\xi_F < l_e$, where l_e is the mean free path of electron
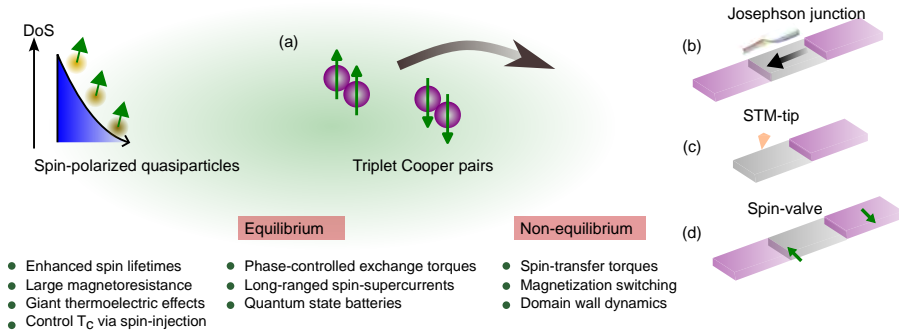
Figure 1.1: (a) Schematic overview of different ways to use superconducting spintronics by means of spin-polarized quasi-particles and triplet Cooper pairs, both in equilibrium and non-equilibrium settings. The fading colour of the quasi-particles in the superconducting region represents their loss of effective charge as they approach the gap edge. (b–d), Schematics for typical experimental set-ups used in superconducting spintronics, including Josephson junctions, bilayers and spin valves. [Taken from ref. [27]].

spin singlets ($|\uparrow\downarrow - \downarrow\uparrow\rangle$) and p-wave spin triplets ($|\uparrow\downarrow + \downarrow\uparrow\rangle$); while odd in frequency can yield s-type spin triplets ($|\uparrow\uparrow\rangle, |\downarrow\downarrow\rangle$) or p-type spin singlets. The p-wave pairing is very sensitive to any external impurities or disorder and hence, is short-range in nature. However, s-type pairing does not suffer from any such limitations. These odd-frequency equal-spin pairing can coexist with a magnetic field as the Zeeman interaction due to the magnetization no longer has a pair-breaking effect. In other words, these triplets and the ensuing supercurrents can have a very long range, mainly determined by the temperature and by spin scattering.

The odd-frequency pairing in a ferromagnet was first outlined in two seminal papers by Bergeret et al. [24] and Kadigrobov et al. [25] in 2001. Crucial in converting s-wave singlet pairs in the superconductor to s-wave triplets in the ferromagnet is the engineering of well-defined magnetic inhomogeneity (the 'generator') at the interface with the superconductor. This was demonstrated experimentally by Keizer et al. on the half-metal CrO_2 films over distances up to 1 μm in 2006 [26]. Since the triplets supercurrents are by definition spin-polarized, they offer great potential for a new kind of superconducting electronics, in which not only the charge and the superconducting phase, but also the spin is utilised. Some of the possible area of applications of superconducting electronics as shown in Fig.1.1 include magnetization switching, magnetization precession, spin-transfer torque, or domain wall motion due to spin-polarized supercurrents; injection of spin-triplet pairs into superconductors, superconducting spin valves; Josephson φ-junction for phase batteries; and Josephson diodes. The major perspective and challenge here is to develop a framework for nonequilibrium transport that can account for dynamic interactions involving spin-triplet pairs and ferromagnetic layers.

1.1. Outline of this thesis

This thesis is concerned with whether and how in particular the half-metal CrO_2, with its full spin polarization, can be utilized as a building block in superspintronics. For this we study the epitaxial growth of CrO_2 and RuO_2 nanowires and investigate their transport properties under the influence of magnetic field. Further, Josephson Junctions devices were fabricated using these wires and it was attempted to find long range supercurrents, in particular in CrO_2. The thesis is structured as follows:

- **Chapter 2** consists of two parts. The first part of this chapter treats the necessary concepts of superconductivity and gives the background on long range spin triplet superconductivity and Josephson physics. In the second part, we introduce the various individual energy contributions that lead to the magnetization state of a ferromagnet, and in competition result in the spontaneous formation of domain walls (DWs) in magnetic materials. Different types of DWs can occur, that are based on the geometry and size. We also introduce the basics of magnetization dynamics through the Landau-Lifshitz-Gilbert equation that describes the dynamic behavior of magnetic moments under the influence of magnetic fields and currents.

- **Chapter 3** describes the selective area growth of CrO_2 nanowires on a TiO_2 substrate along both the substrate c-axis (easy axis) and the substrate b-axis (hard axis). We investigate the morphology of these nanowires by high-resolution transmission electron microscopy (TEM) and measure their transport properties, in particular magnetoresistance (MR) and the Anomalous Hall Effect (AHE). TEM images show the difference in morphology of the wires grown along the two axes, which is supported by the MR measurements.

- **Chapter 4** focuses on the pulse measurements on CrO_2 nanowires with the purpose of removing a domain wall from an artificially made constriction in the wire. For this we design a high frequency pulse setup and then use Py wires to develop and optimize the setup to study current driven DW motion. Then we demonstrate current induced DW motion in CrO_2 in the same setup. We show that the critical depinning current in CrO_2 is comparable to Py despite the high spin polarization of the former, and show it to be very sensitive to small changes in magnetic field and the dimension of the constriction (a 'notch').

- **Chapter 5** studies the growth of RuO_2 nanowires followed by characterization of these wires through electrical and magnetotransport measurements. Then we focus on making Josephson junctions (JJs) in which superconducting MoGe are contacted on top of RuO_2 nanowires with varying lateral gaps and present the results on these junctions. From the data, we extract the coherence length of the superconducting correlations in the RuO_2 wire.

- **Chapter 6** presents the nanofabrication of Josephson Junctions using CrO_2 nanowires. Two approaches were used to make these devices. We start with using the traditional etching of insulating Cr_2O_3 on CrO_2 surface before depositing tri-layer contact (Ag/Ni/MoGe). The interface transparency is studied systematically by varying the etch times on multiple samples (> 50). Despite multiple attempts, we did not succeed in producing the required high transparency. In the second method, RuO_2 is deposited in-situ with CrO_2 to protect the surface of CrO_2 before depositing Ni/MoGe contacts and the results on these junctions are discussed.

References

[1] Tedrow, P. M. & Meservey, R. Spin-dependent tunneling into ferromagnetic nickel. Phys. Rev. Lett. **26**, 192–195 (1971). URL https://link.aps.org/doi/10.1103/PhysRevLett.26.192.

[2] Tedrow, P. M. & Meservey, R. Spin polarization of electrons tunneling from films of Fe, Co, Ni, and Gd. Phys. Rev. B **7**, 318–326 (1973). URL https://link.aps.org/doi/10.1103/PhysRevB.7.318.

[3] Julliere, M. Tunneling between ferromagnetic films. Physics Letters A **54**, 225–226 (1975). URL https://www.sciencedirect.com/science/article/pii/0375960175901747.

[4] Johnson, M. & Silsbee, R. H. Interfacial charge-spin coupling: Injection and detection of spin magnetization in metals. Phys. Rev. Lett. **55**, 1790–1793 (1985). URL https://link.aps.org/doi/10.1103/PhysRevLett.55.1790.

[5] Baibich, M. N. et al. Giant Magnetoresistance of (001)Fe/(001)Cr Magnetic Superlattices. Phys. Rev. Lett. **61**, 2472–2475 (1988). URL https://link.aps.org/doi/10.1103/PhysRevLett.61.2472.

[6] Binasch, G., Grünberg, P., Saurenbach, F. & Zinn, W. Enhanced magnetoresistance in layered magnetic structures with antiferromagnetic interlayer exchange. Phys. Rev. B **39**, 4828–4830 (1989). URL https://link.aps.org/doi/10.1103/PhysRevB.39.4828.

[7] Gubkin, M., Perekalina, T., Bykov, A. & Chubarenko, V. Investigation of the electrical conductivity of some manganites with the perovskite structure. Physics of the solid state **35**, 728–730 (1993).

[8] Inoue, J. & Maekawa, S. Theory of tunneling magnetoresistance in granular magnetic films. Phys. Rev. B **53**, R11927–R11929 (1996). URL https://link.aps.org/doi/10.1103/PhysRevB.53.R11927.

[9] Hwang, H. Y., Cheong, S.-W., Ong, N. P. & Batlogg, B. Spin-Polarized Intergrain Tunneling in $la_{2/3}sr_{1/3}mno_3$. Phys. Rev. Lett. **77**, 2041–2044 (1996). URL https://link.aps.org/doi/10.1103/PhysRevLett.77.2041.

[10] Kimura, T. et al. Interplane tunneling magnetoresistance in a layered manganite crystal. Science **274**, 1698–1701 (1996). URL https://www.science.org/doi/abs/10.1126/science.274.5293.1698.

[11] Sun, J. Z. et al. Observation of large low-field magnetoresistance in trilayer perpendicular transport devices made using doped manganate perovskites.

Applied Physics Letters **69**, 3266–3268 (1996). URL https://doi.org/10.1063/1.118031. https://pubs.aip.org/aip/apl/article-pdf/69/21/3266/11582817/3266_1_online.pdf.

[12] Jonker, B. T., Kioseoglou, G., Hanbicki, A. T., Li, C. H. & Thompson, P. E. Electrical spin-injection into silicon from a ferromagnetic metal/tunnel barrier contact. Nature Physics **3**, 542–546 (2007). URL https://doi.org/10.1038/nphys673.

[13] Appelbaum, I., Huang, B. & Monsma, D. J. Electronic measurement and control of spin transport in silicon. Nature **447**, 295–298 (2007). URL https://doi.org/10.1038/nature05803.

[14] Žutić, I., Fabian, J. & Das Sarma, S. Spintronics: Fundamentals and applications. Rev. Mod. Phys. **76**, 323–410 (2004). URL https://link.aps.org/doi/10.1103/RevModPhys.76.323.

[15] Ralph, D. & Stiles, M. Spin transfer torques. Journal of Magnetism and Magnetic Materials **320**, 1190–1216 (2008). URL https://www.sciencedirect.com/science/article/pii/S0304885307010116.

[16] Hirsch, J. E. Spin Hall Effect. Phys. Rev. Lett. **83**, 1834–1837 (1999). URL https://link.aps.org/doi/10.1103/PhysRevLett.83.1834.

[17] Liu, L. et al. Spin-torque Switching with the Giant Spin Hall Effect of Tantalum. Science **336**, 555–558 (2012). URL https://www.science.org/doi/abs/10.1126/science.1218197.

[18] de Groot, R. A., Mueller, F. M., Engen, P. G. v. & Buschow, K. H. J. New class of materials: Half-metallic ferromagnets. Phys. Rev. Lett. **50**, 2024–2027 (1983). URL https://link.aps.org/doi/10.1103/PhysRevLett.50.2024.

[19] Slonczewski, J. Current-driven excitation of magnetic multilayers. Journal of Magnetism and Magnetic Materials **159**, L1–L7 (1996). URL https://www.sciencedirect.com/science/article/pii/0304885396000625.

[20] Huai, Y., Albert, F., Nguyen, P., Pakala, M. & Valet, T. Observation of spin-transfer switching in deep submicron-sized and low-resistance magnetic tunnel junctions. Applied Physics Letters **84**, 3118–3120 (2004). URL https://doi.org/10.1063/1.1707228. https://pubs.aip.org/aip/apl/article-pdf/84/16/3118/10203727/3118_1_online.pdf.

[21] Saxena, S. et al. Superconductivity on the border of itinerant-electron ferromagnetism in UGe_2. Nature **406**, 587–592 (2000).

References

[22] Aoki, D. et al. Coexistence of superconductivity and ferromagnetism in URhGe. Nature **413**, 613–616 (2001).

[23] Huy, N. T. et al. Superconductivity on the border of weak itinerant ferromagnetism in UCoGe. Phys. Rev. Lett. **99**, 067006 (2007). URL https://link.aps.org/doi/10.1103/PhysRevLett.99.067006.

[24] Bergeret, F. S., Volkov, A. F. & Efetov, K. B. Long-Range Proximity Effects in Superconductor-Ferromagnet Structures. Phys. Rev. Lett. **86**, 4096–4099 (2001). URL https://link.aps.org/doi/10.1103/PhysRevLett.86.4096.

[25] Kadigrobov, A., Shekhter, R. & Jonson, M. Quantum spin fluctuations as a source of long-range proximity effects in diffusive ferromagnet-super conductor structures. Europhysics Letters **54**, 394 (2001).

[26] Keizer, R. S. et al. A spin triplet supercurrent through the half-metallic ferromagnet CrO_2. Nature **439**, 825–827 (2006). URL https://doi.org/10.1038/nature04499.

[27] Linder, J. & Robinson, J. W. Superconducting spintronics. Nature Physics **11**, 307–315 (2015).

2

Long Range Proximity Effects & Domain Wall Physics

This is Chapter 2, which gives an overview over some of the fundamental concepts to be appreciated in the context of this Thesis.

2.1. Introduction

As was already mentioned in Chapter 1, the major motivation to work on CrO_2 and RuO_2 nanowires lies in the fact that CrO_2 is a half-metallic ferromagnet, a class of materials that is uniquely suited to studying superconducting long range proximity effects and spin-polarized supercurrents. Even though this research was not successful, it is fitting to briefly reiterate the framework of the research question on the superconducting side, discuss some basic aspects of superconducting Josephson junctions, and mention what appeared to be the state of the art when the research started. This will be the first part of this Chapter. Then, for the final goal of having supercurrents interact with magnetic structures such as nanomagnets or domain walls (DWs), this Thesis presents results on the magnetic behavior of CrO_2 nanowires, and on pinning and depinning of DWs from constrictions in such nanowires. Some basic notions of magnetism and DW formation are therefore presented in the second part of this Chapter.

2.2. Superconductivity

2.2.1. General concepts

Superconductors are materials that transport electric charge without resistance. It is a so-called macroscopic quantum phenomenon, displaying, for instance, spontaneous flux expulsion and magnetic flux quantization. These quantum phenomena are associated with macroscopic wave functions characteristic of off-diagonal long-range order (ODLRO), a concept first introduced by Yang [1]. This order is characterized by a long-range coherence of the quantum mechanical phase which demonstrates itself in the form of macroscopic quantum phenomena. As a consequence of macroscopic occupation, a simple wave function Ψ can describe the whole superconducting state :

$$\Psi(r, t) = \sqrt{n_s(r, t)} e^{i\theta(r,t)} \tag{2.1}$$

where, n_s is the density of Cooper pairs and θ is the gauge covariant phase. $n_s = n_e/2$, where n_e is the normal electron density. A basic parameter characterizing a superconductor is the Ginzburg-Landau coherence length ξ_{GL}, which determines the distance over which the density of superconducting carriers can meaningfully change. The size of ξ_{GL} can vary from several tens of nm in metallic superconductors down to about 1 nm in the 'high critical temperature (T_c)' copper-oxide superconductors (HTS). The other important length scale is the London penetration depth λ_L which describes the decay of an external magnetic field from the edge of a superconductor toward its interior, from which it is ultimately
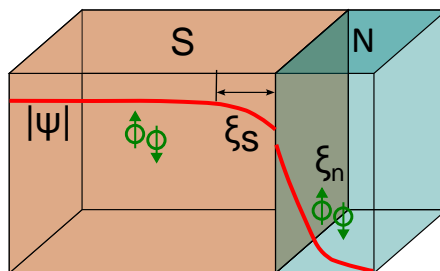
Figure 2.1: Schematic representation of the proximity effect between a superconductor (S) and a normal metal (N). The superconducting order parameter decays over the length scales ξ_S and ξ_N as it extends across the interface. The discontinuity of the order parameter at the interface signifies a non-perfect interface transparency.

expelled. The ratio ($\kappa = \lambda_L/\xi_{GL}$) between these two lengths bifurcates between two types of superconductors, type I, where flux expulsion below T_c is complete, and type II, where flux quanta (vortices) can remain present in the bulk of the material. Both ξ_{GL} and λ_L are temperature dependent. According to Ginzburg-Landau theory, $\xi_{GL}(T) = \xi_{GL}(0)(1 - T/T_c)^{-1/2}$, which implies a diverging enhancement of $\xi_{GL}(T)$ from its minimal value $\xi_{GL}(0)$ at T = 0 when T_c is approached. Similarly, $\lambda_L(T) = \lambda_L(0)(1 - (T/T_c)^4)^{-1/2}$. For λ_L, it is important to know that for film thicknesses $t \leq \lambda_L(T)$, $\lambda_L(T)$ has to be replaced by an effective penetration depth (also called Pearl length) $\Lambda(T) = 2\lambda_L(T)^2/t$.

2.2.2. Proximity effect with normal metals

In a superconductor (S) the electrons are ordered as Cooper pairs whereas in a normal metal (N), the electron arrangement lacks such pairing and is instead characterized by a continuous distribution of single-electron states that are filled up to the Fermi surface. When S is placed next to N, the electron ordering in the two systems does not undergo an instantaneous change at the interface, rather it happens over a finite distance. The characteristic length scale ξ over which the order parameter can change its magnitude is called the coherence length, which is a material property. At the side of N, an often-used picture is that Cooper pairs are carried over ('leak') into the metal and that their density decays over a length ξ_n (see Fig. 2.1). In a diffusive system, defined by $\xi_N < l_e$, where l_e is the electronic mean free path, ξ_N is given by

$$\xi_N = \sqrt{\frac{\hbar D_n}{k_B T}} \tag{2.2}$$
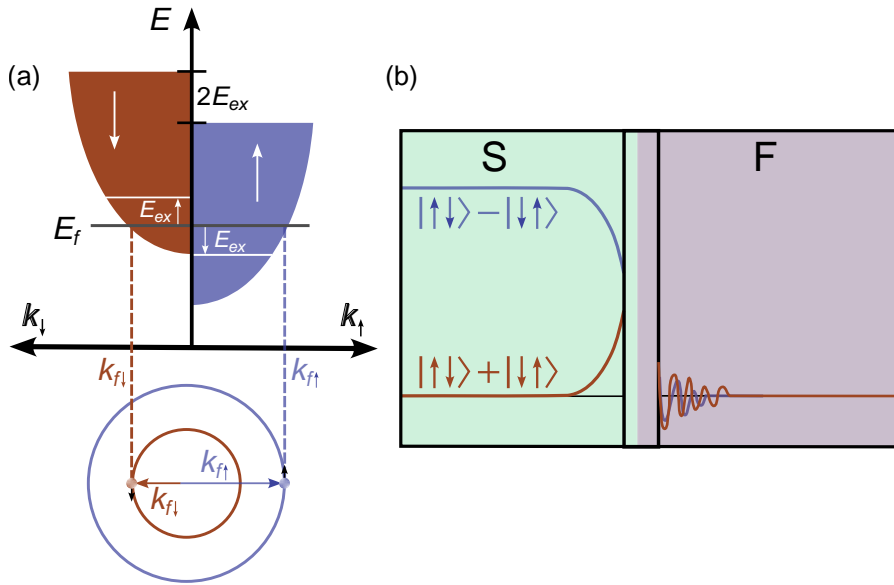
Figure 2.2: (a) Schematic representation of the electronic band structure for a ferromagnet. At S/F interface singlets have to adjust to Fermi energy E_F resulting in finite momentum. (b) Singlet (blue)-triplet (brown) mixing at S/F interface. Due to E_{ex} the correlations decay over very short distances resulting in short range proximity effect. The reflections from F layer cause spin-dependent phase shifts at S-side. Adapted from [2].

where $\hbar$ is reduced Planck constant, D_n is the diffusion coefficient of the metal, and k_B is the Boltzmann constant. ξ_N can be of the order of hundreds of nm. At the S side : As shown in Fig. 2.1 near the interface, the order parameter is depleted over a distance defined by $\xi_S(T)$, where $\xi(0)$ is the coherence length of S at T = 0 K. Therefore, the proximity effect is used to describe the induced superconductivity in a normal metal. Since the total condensate remains conserved, the Cooper pairs are "drained" from S which results in a suppression of T_c of the superconductor. We note in passing that there is another way to look at the superconducting correlations on the N-side of the interface, using the concept of Andreev reflections. In that language, the coherence on the N-side is rather furnished by an electron with a certain spin, coupled to a 'retroreflected hole' of opposite spin. Both pictures allow to discuss the coupling of two superconductors in an S/N/S geometry.

2.2.3. Proximity effect with ferromagnets

If the non-S metal is a ferromagnet (F) instead of a normal metal, several details change in the picture of the proximity effect. As previously mentioned in Ch. 1, the

exchange field E_{ex} of F splits the band structure for up and down spins, resulting in an energy shift of $2E_{ex}$. The singlet Cooper pairs consist of two electrons with equal and opposing momentum (k_F, -k_F) and spin ($\uparrow$, $\downarrow$). E_{ex} induces a momentum shift of $\pm\mathbf{Q}/2$ for electrons located at the Fermi level. In the diffusive limit $Q = 2E_{ex}/\hbar v_F$, where v_F is the Fermi velocity. As a result, a finite momentum for $|\uparrow\downarrow\rangle$ may be expressed as $\mathbf{k}_{F\uparrow}$ - $\mathbf{k}_{F\downarrow} = \mathbf{Q}$, and for $|\downarrow\uparrow\rangle$ is $\mathbf{k}_{F\downarrow}$ - $\mathbf{k}_{F\uparrow} = -\mathbf{Q}$. This results in singlet Cooper pairs at the Fermi energy E_F acquiring a non-zero center-of-mass momentum. Consequently, a spin-mixed state emerges:

$$|\uparrow\downarrow - \uparrow\downarrow\rangle \implies |\uparrow\downarrow\rangle e^{i\mathbf{Q}\cdot\mathbf{R}} - |\downarrow\uparrow\rangle e^{i\mathbf{Q}\cdot\mathbf{R}} = |\uparrow\downarrow - \uparrow\downarrow\rangle\cos(\mathbf{Q}\cdot\mathbf{R}) + i|\uparrow\downarrow + \uparrow\downarrow\rangle\sin(\mathbf{Q}\cdot\mathbf{R}) \quad (2.3)$$

The first component represents a zero-spin oscillating singlet state ($S = 0$ while the second term defines a triplet state ($S = 1$) with a spin projection ($m_s = 0$) relative to the spin quantization axis, determined by the E_{ex}. These correlations can only persist in the F layer within a certain length scale from the interface. The decoherence length ξ_F over which all pair amplitudes decay exponentially is expressed as

$$\xi_F = \sqrt{\frac{\hbar D_F}{E_{ex}}} \quad (2.4)$$

in a diffusive limit. For a conventional F like Co, Ni ξ_F is only a few nm. For a 100% spin polarized material such as CrO_2, only one spin band is occupied at E_F in which case the singlets cannot be injected at all. In terms of Andreev reflections, there is no retroreflected hole with opposite spin available. As a consequence, the S/F interface is fully reflective and ξ_F is of the order of atomic distances. At the S side of the interface, stronger spin polarization of F causes a spin-dependent phase shifts ($\pm\theta$), forming a spin triplet mixture ($m_s = 0$) in S which increases with the spin polarization. E_{ex} results in different scattering phase delay which can be expressed as

$$|\uparrow\downarrow\rangle e^{i\theta} - |\downarrow\uparrow\rangle e^{i\theta} = |\uparrow\downarrow - \uparrow\downarrow\rangle\cos(\theta) + i|\uparrow\downarrow + \uparrow\downarrow\rangle\sin(\theta) \quad (2.5)$$

The oscillating dependence of the order parameter on the distance from S/F interface has an interesting implication: there is the possibility of a 0-π transition by varying the thickness of F layer [3, 4] or changing the temperature [5]. However, the short range of a few nm of the spin mixed state in F limits the development of applications.

2.2.4. Equal spin triplets and the Long-range proximity effect

The proximity effect in S/F hybrids is not restricted to short ranges. The quantization axis of correlations with zero spin projection can be rotated to produce alternative (equal spin) triplet correlations with $m_s = 1$(or -1). A ferromagnet does not break
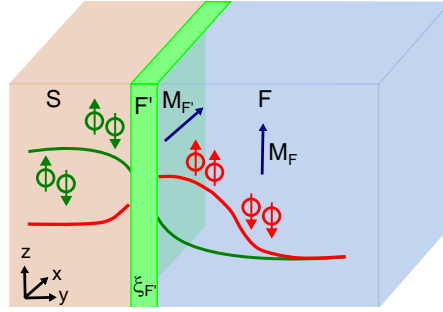
Figure 2.3: (a) Schematic representation of long range proximity effect in a S/F'/F hybrid. When magnetization of F' is non-collinear with F, the $m_s = 0$ triplet is rotated in the spin space and converted into equal spin triplet ($m_s = 1$). when $M_{F'}$ is $\perp$ to M_F singlet to triplet conversion is optimized. Equal spin pairs are not broken by E_{ex} and can exist up to hundreds of nm in F layer.

up equal spin triplets, denoted as $|\uparrow\uparrow\rangle$ and $|\downarrow\downarrow\rangle$ in Dirac notation. The rotation can come about by introducing magnetic non-collinearity or inhomogeneity at the S/F interface. One way to do that is by stacking a thin layer (within length ξ_F) of a magnetic material F' with a different magnetization direction than F (see Fig. 2.3) [6, 7]. For instance, we assume $M_{F'}$ to align with the x-axis while M_F is along z. The spin mixing in S due to F' is then a consequence of E_{ex} along x. The magnetization of spin mixing correlations gets rotated to z. The triplet state ($m_s = 0$) has zero-spin projection along x but it can have non-zero component $|\uparrow\uparrow\rangle_z$ and $|\downarrow\downarrow\rangle_z$ along z. The amount of spin polarization of F and the degree of magnetic inhomogeneity defines the relative amplitude of the two components. In case of half-metals, one of the two is completely suppressed. Due to their equal spins, the triplets are not affected by E_{ex} and therefore can stay coherent over large distance, similar to singlets in a normal metal, resulting in a Long Range Proximity effect. The main limiting factor here is the spin diffusion length, while the characteristic decay length is given by

$$\xi_F^T = \sqrt{\frac{\hbar D_F}{k_B T}} \qquad (2.6)$$

In conventional F metals, ξ_F^T can be tens of nanometers. However for 100% spin polarized F like CrO_2 spin flipping is not an issue and ξ_F^T can be several hundreds nanometers. The equal spin triplet supercurrents are by definition spin-polarized. They offer great potential for the development of superconducting electronics wherein not only the charge and the superconducting phase, but also the spin is utilised. The primary focus of our study revolves around two systems, namely Josephson junctions and triplet spin valves. In the following sections an overview of the general Josephson effect is given prior to the examination of earlier studies on proximity effects.
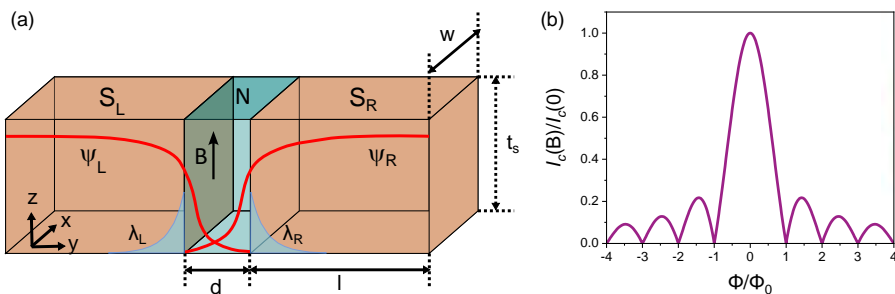
Figure 2.4: (a) Schematic representation of a Josephson junction : Two superconducting (S) electrodes (orange) separated by a thin weak link (blue) of length d. The amplitude of two superconducting wave functions (red) is shown to be overlapping, resulting in a supercurrent through the junction. The dimensions of the superconductors are : width (w), thickness (t_s), length (l). The magnetic field is applied along the z-axis and the current flow is along the y-axis. The magnetic field penetrates into S and decays exponentially over the London penetration depth (λ_L, λ_R).(b) The Fraunhofer-like interference pattern of the critical current I_c in a JJ due to the applied field, in units of flux normalized by the flux quantum. The central peak is two times wider than the side lobes, and the side lobe maxima decay as $1/B$.

2.2.5. Josephson junctions

The Josephson effect in general describes the transfer of Cooper pairs and the coupling of the macroscopic wave functions between two superconductors via a weak link. The nature of the weak link determines the transport through the junction and can be insulating (I), a normal metal (N) or a ferromagnet (F). A schematic of such a geometry is given in Fig. 2.4(a) which shows two superconducting electrodes, each corresponding to a distinct wave function described by $\Psi_{L,R} = \sqrt{n_{s_{L,R}}}e^{i\theta_{L,R}}$ separated by a thin N layer such that the two wave functions overlap and maintain coherence. We assume that the density of Cooper pairs (n_s) stays the same in both the electrodes. The phase difference φ between the two condensates is given by $\theta(L) - \theta(R)$, where $\theta(L, R)$ corresponds to the phase of the individual condensates. Supercurrents in the weak link are driven by the phase difference and can be expressed as

$$J = J_c \sin(\varphi) \tag{2.7}$$

J_c is the maximum current density the junction can sustain. Above this current, the junction returns to the normal resistive state and a finite voltage is measured. The sinusoidal current-phase relation reveals the wave-like nature of the charge transport in a superconductor. The manifestation of quantum behavior becomes more apparent when a magnetic field is applied in a direction perpendicular to the current. Experimentally, it results in a "Fraunhofer"-like diffraction pattern (see Fig. 2.4(b)) similar to the diffraction pattern observed when a wave passes through a single slit. It is also called as superconducting quantum interference (SQI) pattern. When an external field is applied, the vector potential interacts with the

supercurrent, resulting in the introduction of an additional phase difference that is proportional to the strength of the field. The critical current exhibits oscillatory behavior when the field is increased due to the periodicity of the phase, superimposed on the decay due to orbital breaking effect. The periodicity of the oscillation is equal to $\Delta B = \Phi_0 / A$, where Φ_0 is the magnetic flux quantum and A is the effective junction area, given by $(\lambda_L + \lambda_R + d) w$ (see Fig. 2.4(a)), penetrated by the flux (Φ). The SQI is described by

$$\frac{I_c(B)}{I_c(0)} = \left| \frac{\sin(\frac{\pi \Phi}{\Phi_0})}{\frac{\pi \Phi}{\Phi_0}} \right| \qquad (2.8)$$

It should be noted that the periodicity of SQI is dependent on the size of the superconductor. The above discussion holds true under the condition that the thickness t of S is larger than the London penetration depth λ. As discussed in the previous sec. 2.2 (and shown in Fig. 2.4(a)) the magnetic field applied along the z axis decays in both right and left superconducting electrodes over λ. In particular, junction physics becomes different when the thickness of the superconducting electrodes is less than λ. Additionally, when the junction width w becomes smaller than the Josephson penetration length ℓ_J given by

$$\ell_J = \frac{\Phi_0}{4\pi \mu_0 \lambda^2 J_c(0)} \qquad (2.9)$$

with J_c being the (presumed homogeneous) critical current density of the junction. The shielding current running along the junction, responsible for the shape and periodicity of SQI is no longer determined by Meissner effect. In this scenario, as has been discussed in numerous studies, the electrodynamics becomes non-local, and $I_c(B)$ becomes independent of λ and is solely determined by the geometry of the device [8–12]. In particular, when $l >> w$ then $\Delta B = 1.84\Phi_0 / w^2$ and when $l << w$ then $\Delta B = 2\Phi_0 / (l \cdot w)$.

2.2.6. Earlier work on proximity effect in CrO_2

A first experimental breakthrough in long-range effects came in 2006, when Keizer et al. reported a Josephson supercurrent between two singlet superconducting electrodes (NbTiN) separated by (0.3- 1) μm of CrO_2 film[13]. The half-metallic nature of CrO_2 completely suppresses the Andreev reflections, hence preventing the penetration of singlet Cooper pairs, and the supercurrent was strong evidence for the LRP effect. They found a critical current density of the order of 5×10^9 A/m^2 and also observed SQI when an in-plane transverse field to the current was applied. Their experiments however, did not provide information about the pairing symmetry of the correlations. Furthermore, they reported large spread in their critical currents which suggests that the triplet generator was poorly defined and controlled.
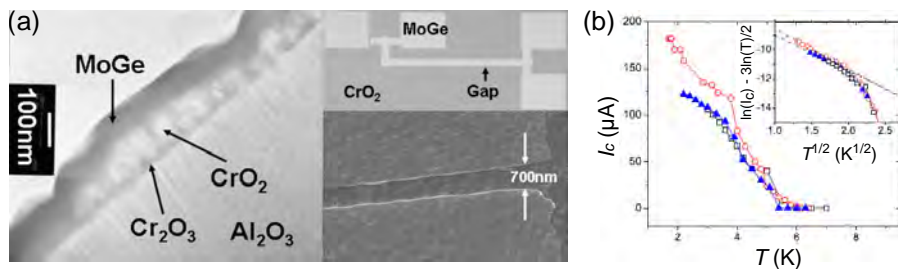
Figure 2.5: (a) (left) Transmission electron microscopy image of a CrO_2 film grown on Al_2O_3. Visible are the Cr_2O_3 seed layer, the CrO_2 layer, and the MoGe layer. (right) Layout of the device structure with four current/voltage contacts. The width of the electrodes is 30 μ m. SEM image of the gap between the two electrodes of 700 nm, made by liftoff. (b) Critical current I_c versus temperature T for three different junctions. The inset shows a linear fit to a plot of $\ln I_c - 3/2 \ln T$ vs $\sqrt{T}$. Taken from Ref. [14].

In 2010, Anwar et al. were able to successfully replicate the effect using MoGe electrodes separated by 700 nm on CrO_2 film grown on a Al_2O_3 substrate [14]. They observed supercurrents of the order of 10^7 A/m^2, lower by two order of magnitude compared to the previous study. Furthermore, it was estimated that the supercurrents were limited to a thickness of around 30 nm out of 100 nm of CrO_2 film resulting in a weaker junction. It was argued, supported by TEM images (see Fig. 2.5(a)), that the growth of CrO_2 films on Al_2O_3 leads to significant differences in film morphology: growth on Al_2O_3 does not start as CrO_2, but rather as Cr_2O_3 and only after a few tens of nanometers, the growing film becomes CrO_2.

One way to estimate the strength of a junction is by measuring the critical current I_c as a function of temperature. In a diffusive limit, for a long junction $I_c \propto T^{3/2} e^{\sqrt{(2\pi K_B T)/E_{Th}}}$, with E_{Th} the Thouless energy. Their junction showed good compliance at low temperatures up to 2 K (see Fig. 2.5(b)) with values of E_{Th} around 72 μV. However, no clear Fraunhofer pattern was observed when an in-plane magnetic field is applied parallel to the I_c. Furthermore, I_c showed little sensitivity to applied fields up to 500 mT which suggested that the non-collinear magnetic moments responsible for triplet generation are pinned at the CrO_2 interface. The authors also found a high normal state resistance R_N of 11 Ω instead of expected value of 4 mΩ which pointed to a low transparency of the S/F interface. This was due to the fact that CrO_2 is metastable and reduces to Cr_2O_3 at room temperature. This forms an insulating layer and has to be Ar-etched away before the superconducting electrodes are deposited. The Ar etching will not only remove unwanted oxides but may also damage the surface.

Overall, the complicated fabrication process to get the desired interface transparency and the lack of control over magnetization at the interface with CrO_2 films
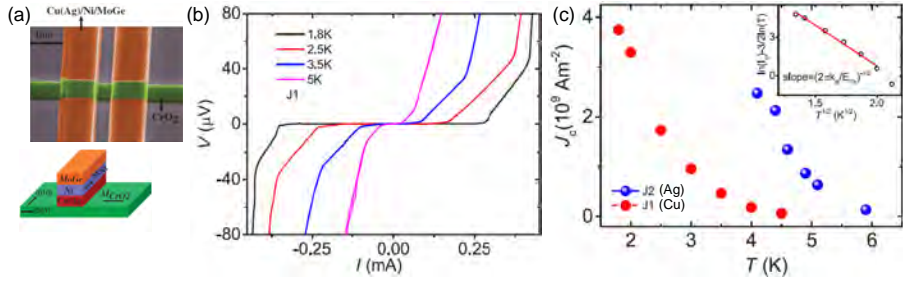
Figure 2.6: (a) Scanning electron micrograph (false color) of a Josephson junction on a CrO2 nanowire (green), Orange contact pads consist of trilayer (Cu or Ag)/Ni/MoGe. (top). Schematic of the device with CrO_2 wire as a weak link. (b) Current I versus voltage V characteristics of J1 at different temperatures. (c) Critical current density Jc vs T. The inset shows a linear fit to a plot of $\ln I_c - 3/2 \ln T$ vs $\sqrt{T}$. Taken from Ref. [16].

revealed the some of the limitations of these junctions. Consequently, the proportion of fabricated junctions exhibiting supercurrents falls below 30%.

In 2012 Anwar et al. improved on their previous work and reported supercurrents on CrO_2 films grown on TiO_2 substrates by employing a sandwich layer of Ni/Cu between the CrO_2 film and superconducting MoGe [15]. Adding a thin ferromagnetic layer of Ni layer provided the necessary magnetic inhomogeneity for triplet generation similar to the model proposed by Houzet and Budzin[6]. They observed an I_c of the order of 10^9 A/m^2, comparable to ref. [13] and two order of magnitude more than junctions on Al_2O_3 substrates. However, other issues like no clear Fraunhofer pattern in the presence of an external field, non-zero I_c at fields of 500 mT suggesting that the lack of control of magnetization at the interface and low interface transparency still remained.

So far, the studies were conducted on 'full-film' devices which, as we discussed, suffer from limitations due to presence of grain boundaries, ill-defined current paths and an lack of control of the magnetization state at the local level. In 2016, Singh et. al. reported selective area grown CrO_2 nanowires based lateral JJs[16]. Similar to the above studies, artificial magnetic homogeneity was provided by a sandwich layer of Cu (or Ag)/Ni at the interface of CrO_2 and MoGe (see Fig. 2.6(a)). It was observed that these junctions could also sustain supercurrents of the order of 10^9 A/m^2 below 5 K for a junction length of 500 nm. Furthermore, the junctions which used Ag (J2) instead of Cu (J1) had a larger critical current density (see Fig. 2.6(c)). It was postulated that the observed improvement in performance can be attributed to the increased interface transparency resulting from the use of Ag which, unlike Cu, does not undergo oxidation at the contact with CrO_2. The Thouless energy was estimated to be around 11 μV from the slope of plot (inset Fig. 2.6(c)), which was in good agreement with the calculated value of 15 μV using the relationship $E_{Th} = \hbar D / L^2$

where, diffusion constant D = 3.7×10^{-3} m^2/s and junction length L = 400 nm.

It can be concluded from these studies that selective area growth of CrO$_2$ nanowires with a well defined geometry and magnetization allows to overcome some of the issues of earlier studies on films. The estimated current densities are large enough to envision devices where such spin-polarized supercurrents could be used to manipulate the magnetization of a nanomagnet [17]. This forms the motivation behind the current work.

2.3. Magnets and magnetic domains

2.3.1. A magnetized object: The Landau free energy

Magnetic materials, such as ferromagnets, ferrimagnets, etc., contain regions where spins cluster to create uniform magnetization. These regions, known as magnetic domains, were first postulated by Weiss to explain extremely high permeability in the ferromagnets [18]. The development of the Weiss molecular field, which is actually a manifestation of the exchange interaction, was part of the solution, while the other part was the assumption that the sample was divided into multiple fully magnetized regions, called magnetic domains. The presence of magnetic domains was first suggested by the experimental work of Barkhausen [19] but it was confirmed later by Sixtus and Tonks [20] and Bitter [21]. Later, in 1935, Landau and Lifschitz proposed that the formation of magnetic domains in ferromagnetic materials helps to minimize the magnetostatic energy [22], along with the domain wall profile which was an improvement on Bloch [23] and Heisenberg work [24]. The fundamental concepts of magnetic domains were reviewed by Kittel [25], and later Hubert and Schäfer [26] extended the theory beyond the magnetostatic energy to include additional energy components.

The competition between the different energy terms that describe a magnetic object provides the physical foundation for domain formation. The sum of the individual energy contributions is the Landau free energy (G_L), given by the sum of the exchange energy E_{ex}, the Zeeman energy E_Z, the anisotropy energy E_{aniso} and the magnetostatic energy (also called the magnetostatic self-energy) E_{ms} [27]

$$G_L = E_{ex} + E_Z + E_{aniso} + E_{ms} \qquad (2.10)$$

As with all physical systems, the magnetic system seeks to minimize this Landau free energy. Since the magnitude of the magnetization vector is fixed, its direction must be changed. To determine the magnetization direction with the lowest total energy, a compromise must be reached between these energy terms. Consequently, some spins will no longer be pointing along this optimal direction. Typically, a uniformly

magnetized state has a high magnetostatic energy (Fig. 2.7(a)) (Fig. 2.7(a)), which can be reduced by forming a non-uniform or even flux-closed magnetic state (Fig. 2.7(b-d)). The formation of domains continues until the decrease in magnetostatic energy is balanced by the exchange and anisotropy energy costs, accompanied by magnetic structure twists and deviations. If an external magnetic field is applied, the Zeeman energy also plays a role which may be sufficient to eliminate the domain state and generate a uniform saturated state. [28, 29]. Detailed expressions for these energy contributions can be written down in terms of volume integrals over local energies that in turn involve local fields, local magnetic moments $\vec{m}(\vec{r})$ and spatial gradients of $\vec{m}$. Parameters involved in determining the size of each contribution are as follows :

(i) for E_{ex} it is the exchange stiffness which tries to align neighboring spins and is related to J: $A \propto kJS^2/a_0$, where J is the nearest neighbor exchange constant, S is the spin magnitude, a_0 is the lattice constant, and k is a numerical factor depending on the lattice symmetry [30];

(ii) for E_Z it is the saturation magnetization M_s of the object;

(iii) for E_{ani} it is a general parameter $\varepsilon_{ani}(\vec{m}(\vec{r}))$. Magnetocrystalline anisotropy results from the orbital coupling of the crystal structure and the spin moments via spin-orbit coupling. It depends on the crystal symmetry and any defects in the crystal lattice would cause a change in anisotropy. A way to handle this is to express ε_{ani} in terms of the angles α_i between the magnetization and the crystal axes. For uniaxial anisotropy, that leads to an expression of the form $\varepsilon_{ani}(\vec{m}(\vec{r})) = K_0 + K_1 \cos^2(2\alpha) + \ldots$;

(iv) for E_{ms} there is no parameter that sets the scale. It represents the energy cost of magnetic poles on the surface due to stray magnetic fields leaving the material and therefore depends on the shape of the sample (shape anisotropy). The fields created by the sample also lead to an internal field H_i that is different from the applied field, but also not simply given by the magnetization. It can be written as $\vec{H}_i = \vec{H}_a + \vec{H}_d$, where $\vec{H}_d$ is the so-called demagnetization field, that will depend on the sample shape. This shape dependence is the reason that the magnetization becomes non-uniform, meaning that magnetic domains form, for non-ellipsoidal objects.

This leads to an expression for the Landau free energy that reads:

$$G(\vec{M}) = \int_V \left(A(\nabla \vec{m})^2 - \mu_0 M_s(\vec{H}(\vec{r}) \cdot \vec{m}(\vec{r})) + \varepsilon_{ani}(\vec{m}(\vec{r})) - \frac{\mu_0}{2}(\vec{H}_d \cdot \vec{M}) \right) dV \quad (2.11)$$

The local minima of the G_L can be determined by varying the system's magnetization configuration and satisfying the necessary conditions for the existence of a
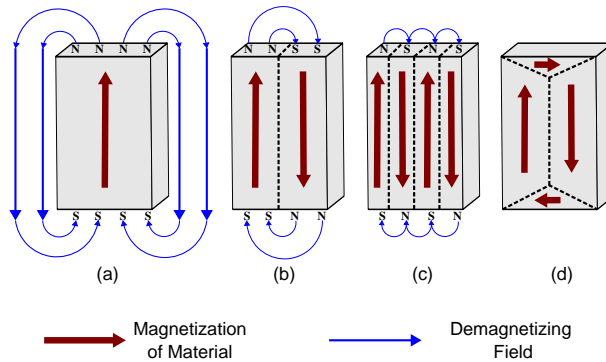
Figure 2.7: Schematic illustration of the breaking up and formation of magnetic domains (a) single domain state with uniform magnetization, (b) two-domain state with reduced magnetostatic energy, (c) four-domain state with even lower magnetostatic energy, and (d) a flux-closure domain state with zero magnetostatic energy (adapted from ref. [31]).

minimum. Stable magnetization configurations should then follow from finding free energy minima through solving the variational problem $\frac{\delta G}{\delta M} = 0$ with appropriate boundary conditions.

This works for a uniform magnetization, but does not simply allow to find configurations where different domains of the object have different directions of the magnetization. Domain theory tries to make this complexity easier to deal with. It proposes that in a macroscopic sample is subdivided in such domains that are separated by planar regions where the magnetization is changing its direction. These regions are called Domain Walls (DWs). Figure 2.7 illustrates the principle, showing how domain formation minimizes the stray fields and their energy. One point to keep in mind is that the gain is in the stray fields, but the loss is in exchange energy. If the separation between domains would be a single-atom-width plane, the exchange energy price is very high, because spins have to be fully flipped. In practice, the DW therefore will have a finite width. In the next section we look into DWs in more detail.

2.3.2. Domain Walls

Generally, there is a narrow transition region between magnetic domains where the direction of the magnetization vector varies continuously. As mentioned above, it is energetically (much) more favorable to rotate the magnetic moments gradually over the DW region. In this thesis, we will work with DWs in which the magnetization vector can rotate in one of the two ways – either in the plane of the wall, or out of that plane. These two possibilities are referred to as either a Bloch wall [23] or a

Néel wall [32], respectively. The former is more prevalent in bulk materials such as thick films, whose magnetization vector rotates parallel to the wall plane, whereas the latter is preferred for thin films, whose magnetization vector rotates in the wall plane. They will be discussed in details below.

Bloch Wall : Felix Bloch proposed the Bloch wall. Subsequently, Landau and Lifshitz analyzed its properties in greater detail. It is found in bulk materials since, despite the rotation of the magnetization vector, the condition $\nabla \cdot \vec{M} = 0$ is satisfied everywhere including the wall. This means that there is no charge associated with the wall, hence no stray field, and no magnetostatic energy cost associated with the creation of the wall. However, the exchange energy term incurs an additional cost since the neighboring magnetic moments are no longer parallel. To achieve a low magnetocrystalline energy, the magnetization within the domains prefers to align along the easy axis direction, so there will be some anisotropy cost to the wall as well as the magnetisation must rotate through a hard direction. The width of the DW δ_w is given by

$$\delta_w = \pi \sqrt{\frac{A}{K}} \tag{2.12}$$

where, A is the exchange stiffness constant and K is the anisotropy constant. The DW energy per unit area, which is the energy cost of creation of a DW per unit area in terms of the exchange and anisotropy contributions only is expressed as

$$\sigma_W = 2\pi\sqrt{AK} \tag{2.13}$$

Néel Wall : Louis Néel proposed that in thin film systems, the energy costs are different than in the bulk materials. Typically, the magnetization within the domains lies in the film plane; however, for a Bloch wall to form, the magnetization must rotate out of the film plane. This will result in surface charges or stray field and extra cost in magnetostatic energy which increases as the sample thickness decreases. Therefore, in order to reduce this energy in thin films, the magnetic moments inside the wall may rotate in the surface plane, as shown in Fig. 2.7. Such a DW is called Néel wall. Néel walls are only stable in films thinner than the wall width and it can be approximated by an elliptical cylinder of cross section $t \times \delta_w$ where t is the film thickness and δ_w is the width of the DW. The wall profile for the Néel wall is given by [33]

$$\theta(x) = 2\arctan\left(\exp\left(\frac{x - x_0}{\delta_w}\right)\right) \tag{2.14}$$

where, θ is the angle of the local magnetization in the wall, x the position along the nanowire and x_0 the central position of the DW. The DW energy is now given by

$$\sigma_w = 4\sqrt{AK} \tag{2.15}$$
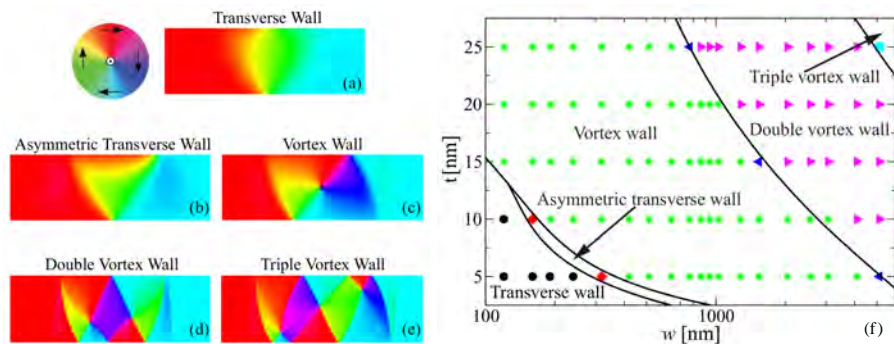
Figure 2.8: Equilibrium micromagnetic domain wall structures encountered in a Permalloy (Py) nanowire of a wide range of thicknesses and widths. TW for w = 120 nm and t = 5 nm, b) ATW for w = 160 nm and t = 10 nm, c) VW for w = 640 nm and t = 15 nm, d) DVW for w = 2560 nm and t = 20 nm, and e) TVW for w = 5120 nm and t = 25 nm. The color wheel (top left) shows the mapping between magnetization directions and colors. w,t correspond to the width and thickness of the wire respectively. Simulations were performed using Mumax3. (f) Phase diagram corresponding to the type of domain wall as a function of the width and thickness in a Py nanowire. (Image from Ref. [35]).

and the wall width by

$$\delta_w = \sqrt{\frac{A}{K}} \tag{2.16}$$

For a bulk sample the demagnetizing factor for the Bloch wall is zero, while that for the Néel wall is 1 [34].

Other types of walls which are some form of combination of Bloch and/or Néel also exist that could result in having lower energy than Bloch or Néel walls depending on thickness, external field value etc. Some of the more common examples, but not relevant to this thesis, are cross-tie walls, asymmetric walls etc.

2.4. Magnetization Dynamics

In the preceding sec.2.3 we discussed the energy contributions that influence the equilibrium state of the magnetic moments in a sample. However, it only provides a static solution for the magnetization distribution and the dynamical behavior of a system, such as its response to a change in the external field or the injection of a current, has not yet been included. Landau-Lifshitz-Gilbert equation which describes magnetization dynamics provides the solution to this problem. Additionally, some extensions are proposed to describe interactions with spin-polarized electric currents.

2.4.1. The Landau-Lifshitz-Gilbert Equation

The Landau-Lifshitz-Gilbert (LLG) equation initially proposed by Landau and Lifshitz [22] and later modified by Gilbert [36], mathematically describes the temporal and spatial evolution of the magnetization under the influence of an effective magnetic field. The same equation can be used to understand both the magnetization reversal of a uniform magnetic domain and the magnetization dynamics inside the DW.

When an external magnetic field is applied to a magnetic material, the magnetization $\vec{M}$ starts to precess in a circular orbit around the field axis. The torque that causes this precession can be written as

$$\frac{\partial \vec{M}}{\partial t} = -\gamma \vec{M} \times \vec{H_{eff}} \tag{2.17}$$

Here, γ is the gyromagnetic ratio and is expressed as $\gamma = \frac{ge\mu_0}{2m_e}$ where, g is the Landé factor (~ 2) and $\vec{H_{eff}}$ is the effective field that induces a torque due to which the magnetization will start precessing at Larmor frequency given by $\omega_L = \gamma \left| \vec{H}_{eff} \right|$.

Taking into account only this torque, the magnetization should perpetually precess around the external field. Experimentally, this is not observed: when an external field is applied, the magnetization relaxes into an equilibrium state aligned along $\vec{H}_{eff}$. Consequently, an additional damping torque $\vec{T}_d$ is required to explain the magnetization dynamics. In the LLG formalization, damping is expressed as

$$\vec{T}_d = \frac{\alpha}{M_s} \vec{M} \times \frac{\partial \vec{M}}{\partial t} \tag{2.18}$$

where, α is the damping constant, $\alpha > 0$. The damping mechanism is associated with a transfer of energy from the magnetic system to other degrees of freedom such as the lattice through the spin-orbit coupling. Therefore, the LLG equation for the net magnetization dynamics can be written as the sum of two terms: a precessional term and damping term.

$$\frac{\partial \vec{M}}{\partial t} = -\gamma \vec{M} \times \vec{H}_{eff} + \frac{\alpha}{M_s} \vec{M} \times \frac{\partial \vec{M}}{\partial t} \tag{2.19}$$

2.4.2. Spin-transfer torque

The Landau-Lifshitz-Gilbert equation presented in eq. 2.19 describes magnetization dynamics, but no interactions with spin-polarized currents or spin currents. The microscopic origins of spin transfer torque are still a matter of debate. Present consensus holds that at least two mechanisms can cause DW motion by current, to be discussed next:

Adiabatic spin-transfer Conservation of spin angular momentum provides an intuitive explanation for the effect of current on domain wall motion. When the conduction electrons flow through a spin-polarized material, their spin align with the local magnetization of their environment due to the intratomic (Hund) exchange field interaction [37]. When such an electron crosses a domain wall, it senses a change in magnetization and realigns with the local magnetization inside the domain wall. This means that the system's total angular momentum has changed from its initial value. To compensate for this change, the first domain must expand, which corresponds to a movement of the domain wall in the direction of the electron flow. The mechanism behind this type of transfer is the s–d exchange force between the localized 3d-electrons in the domain wall and the delocalized 4s-electrons carrying the current ($\vec{S} \propto \vec{M}$) [38, 39].

$$H_{ex} = -J_{ex}\vec{s} \cdot \vec{S} \tag{2.20}$$

where, J_{ex} is the exchange coupling strength. This interaction generates a torque $\vec{\tau}$ that is responsible for the movement of the domain wall along the electron flow direction.

Li and Zhang [40] and Thiaville and Miltat [41] independently proposed similar extensions to the Landau–Lifshitz–Gilbert equation to describe the interaction with an electrical current, the extension differ only in their coefficients. Both groups proposed a spin–transfer torque term as a function of the generalized velocity $\vec{u}$ which can be expressed in terms of the current density J:

$$\vec{u} = \frac{g\mu_B P}{2eM_s}\vec{J} \tag{2.21}$$

where g is the Landé factor, μ_B the Bohr magneton, P the spin polarization, e the electron charge and M_s the saturation magnetization. According to the Li-Zhang model, the spin-transfer torque $\vec{\tau}_{adiabatic}$ is expressed as[40]:

$$\vec{\tau}_{adiabatic} = -\frac{\vec{M}}{M_s^2} \times (\vec{M} \times (\vec{u} \cdot \vec{\nabla}))\vec{M} \tag{2.22}$$

According to the Thiaville-Miltat model, the spin-transfer torque is expressed as[41]:

$$\vec{\tau}_{adiabatic} = -(\vec{u} \cdot \vec{\nabla})\vec{M} \tag{2.23}$$

At low temperatures the magnetization vector $\vec{M}$ has a constant length, so then Eq.2.22 proposed by Li and Zhang is equivalent to the formulation of Thiaville and Miltat in Eq.2.23. Both models work only above the Walker breakdown field (the maximum external field at which the DW attains a maximum velocity) and coul not explain the experimentally observed continuous domain wall propagation for relatively low currents densities.

Non-adiabatic spin-transfer Considering only the adiabatic contribution, the predicted critical current density for domain wall motion is much larger than the experimentally observed value [41, 42]. An additional torque mechanism is required to correctly describe the experiments which results from the spatial mistracking of the conduction electron spins and the local moments. When the spin orientation of the conduction electrons does not match the spin direction of the local moments, the electrons can be reflected from the local moments, thereby altering their direction of motion. In turn, this can transfer linear momentum from the conduction electrons to the local moments, leading to DW motion. This mechanism is commonly referred to as the non-adiabatic spin transfer process, where non-adiabaticity represents the misdirection of the conduction electron spins and local moments.

Thiaville and Miltat proposed the following addition to the Landau-Lifshitz-Gilbert equation to quantify the mistracking between conduction electron spin and local magnetization [43]:

$$\vec{\tau}_{non-adiabatic} = \frac{\beta}{M_s} \vec{M} \times \left[(\vec{u} \cdot \vec{\nabla}) \vec{M} \right] \tag{2.24}$$

where, β is the non-adiabaticity parameter and is identified as the squared ratio of the exchange length and spin flip length, $\beta = (\lambda_{ex}/\lambda_{sf})^2$ where λ is the associated diffusion length.

Zhang and Li provide a similar equation, but a more rigorous derivation from the semiclassical Bloch equation[38]. Zhang's version uses a slightly reduced $\vec{u}$ and defines β equal to the ratio of the exchange time and spin flip relaxation time ($\beta = \tau_{ex}/\tau_{sf}$), but otherwise the proposed extensions are identical.

The complete LLG equation for the current induced domain wall motion including both the adiabatic and non-adiabatic torques can be written as

$$\frac{\partial \vec{M}}{\partial t} = -\gamma \vec{M} \times \vec{H}_{eff} + \alpha \frac{\vec{M}}{M_s} \times \frac{\partial \vec{M}}{\partial t} - (\vec{u} \cdot \vec{\nabla}) \vec{M} + \frac{\beta}{M_s} \vec{M} \times \left[(\vec{u} \cdot \vec{\nabla}) \vec{M} \right] \tag{2.25}$$

These equations provide experimentalists various quantities to verify the theoretical descriptions. From the application point of view, the usefulness of the current induced DW motion depends on two parameters: the current required for the depinning of the DW and the DW velocity. For applications such as the racetrack memory [44], one is obviously interested in low critical current densities and high and reproducible domain wall velocities. Typical measured current densities on Py based structures are relatively high and of the order of 10^{12} A/m^2 [45–47]. By improving the sample quality (increasing nonadiabaticity), the depinning critical current could be decreased [48]. Another way could be by increasing spin polarization. When there are no pinning sites, the critical current is proportional to the hard-axis magnetic anisotropy [49], and depends on the spin polarization of the

current:

$$I_c = \left(\frac{2e}{\hbar}\right)\left(\frac{\alpha}{P}\right) V M_s (H_K + 2\pi M_s) \qquad (2.26)$$

where α is Gibert damping parameter, P is the spin polarization of the current, V is the volume of the domain, M_s is the saturation magnetization and H_K is the anisotropy field [29, 50, 51]. Regarding the DW velocity, initial studies reported velocities of the order of 1 m/s [45, 46], but in high quality samples of Py, with the maximum applicable current density, STT-driven DW velocities were observed up to 100 m/s [52]. However, experimentally increasing the current density may lead to Joule heating in the sample and cause damage. Half metals like CrO_2 with 100% spin polarization are a natural choice to consider in the development of reliable domain wall motion and pinning technology.

References

[1] Yang, C. N. Concept of Off-Diagonal Long-Range Order and the Quantum Phases of Liquid He and of Superconductors. Rev. Mod. Phys. **34**, 694–704 (1962). URL https://link.aps.org/doi/10.1103/RevModPhys.34.694.

[2] Lahabi, K. Spin-triplet supercurrents of odd and even parity in nanostructured devices. Ph.D. thesis, Leiden University (2018).

[3] Kontos, T. et al. Josephson junction through a thin ferromagnetic layer: Negative coupling. Phys. Rev. Lett. **89**, 137007 (2002). URL https://link.aps.org/doi/10.1103/PhysRevLett.89.137007.

[4] Blum, Y., Tsukernik, A., Karpovski, M. & Palevski, A. Oscillations of the Superconducting Critical Current in Nb-Cu-Ni-Cu-Nb Junctions. Phys. Rev. Lett. **89**, 187004 (2002). URL https://link.aps.org/doi/10.1103/PhysRevLett.89.187004.

[5] Ryazanov, V. V. et al. Coupling of two superconductors through a ferromagnet: Evidence for a π junction. Phys. Rev. Lett. **86**, 2427–2430 (2001). URL https://link.aps.org/doi/10.1103/PhysRevLett.86.2427.

[6] Houzet, M. & Buzdin, A. I. Long range triplet josephson effect through a ferromagnetic trilayer. Physical Review B **76**, 060504 (2007).

[7] Halterman, K., Valls, O. T. & Barsic, P. H. Induced triplet pairing in clean s-wave superconductor/ferromagnet layered structures. Phys. Rev. B **77**, 174511 (2008). URL https://link.aps.org/doi/10.1103/PhysRevB.77.174511.

[8] Kogan, V. G., Dobrovitski, V. V., Clem, J. R., Matawari, Y. & Mints, R. G. Josephson junction in a thin film. Phys. Rev. B **63**, 144501 (2001). URL https://link.aps.org/doi/10.1103/PhysRevB.63.144501.

[9] Moshe, M., Kogan, V. G. & Mints, R. G. Edge-type josephson junctions in narrow thin-film strips. Phys. Rev. B **78**, 020510R (2008). URL https://link.aps.org/doi/10.1103/PhysRevB.78.020510.

[10] Clem, J. R. Josephson junctions in thin and narrow rectangular superconducting strips. Phys. Rev. B **81**, 144515 (2010). URL https://link.aps.org/doi/10.1103/PhysRevB.81.144515.

[11] Boris, A. A. et al. Evidence for nonlocal electrodynamics in planar josephson junctions. Phys. Rev. Lett. **111**, 117002 (2013). URL https://link.aps.org/doi/10.1103/PhysRevLett.111.117002.

[12] Fermin, R., de Wit, B. & Aarts, J. Beyond the effective length: How to analyze magnetic interference patterns of thin-film planar josephson junctions with finite lateral dimensions. Phys. Rev. B **107**, 064502 (2023). URL https://link.aps.org/doi/10.1103/PhysRevB.107.064502.

[13] Keizer, R. S. et al. A spin triplet supercurrent through the half-metallic ferromagnet CrO_2. Nature **439**, 825–827 (2006). URL https://doi.org/10.1038/nature04499.

[14] Anwar, M. S., Czeschka, F., Hesselberth, M., Porcu, M. & Aarts, J. Long-range supercurrents through half-metallic ferromagnetic CrO_2. Phys. Rev. B **82**, 100501 (2010). URL https://link.aps.org/doi/10.1103/PhysRevB.82.100501.

[15] Anwar, M. S., Veldhorst, M., Brinkman, A. & Aarts, J. Long range supercurrents in ferromagnetic CrO_2 using a multilayer contact structure. Applied Physics Letters **100**, 052602 (2012). URL https://doi.org/10.1063/1.3681138.

[16] Singh, A., Jansen, C., Lahabi, K. & Aarts, J. High-Quality CrO_2 Nanowires for Dissipation-less Spintronics. Physical Review X **6**, 041012 (2016).

[17] Koyama, T. et al. Observation of the intrinsic pinning of a magnetic domain wall in a ferromagnetic nanowire. Nature materials **10**, 194–197 (2011).

[18] Weiss, P. & Foex, G. Le Magnétism. Paris: Armand Colln (1926).

[19] Barkhausen, H. Zwei mit Hilfe der neuen Verstärker entdeckte Erscheinungen. Physische Zeitschrift **20**, 401–403 (1919).

[20] Sixtus, K. J. & Tonks, L. Propagation of Large Barkhausen Discontinuities. Phys. Rev. **37**, 930–958 (1931). URL https://link.aps.org/doi/10.1103/PhysRev.37.930.

[21] Bitter, F. Experiments on the Nature of Ferromagnetism. Phys. Rev. **41**, 507–515 (1932). URL https://link.aps.org/doi/10.1103/PhysRev.41.507.

[22] Landau, L. & Lifschitz, E. On the Theory of the Dispersion of Magnetic Permeability in Ferromagnetic Bodies. Physische Zeitschrift der Sowjetunion **8**, 153–169 (1935).

[23] Bloch, F. Zur Theorie des Austauschproblems und der Remanenzerscheinung der Ferromagnetika. Zeitschrift für Physik **74**, 295–335 (1932). URL https://doi.org/10.1007/BF01337791.

[24] Heisenberg, W. Zur Theorie der Magnetostriktion und der Magnetisierungskurve. Zeitschrift für Physik **69**, 287–297 (1931). URL https://doi.org/10.1007/BF01391350.

[25] Kittel, C. Physical Theory of Ferromagnetic Domains. Rev. Mod. Phys. **21**, 541–583 (1949). URL https://link.aps.org/doi/10.1103/RevModPhys.21.541.

[26] Hubert, A. & Schäfer, R. Magnetic Domains - The Analysis of Magnetic Microstructures (Springer Berlin, Heidelberg, 1998).

[27] O'Handley, R. C. Modern Magnetic Materials - Principles and Applications (John Wiley & Sons, Inc., 1999).

[28] Marrows, C. H. Spin-polarised currents and magnetic domain walls. Advances in Physics **54**, 585–713 (2005). URL https://doi.org/10.1080/00018730500442209.

[29] Zou, X. Magnetic Domain Configurations and Huge Wall Resistivity in Half-metallic Chromium Dioxide (CrO_2) Nanostructures. Ph.D. thesis, Brown University, Providence, Rhode Island, 5 (2010).

[30] Bertotti, G. Hysteresis in Magnetism (First Edition. Academic Press, San Diego, CA, USA, 1998).

[31] University of Birmingham, Magnetic Materials Group (2009). URL https://www.birmingham.ac.uk/research/activity/metallurgy-materials/magnets/Magnetic-Materials-Background-Information.aspx.

[32] Néel, L. Quelques propriétés des parois des domaines élémentaires ferromagnétiques. Cahiers de Physique **25**, 1–20 (1944).

[33] Slonczewski, J. Current-driven excitation of magnetic multilayers. Journal of Magnetism and Magnetic Materials **159**, L1–L7 (1996). URL https://www.sciencedirect.com/science/article/pii/0304885396000625.

[34] Coey, J. M. D. Magnetism and Magnetic Materials (Cambridge University Press, New York, 2010). URL http://www.cambridge.org/9780521816144.

[35] Estévez, V. & Laurson, L. Head-to-head domain wall structures in wide permalloy strips. Phys. Rev. B **91**, 054407 (2015). URL https://link.aps.org/doi/10.1103/PhysRevB.91.054407.

[36] Gilbert, T. A phenomenological theory of damping in ferromagnetic materials. IEEE Transactions on Magnetics **40**, 3443–3449 (2004).

[37] Berger, L. Low-field magnetoresistance and domain drag in ferromagnets. Journal of Applied Physics **49**, 2156–2161 (1978). URL https://doi.org/10.1063/1.324716. https://doi.org/10.1063/1.324716.

[38] Zhang, S. & Li, Z. Roles of Nonequilibrium Conduction Electrons on the Magnetization Dynamics of Ferromagnets. Phys. Rev. Lett. **93**, 127204 (2004). URL https://link.aps.org/doi/10.1103/PhysRevLett.93.127204.

[39] Simon, B. G. Domain wall motion in Permalloy nanowires. Master's thesis, Leiden University, Netherlands (2018).

[40] Li, Z. & Zhang, S. Domain-Wall Dynamics and Spin-Wave Excitations with Spin-Transfer Torques. Phys. Rev. Lett. **92**, 207203 (2004). URL https://link.aps.org/doi/10.1103/PhysRevLett.92.207203.

[41] Thiaville, A., Nakatani, Y., Miltat, J. & Vernier, N. Domain wall motion by spin-polarized current: a micromagnetic study. Journal of Applied Physics **95**, 7049–7051 (2004). URL https://doi.org/10.1063/1.1667804. https://doi.org/10.1063/1.1667804.

[42] Kläui, M. et al. Domain wall motion induced by spin polarized currents in ferromagnetic ring structures. Applied Physics Letters **83**, 105–107 (2003). URL https://doi.org/10.1063/1.1588736. https://doi.org/10.1063/1.1588736.

[43] Thiaville, A., Nakatani, Y., Miltat, J. & Suzuki, Y. Micromagnetic understanding of current-driven domain wall motion in patterned nanowires. Europhysics Letters **69**, 990 (2005). URL https://dx.doi.org/10.1209/epl/i2004-10452-6.

[44] Parkin, S. S. P., Hayashi, M. & Thomas, L. Magnetic Domain-Wall Racetrack Memory. Science **320**, 190–194 (2008). URL https://www.science.org/doi/abs/10.1126/science.1145799.

[45] Yamaguchi, A. et al. Real-space observation of current-driven domain wall motion in submicron magnetic wires. Phys. Rev. Lett. **92**, 077205 (2004). URL https://link.aps.org/doi/10.1103/PhysRevLett.92.077205.

[46] Kläui, M. et al. Controlled and reproducible domain wall displacement by current pulses injected into ferromagnetic ring structures. Phys. Rev. Lett. **94**, 106601 (2005). URL https://link.aps.org/doi/10.1103/PhysRevLett.94.106601.

[47] Hayashi, M. et al. Dependence of Current and Field Driven Depinning of Domain Walls on their Structure and Chirality in Permalloy Nanowires.

Phys. Rev. Lett. **97**, 207205 (2006). URL `https://link.aps.org/doi/10.1103/PhysRevLett.97.207205`.

[48] Meier, G. et al. Direct imaging of stochastic domain-wall motion driven by nanosecond current pulses. Phys. Rev. Lett. **98**, 187202 (2007). URL `https://link.aps.org/doi/10.1103/PhysRevLett.98.187202`.

[49] Tatara, G. & Kohno, H. Theory of Current-Driven Domain Wall Motion: Spin Transfer versus Momentum Transfer. Phys. Rev. Lett. **92**, 086601 (2004). URL `https://link.aps.org/doi/10.1103/PhysRevLett.92.086601`.

[50] Koch, R. H., Katine, J. A. & Sun, J. Z. Time-resolved reversal of spin-transfer switching in a nanomagnet. Phys. Rev. Lett. **92**, 088302 (2004). URL `https://link.aps.org/doi/10.1103/PhysRevLett.92.088302`.

[51] Sun, J. Z. Spin-current interaction with a monodomain magnetic body: A model study. Phys. Rev. B **62**, 570–578 (2000). URL `https://link.aps.org/doi/10.1103/PhysRevB.62.570`.

[52] Hayashi, M. et al. Current Driven Domain Wall Velocities exceeding the Spin Angular Momentum Transfer Rate in Permalloy Nanowires. Phys. Rev. Lett. **98**, 037204 (2007). URL `https://link.aps.org/doi/10.1103/PhysRevLett.98.037204`.

3

Growth and Properties of CrO_2 Nanowires

Chromium dioxide (CrO_2) nanowires with their half-metallic ferromagnetic properties have shown great promise in spintronics applications. However, growth of such wires remains challenging. We used the Selective Area growth method to fabricate high quality epitaxial CrO_2 wires on a TiO_2 substrate, using trenches oriented both along the substrate [001] c-axis and along the [010] b-axis, which are the magnetically easy and hard axis of the wire, respectively. We investigated the morphology of the wires by high-resolution transmission electron microscopy (TEM) and measured their physical properties, in particular magnetoresistance (MR) and the Anomalous Hall Effect (AHE). TEM images showed that the morphology of the wires grown along the two axes are very different. MR data show very sharp switching for c-axis grown wires (the easy axis), even for quite large wire widths. The AHE is found to be different for c-axis wires and b-axis wires, which we argue to be due to a different wire morphology on the nanoscale.

3.1. Introduction

Binary oxides with the rutile structure are currently of interest again, especially the ones which show good metallic conductivity. In the area of spintronics, in particular CrO$_2$, RuO$_2$ and IrO$_2$, plus substituted alloys have been studied in recent years. CrO$_2$ is a half-metallic ferromagnet (HMF) [1], and therefore fully spin-polarized; RuO$_2$ was recently found to be a weak collinear antiferromagnet [2] and is a prime candidate for showing the Crystal Hall effect [3]; and IrO$_2$ has been studied for its use as spin current detector [4]. The HMF nature of CrO$_2$ makes it particularly interesting for spintronics applications, with recent studies reporting on the expected performance in magnetic tunnel junctions[5], on the resistance of single domain walls[6], on Gilbert damping in epitaxial films[7], and on spin-curvature induced resistivity[8]. A significant drawback is that the compound is metastable at ambient conditions [9]. Single crystals can be synthesized using high pressure, but thin films cannot be grown with the standard physical deposition methods such as molecular beam epitaxy, sputtering, or pulsed laser deposition. Instead, a chemical vapor deposition (CVD) method has to be used, in which a precursor gas, mixed with oxygen, is led over a heated substrate. At the right substrate temperature, dissociation takes place, and CrO$_2$ is formed [10, 11].

Because of relatively good lattice matching, the substrate of choice for the deposition is TiO$_2$, and, to a lesser degree, Al$_2$O$_3$. Magnetotransport properties of thin films grown by the CVD method grown on either substrate have been extensively investigated [12–15]. One salient finding for films grown on TiO$_2$ is that the easy and hard axes for the magnetization lie along different directions in the crystal (easy axis is the [001] *c*-axis) than in thin and inevitably slightly strained films (easy axis often is the [010] *b*-axis). It was even observed that, through strain release, this can lead to a change of the easy (hard) axis direction, both as function of temperature and film thickness [13, 16]. Observations of biaxial anisotropy can also be explained through this relaxation mechanism [16–18].

Much of this work has been done on films, but for incorporating CrO$_2$ in mesoscopic structures, the grainy nature of the films is a serious impediment. Substrate treatment plays a role in the grain morphology [16, 19], and influence of grain boundaries was observed in the form of Intergrain Tunneling Magnetoresistance (ITMR) [14, 15]. Grain boundaries can be avoided, however, by using the technique of Selective Area (SA) growth, which allow to grow high-quality nanowires and other structures. The technique is based on the fact that, at the required deposition conditions, CrO$_2$ grows epitaxially on TiO$_2$, but does not form any deposit on silicon oxide (SiO$_x$) [20]. By etching a trench in a SiO$_x$ layer deposited on the TiO$_2$ substrate, high quality nanowires can be grown. The magnetotransport properties of such wires

were studied [21–24] and more recently, they were used to investigate spin-triplet superconductivity [25] and the resistance of a single domain wall (DW)[26], which is of particular interest in half metals.

Given the fact that CrO$_2$ nanowires are of clear interest for a variety of spintronics phenomena as referred to above, little attention has been paid to the growth and the morphology. It was reported that lateral overgrowth occurs when the growing layer reaches the top of the SiO$_x$ mask, and is accompanied by the formation of side facets [20, 25]. but also that the initial growth can be quite defective, with a high dislocation density [20], or even voids [25].

In this thesis, we make a detailed study of the morphology of SA-grown nanowires, and combine this with magnetotransport experiments. We focus on growing wires on TiO$_2$(100), with directions along the substrate c-axis and b-axis (the magnetic easy and hard axis, respectively) for trench and wire widths in the range of 0.5 μm to 2 μm. We use atomic force microscopy (AFM), but more importantly Transmission Electron Microscopy (TEM) to study the morphology. The main and new finding of the study is that the wires along the two axes differ in important details, both with respect to the morphology and with respect to the magnetotransport. Most surprising, possibly, is that the Anomalous Hall Effect (AHE) is different for the two types of wires. This is very different from what is found when bars are etched in films by Ar-ion etching along the magnetic easy and hard directions [14, 15], which can be understood from the difference in fabrication.

The chapter is structured as follows. First we give a detailed description of the nanofabrication process which leads to SA-grown nanowires. Then we concentrate on wire widths around 0.5 μm and give TEM and electrical and magneto-transport results for the c-axis (magnetic easy axis) wires, followed by the results for the b-axis (magnetic hard axis) wires. Because of in particular the AHE results, we finally present data on larger hard-axis wire widths, up to 2 μm.

3.2. Selective area growth of CrO$_2$ nanowires

CrO$_2$ and TiO$_2$ both crystallize in the rutile structure, with a tetragonal unit cell. Both structures are shown in the Appendix, sec.3.8.2. We use (100) oriented TiO$_2$ substrates, which means that the b- and c-axes of the structure lie in the film plane. For CrO$_2$, the lattice parameters are $a = b = 0.4421$ nm and $c = 0.2916$ nm. For TiO$_2$ the values are $a = b = 0.4594$ nm, $c = 0.2958$ nm. The CrO$_2$ values in the plane are therefore smaller by -3.8% (b-axis) and -1.5% (c-axis), resulting in tensile strain. In CrO$_2$ films on HF-treated substrates, comparatively lower strain along c-axis leads to crystallites oriented along the c-direction [16]. As was already mentioned, the
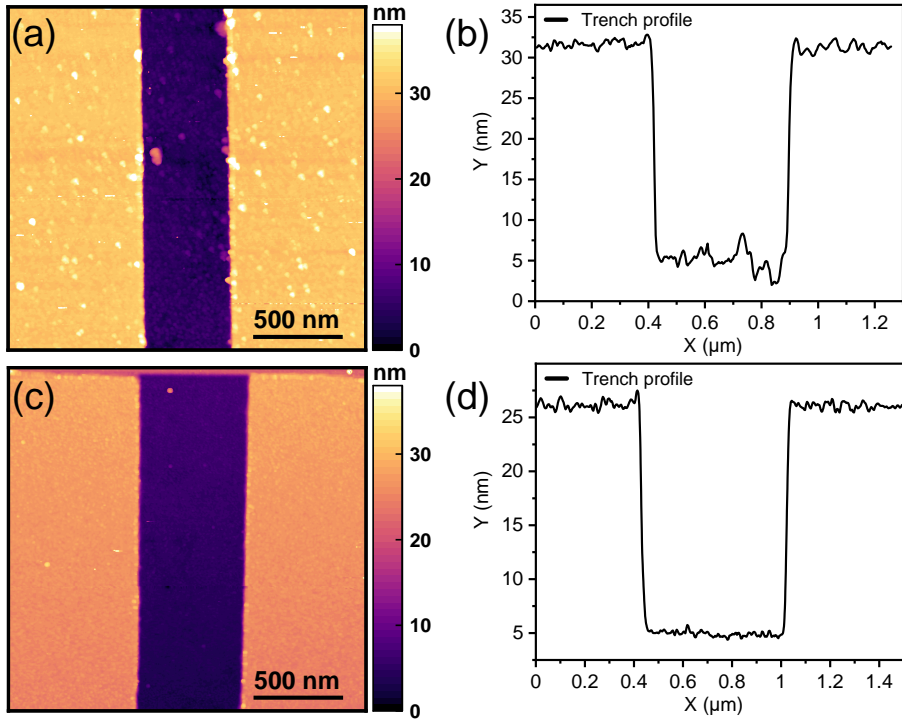
Figure 3.1: AFM images of etched SiO$_x$ masks on top of TiO$_2$ substrates. The thickness of the SiO$_x$ layer in this case is 19 nm. (a) Surface scan of a section of a mask with the trench, taken from an overetched trench (depth 26 nm). (b) The corresponding line profile of the trench showing a rough and damaged TiO$_2$ surface at the bottom. (c) Surface scan of an optimally etched trench (depth 21 nm). (d) The corresponding line profile showing a smooth surface at the bottom.

crystallographic c-axis is the magnetic easy axis, while the b-axis is the hard axis. Hereafter, we call c-axis oriented wires as 'easy' wires and b-axis oriented wires as 'hard' wires.

Making the SiO$_x$ mask starts with a HF etch of the TiO$_2$ substrate, depositing a SiO$_x$ layer with a typical thickness of about 20-25 nm, and electron beam patterning to create a positive resist mask with the desired device structure. The trench is selectively etched into the SiO$_x$ by reactive ion etching. After that, CrO$_2$ nanowires are grown in the trenches using CVD in a two-zone furnace, where the substrate temperature is kept at 390°C, while the precursor CrO$_3$ is heated to 260°C in the presence of a flow of O$_2$ carrier gas. The temperature window for growth is very narrow, not more than 10°C. We found that, for successful growth, it is critical to neither underetch nor overetch the trench. The result of underetching is clear, the trench bottom will then still be formed by SiO$_x$, and CrO$_2$ cannot grow. Overetching
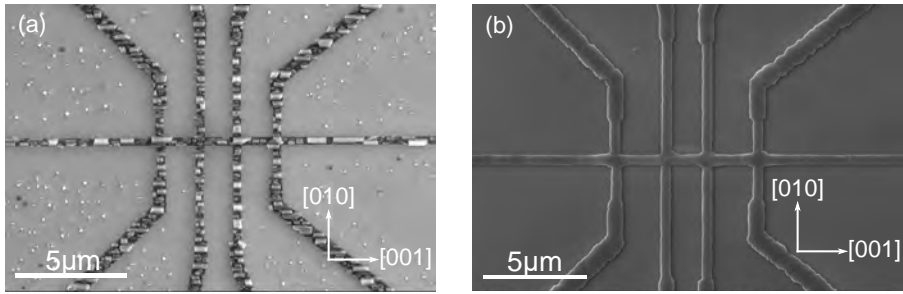
Figure 3.2: SEM images comparing (a) growth in an overetched and rough trench bottom and (b) the growth in a smooth trench. The horizontal direction [001] in the images is the crystal c-axis, which is also the orientation of the long axis of the crystallites in (a).

is also detrimental, however, as it damages the underlying TiO$_2$ surface. Fig. 3.1 compares the AFM images of two trenches, an overetched one with a depth of about 26 nm, and an optimally etched one of 21 nm. Fig. 3.1(a) has a rough bottom while Fig. 3.1(c) is very smooth, and that translates into the growth. Fig. 3.2(a) shows SEM images of wire growth on a rough trench surface. This causes formation of unevenly distributed CrO$_2$ crystallites that fail to merge timely, resulting in a broken wire growth. However, for an optimally etched smooth trench as seen in Fig. 3.2(b), the crystallites merge completely at the bottom surface of the trench and we get high quality epitaxial growth. The depth window where we get desired trench quality to facilitate good nanowire growth is rather small, not more than a few nm. That means not only the etching, but also the SiO$_x$ deposition has to be monitored carefully, while also the uniformity of the deposition is important. In our optimized procedure we deposit on both a 'device' substrate and a 'test' substrate in the same run. On the test substrate we measure the actual SiO$_x$ thickness by small-angle X-ray diffraction, an etch run is performed, and AFM is used to measure the resulting trench depth. From AFM images the etch rate is computed and used in growing the wire on the 'device' substrate. Afterwards, devices are inspected by SEM. We grew CrO$_2$ nanowires along different angles with respect to the TiO$_2$ substrate axes. Here, we will focus on the easy [001] and hard [010] wires while intermediate angles are discussed in the Appendix, sec. 3.8.4[27].

As a side note, CrO$_2$ nanowires have also been SA-grown in considerably deeper trenches, of about 100 nm [24, 26]. We have not investigated growth in such deeper trenches.
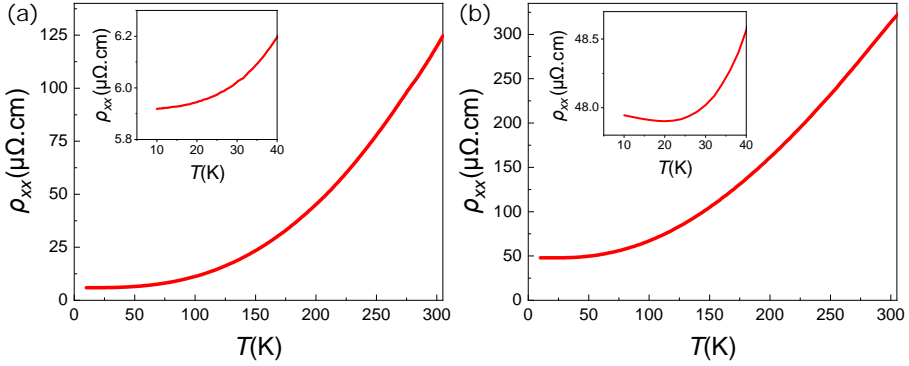
Figure 3.3: Resistivity as a function of temperature for (a) an easy wire (width 580 nm, thickness 105 nm, contact distance 4 μm); the inset shows the positive temperature coefficient of resistance at lower temperature. (b) a hard wire (width 610 nm, thickness 60 nm, contact distance 2.5 μm); the inset shows an upturn in resistance below 20 K.

3.3. Resistivity as function of temperature: easy and hard wires

The temperature dependence of the resistivity, $\rho(T)$, is an important characterization parameter. The transport measurements were carried out over a temperature range from 300 K to 10 K in a Physical Property Measurement System (PPMS). Fig. 3.3(a) shows $\rho(T)$ for a typical easy wire: a width around 580 nm, a thickness of 105 nm and with a distance between the contacts around 4 μm. The room temperature resistivity ρ_{300} is 120 $\mu\Omega$cm while the low-temperature (10 K) value ρ_0 is 5.9 $\mu\Omega$cm. This gives a residual-resistance ratio (RRR, the ratio between ρ_{300} and ρ_0) of ≈ 21. The wire has a positive temperature coefficient of resistance at all temperatures, also at the lowest temperatures, as seen in the inset of Fig. 3.3(a). This suggests very little or no grain boundary scattering of electrons [24]. We also notice that in our easy wire, while ρ_0 is similar, ρ_{300} is more than 2 times lower compared to previous studies on films and SA-grown nanowires [12, 15, 24], indicating higher conductivity (or better metallic behavior) of our nanowires at room temperature. This suggests better crystal quality of the wires, which is supported by TEM analysis on an easy wire that is discussed in the next section.

As mentioned in section 3.2, we observe that for both easy and hard wires, the preferred direction of crystallite growth is the c-axis, i.e. along the easy wire length, but along the hard wire width. This makes growing hard wires more difficult. They are more sensitive to the trench depth, and also the width cannot be too small. We found the minimal width for reproducible good growth to be about 500 nm, unlike easy wires which we could grow down to a width of ≈ 100 nm.

Fig. 3.3(b) shows ρ(T) for a similar but hard wire: a width around 610 nm, a thickness of 60 nm, and distance between the contacts of 2.5 μm. For this wire, ρ_{300} is 314 μΩcm while ρ_0 is 47 μΩcm, yielding an RRR of 6.7. These numbers are similar to the epitaxial hard wires measured in Ref. [24] but significantly higher than Ar ion-etched wires from thin films [15]. Since the growth kinetics for a SA-grown hard wire is totally different from the hard wire obtained from a CrO_2 film through Ar ion-etching, it is not reasonable to compare the ρ(T) measurements. We further observe that there is a small upturn in ρ at low temperature around 20 K, as seen in inset of Fig. 3.3(b). This indicates the presence of grain boundaries in the nanowire, that become more dominant at lower temperatures [24]. The morphology of the hard wire is further explained in details in section 3.5.1.

3.4. Easy axis wires

3.4.1. TEM analysis

Using high-resolution transmission electron microscopy (HR-TEM), we analyzed the crystal structure and orientation of the nanowires and compared them to the single crystal TiO_2 substrate. A low magnification image of a cross-section of the easy nanowire is given in Fig. 3.4(a) wherein, we can see the TiO_2 substrate at the bottom with the CrO_2 nanowire on top of TiO_2. The nanowire grew inside the 517 nm wide trench that was etched in the SiO_x mask (shown in white in Fig. 3.4(a)) that was deposited on the TiO_2 substrate. The cross-section also clearly shows no CrO_2 growth on top of the SiO_x mask. Contrary to previous report by Singh et. al,[25] we observe no overgrowth for the easy wire. However, we still observe the formation of side facets. These facets are oriented at a 90° angle with respect to the edge of the SiO_x mask and a 45° angle with respect to the TiO_2 substrate, as seen near the bottom right in Fig. 3.4(a). The nanowire is 75 nm high and 525 nm wide at its highest and widest point, respectively. The trapezoidal shape of the wire is only interrupted by a triangular divot. A higher resolution image of the area underneath the divot is shown in the Appendix, Fig. 3.10(a). The area underneath the divot, right at the interface between the TiO_2 substrate and the CrO_2 nanowire, has several regions with a darker contrast. An HR-TEM image of one of these regions, highlighted by the white box in Fig. 3.4(a), is shown in Fig. 3.4(b). This atomic resolution image shows the TiO_2 substrate in the bottom left corner and two different crystal CrO_2 domains on the right. The fast Fourier transform (FFT) of the area in the blue box helps us to establish that the TiO_2 crystal substrate is oriented along the [001] zone-axis as expected for the easy nanowire. As mentioned before in section 3.2, we would expect the CrO_2 nanowire to grow epitaxially because of the minor lattice mismatch between the TiO_2 and the CrO_2. However, we observe two different CrO_2
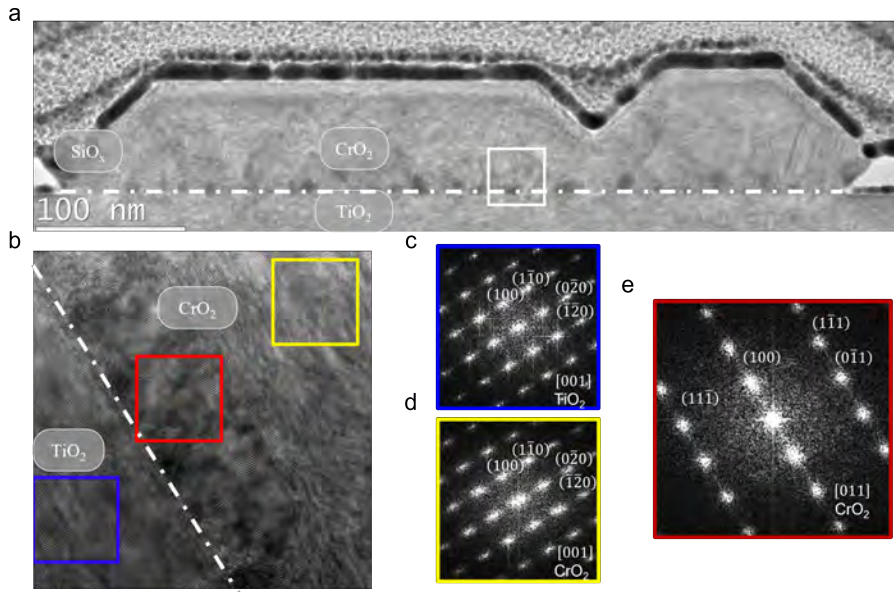
Figure 3.4: TEM inspection of a cross-section from the CrO$_2$ nanowire along the easy axis. (a) Low resolution TEM image of the TiO$_2$ substrate at the bottom and the partially grown CrO$_2$ nanowire in between the SiO$_x$ mask. (b) High-resolution TEM image of the dark cluster highlighted in (a) showing the TiO$_2$ substrate at the bottom (blue box) and two CrO$_2$ crystal domains with different crystal orientations (red and yellow boxes). (c-e) The indexed fast Fourier transforms of the areas highlighted in (b) (blue box in (c), yellow box in (d), red box in (e)). The FFT's show that most of the nanowire grows epitaxially with the substrate, but some crystal domains have a different orientation than the substrate.

crystal orientations in Fig. 3.4(c). Indeed, the FFT of the area inside the yellow box, just like the bulk of the nanowire, corresponds to the diffraction pattern of CrO$_2$ orientated along the [001] zone axis. However, the FFT of the area in the red box corresponds to the diffraction pattern of CrO$_2$ oriented along the [011] zone axis. This shows that the bulk of the CrO$_2$ grows epitaxially on the TiO$_2$ substrate, but some small regions have a different crystal orientation than the TiO$_2$ substrate. An atomic model of the different crystal domains is displayed in Fig. 3.10(b) of the Appendix. These irregularities in the crystal orientation can mostly be found at the interface between the TiO$_2$ substrate and the CrO$_2$ nanowire or at the interface with the SiO$_x$ mask. This is probably due to imperfections in the TiO$_2$ substrate caused by the over-etching of the SiO$_x$ mask or conversely by leaving a SiO$_x$ residue by under-etching the SiO$_x$ mask.
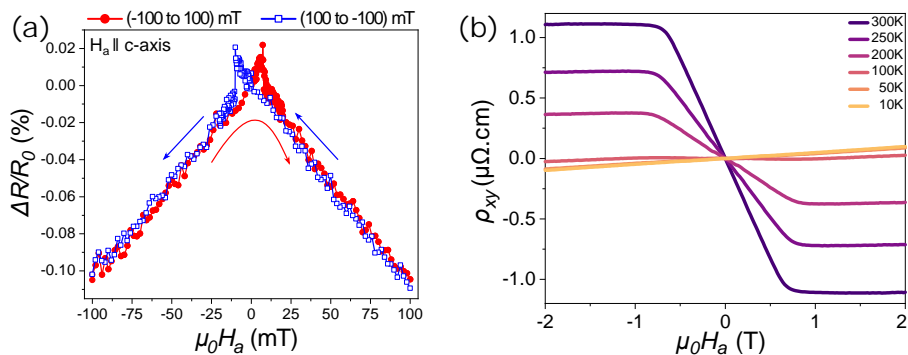
Figure 3.5: Magnetotransport measurements on the same 580 nm wide easy wire as shown in Fig. 3.3. (a) In-plane longitudinal MR measured at 10K. The external magnetic field H_a is parallel to the easy wire i.e. (H_a || c-axis [001]). The field is swept from -100 mT to 100 mT (filled red circles) and then from 100 mT to -100 mT (open blue squares). The arrows in blue and red show the sweep direction for the respective curves. (b) Hall resistivity as a function of external out-of-plane field for the same easy wire measured at various temperatures between 10 K to 300 K. A current of 100 μA is applied in both cases.

3.4.2. Magnetotransport

We further characterized CrO_2 wires through magnetotransport measurements for different magnetic field orientations and at different temperatures. Fig. 3.5(a) shows the longitudinal magnetoresistance (MR) behavior $(R(H_a) - R(0))/R(0) = \Delta(R)/R(0)$ at 10 K, where H_a is the magnetic field along the wire axis, for the same 580 nm wide easy wire as measured in section 3.3. We find that the MR behavior differs from that of previous SA-grown wires of comparable or smaller width. In contrast to earlier studies that showed parabolic behavior and an extended switching range for a similar wire width, we find that the magnetization switching is sharp, with only very little supralinear behavior when approaching the coercive field H_c at around 10 mT [24]. In earlier research, even 100 nm-wide wires did not exhibit the same degree of sharp switching as this 580 nm-wide wire demonstrates. We view this as further evidence of the high crystalline quality of the wires, possibly as a consequence of using quite shallow trenches with very well controlled bottom surfaces.

Fig. 3.5(b) shows measurements of the Hall resistivity as a function of external out-of-plane (OP) field for different temperatures in a range from 300 K to 10 K. The data are represented as ρ_{xy} as function of magnetic field, with $\rho_{xy} = V_{xy}d/I$, where V_{xy} is the transverse voltage, I is the measurement current, and d is the thickness of the wire. The behavior can, as expected, be described by

$$\rho_{xy}(H_a) = \mu_0 (R_0 H_a + R_{AHE} M) \tag{3.1}$$

with R_0 the normal Hall coefficient, R_{AHE} the anomalous Hall coefficient, and M the magnetization of the ferromagnet. We see that R_{AHE} decreases from 300 K in a roughly linear fashion down to 100 K, where zero is reached. Below 100 K, R_{AHE} is zero. This behavior is well known, and attributed to a Berry phase, caused by an increasing amount of spin defects with increasing temperature that produce a non-trivial spin background through which the carriers move [28, 29].

The values of R_{AHE} can be compared to earlier work. According to Eq. 3.1, $R_{AHE} = \rho_{xy}(0)/(\mu_0 M)$, but the use of different units and the ambiguity with respect to the value of M (the saturation value at 300 K is lower than at 10 K, and lower than inferred from the saturation moment of $2\,\mu_B$/Cr-atom) make it more straightforward to compare values for $\rho_{xy}(0)$ at 300 K. From Fig. 3.5(b) we find $\rho_{xy}(0) = 1.1\,\mu\Omega$cm for the 580 nm wide easy wire. For films measured by the van der Pauw method, values of $1.4\,\mu\Omega$cm[11] and $0.8\,\mu\Omega$cm [30] are reported. For etched films with a bar along the easy axis, two studies report $1.5\,\mu\Omega$cm[29, 31]. No values have been reported for SA-grown wires. Interestingly, the three films yielding similar values were grown on a TiO$_2$ substrate, while the film with a significantly lower value was grown on Al$_2$O$_3$. It is well known that such films have a different morphology, because of the hexagonal mesh of that substrate [31, 32].

3.5. Hard axis wires

3.5.1. TEM analysis

We also investigated the crystal structure of the hard nanowire. The cross-section of such a wire can be seen in Fig. 3.6(a). Here we can see the TiO$_2$ substrate at the bottom with the CrO$_2$ nanowire in between the SiO$_x$ mask. Like for the easy axis nanowire, the CrO$_2$ grew inside the 516 nm wide trench that was etched in the SiO$_x$ mask. The nanowire is 522 nm wide and 99 nm high at its widest and highest point, respectively. Similar to the easy wire, we observe faceted edges. Although these are less well defined than the faceted edges of the easy wire, we can still determine that the facets make roughly a 45° angle with the TiO$_2$ substrate. Furthermore, the CrO$_2$ only grows on top of the TiO$_2$ substrate, which means that there is again no overgrowth over the SiO$_x$ mask. An HR-TEM image of the interface between the TiO$_2$ substrate and the CrO$_2$ nanowire is shown in Fig. 3.6(b). The FFT of the region enclosed in the blue box is shown in Fig. 3.6(c). As expected, this pattern corresponds to the diffraction pattern of TiO$_2$ oriented along the [0 1 0] zone axis. The FFT of the area of CrO$_2$ inside the red box is depicted in Fig. 3.6(d). Here, we can see the same basic diffraction pattern corresponding to CrO$_2$ oriented along the [0 1 0] zone axis, but more diffraction spots are visible. These Moiré patterns belong
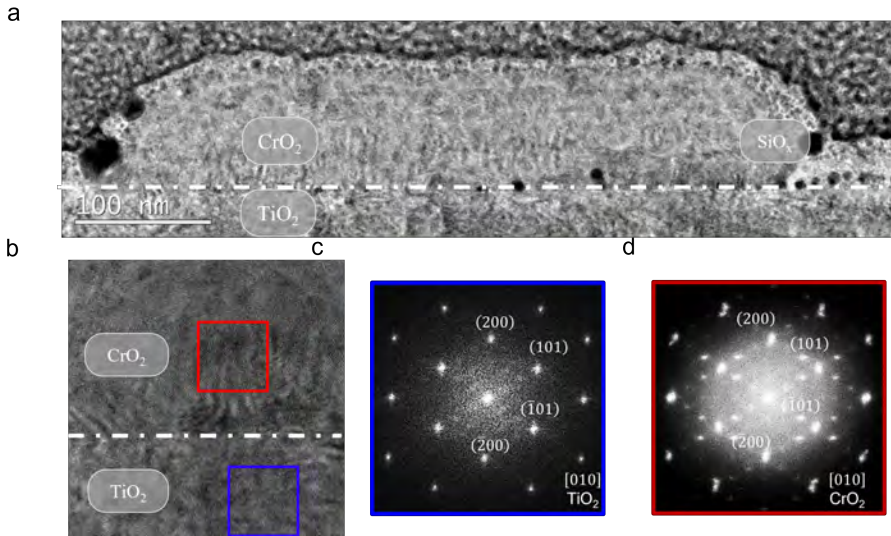
Figure 3.6: TEM inspection of a cross-section from the CrO$_2$ nanowire along the hard axis . (a) A low resolution TEM image of the TiO$_2$ substrate at the bottom and the partially grown CrO$_2$ nanowire in between the SiO$_x$ mask. (b) A high resolution TEM image of the interface between the TiO$_2$ substrate and the CrO$_2$ nanowire (c) The indexed FFT of the blue box in (b). The FFT shows the hexagonal diffraction pattern of the TiO$_2$ substrate with a [010] zone axis. (d) The indexed FFT of the red box in (b). The CrO$_2$ FFT has the same hexagonal diffraction pattern as in (c) but has extra diffraction spots that are rotated with respect to the main hexagonal diffraction pattern. The complete indexation of all the diffraction spots in (d) is given in the Appendix, sec. 3.8.6.

to rotated, double, and half reflections inside the crystal lattice. This indicates that the CrO$_2$ nanowire has many crystal domains that are all rotated with respect to each other at specific angles. This Moiré pattern is present in the entire hard wire. This is different from the easy wire, where only small crystal domains along the TiO$_2$ and CrO$_2$ interface had a different crystal orientation. A complete indexation of all diffraction spots in Fig. 3.6(d) can be found in the Appendix, sec. 3.8.6.

3.5.2. Magnetotransport

Fig. 3.7(a) shows the longitudinal MR behavior at 10 K for a *hard* wire (the same hard wire as measured in section 3.3), with H$_a$ the magnetic field along the wire axis, meaning $H_a \parallel I$, with I the applied current. Now, the results are different from both the 2 μm etched bars [14, 15] and from other SA grown hard wires of similar width [24]. Both in the etched bars and the SA grown wires, the MR showed a structure of a maximum followed by a bump, due to the several states the magnetic structure went through in the switching process. This includes an intermediate stripe-domain-like
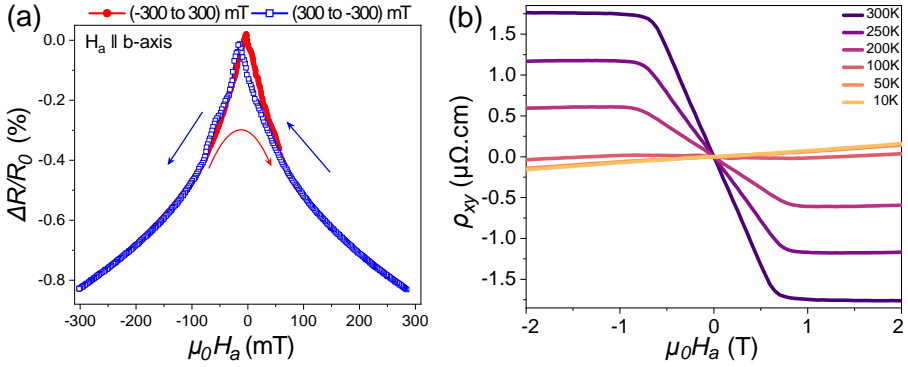
Figure 3.7: Magnetotransport measurements on a hard wire of width 610 nm. (a) In-plane longitudinal MR plot of a hard wire measured at 10 K. The external magnetic field H_a is parallel to the hard wire axis i.e. (H_a || b-axis [010]). The field is swept from -300 mT to 300 mT (filled red circles) and then from 300 mT to -300 mT (open blue squares). The arrows in blue and red show the sweep direction for the respective curves. (b) Hall resistivity as a function of external out-of-plane field for the same hard wire measured at various temperatures between 10 to 300 K. A 100 μA current is applied in both cases.

stable configuration, with the in-plane magnetization perpendicular to the wire (and therefore along the easy axis). Here, we observe a single maximum and only a small amount of hysteresis, indicating that the magnetization along the wire axis is subject to a single domain switching with only minimal additional magnetic disorder. This suggests that the shape anisotropy still plays a significant role in our 610 nm wide hard wire, unlike earlier SA-grown wires where magneto-crystalline anisotropy already dominated the shape anisotropy at a width of 350 nm.

Also the Hall measurements on the hard wire differ when comparing to the previous studies. Fig. 3.7(b) shows ρ_{xy} for different temperatures in a range from 300 K to 10 K. The behavior again follows Eq. (3.1) but the values for $\rho_{xy}(0)$ are almost 50% larger than for the easy wires of similar width. For $\rho_{xy}(0)$ at 300 K, in particular, we find a value of 1.75 $\mu\Omega$cm, compared to 1.1 $\mu\Omega$cm for the easy wire. The significance of this result is that it shows the hard-axis material to be different from the soft-axis material, as actually seen from the HR-TEM results described in sec 3.5.1. For a single type of material, Onsager's principle would say that $\rho_{xy} = -\rho_{yx}$ regardless of crystal orientation, as was indeed found for etched bars [29].

3.6. Wider hard wires

To further investigate the unexpected MR and AHE results obtained for the 610 nm hard wire, we fabricated wider hard wires, with widths of approximately 1.10 μm, 1.67 μm, and 2.26 μm. TEM images from cross-sections of these wires can be found
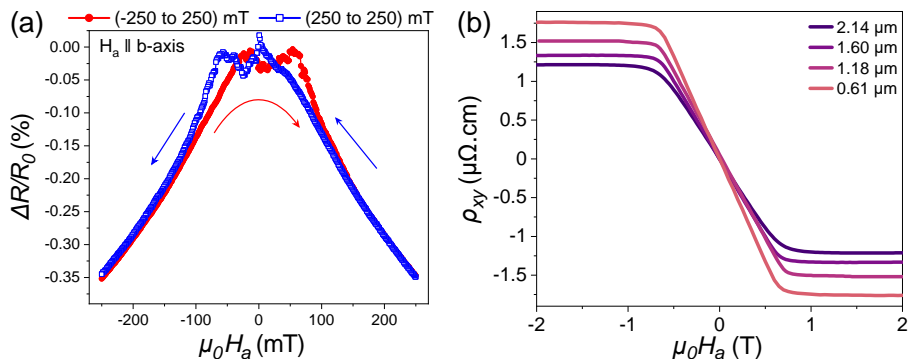
Figure 3.8: Magnetotransport measurements on hard wires of different widths. (a) In-plane longitudinal MR plot of a hard wire of width 1.1 µm measured at 10 K. The applied external magnetic field H_a is parallel to the hard wire axis i.e. (H_a || b-axis [010]). The field is swept from −250 mT to 250 mT (filled red circles) and then from 250 mT to −250 mT (open blue squares). The arrows in blue and red show the sweep direction for the respective curves. (b) Comparison of Hall resistivity as a function of external out-of-plane field for the hard wires of different widths measured at 300 K shows a clear trend of $\rho_{xy}(300)$ decreasing as the width increases.

in the Appendix, sec.3.8.5. Although no significant morphological differences were observed between hard wires of varying widths, including the wire from section 3.5.1, the transport measurements revealed a dependence on the width. Fig. 3.8(a) shows typical MR behavior of the 1.10 µm wire at 10 K. Here, we see the double maximum structure which is similar to the MR behavior observed in previous studies for films and wires.[14, 15, 24] This suggests that at a width of around 1 µm, the point is reached where magnetocrystalline anisotropy dominates shape anisotropy. We observe a similar trend in the Hall data. Fig. 3.8(b) compares the Hall resistivity at 300 K on hard wires of different widths. As the width increases, $\rho_{xy}(0)$ at 300 K decreases and gets closer to the value obtained for the easy wire described in sec 3.4.2. It is likely that for hard wires wider than 2 μm, the behavior of the hard and easy wires becomes comparable, and that we are then essentially in the film regime. This can be understood from a growth point of view, since typical crystallites in films have dimensions of the order of a few μm. A trench of that width will have less confining influence on the growth.

3.7. Conclusion

In summary, we have shown that we can grow high quality CrO_2 nanowires using the Selective Area (SA) growth on a TiO_2 substrate along both the c-axis (easy axis) and the b-axis (hard axis). For the best results, a high degree of control over the etching of the trench is required. Growing hard wires is more challenging due to

higher lattice mismatch between TiO$_2$ and CrO$_2$ along the b-axis. High-resolution TEM imaging shows that the material has a different morphology on the nanoscale, with the presence of multiple crystal domains that are rotated with respect to each other. The electrical and magnetic properties of the wires generally are in line with the picture coming from TEM.

Our wires are found to be highly conductive, in particular the easy wires, with a room temperature value for ρ_{300} of 120 µΩcm and an RRR of 21. Hard wires are less conducting , as can be expected from the TEM results. The same is true for magnetotransport properties where we find very sharp switching for quite wide easy wires, and different behavior for hard wires. Of special interest is the difference in the AHE for both wire types, which once more reflects the difference in morphology. When trenches become wider than roughly 2 µm, the differences between (easy) c-axis wires and (hard) b axis wires disappear.

3.8. Appendix

3.8.1. Methods: TEM sample preparation and measurements

The cross-sections of the various nanowires were prepared for TEM inspection using a Focused Ion Beam (FIB) system (The Thermo Scientific™ Helios™ G4 CX DualBeam™ System). The acceleration voltage for the ion beam was set at 30 kV. Before starting the FIB process, a thin layer of gold was sputtered on top of the samples in order to prevent chairing effects on the insulating TiO_2 substrate. During the FIB process the CrO_2 nanowire was protected by a platinum layer, deposited in situ using a MultiChem™ system. Tungsten was used whenever platinum was unavailable. The TEM measurements were carried out using a Thermo Scientific™ Titan 60-300 cubed TEM, operated at 300 kV. The TEM samples were oriented in a zone-axis using a double tilt holder. The HR-TEM images were recorded using a Thermo Scientific™ Ceta-16M CMOS camera.

3.8.2. Crystal structure of CrO$_2$ and TiO$_2$
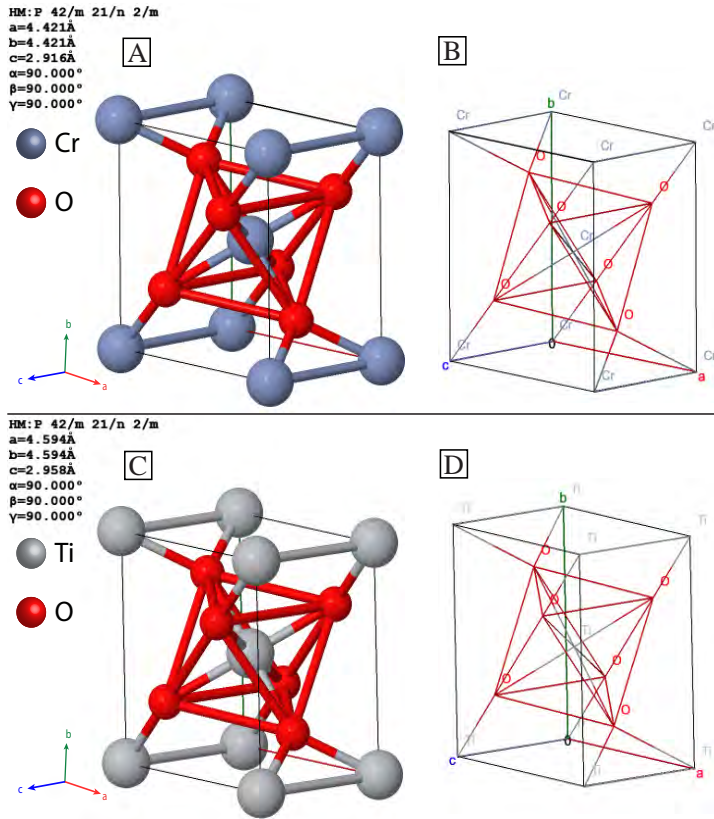
Figure 3.9: The unit cell for CrO$_2$ (a-b) and TiO$_2$ (c-d), respectively. Both materials have a rutile structure and are described by a body-centered cubic (bcc) tetragonal unit cell. The lattice parameters of the CrO$_2$ unit cell are a = b = 4.421 Å and c = 2.916 Å. [33] There are two Cr atoms in the cell, at positions (0,0,0) and $(\frac{1}{2},\frac{1}{2},\frac{1}{2})$. Oxygen atom form octahedra around Cr-atoms and are both side-sharing and corner-sharing. The four oxygen atoms are at [u,u,0] and their symmetric equivalents; where $u = 0.303$. The lattice parameters of the TiO$_2$ unit cell are a = b = 4.594 Å and c = 2.958 Å. [34] The chromium atoms are indicated in purple, the titanium atoms in grey, and the oxygen atoms in red. These models are generated using Eje-Z [35, 36]

3.8.3. Growth morphology and correlation between the width of a nanowire and the direction of growth

CrO_2 crystallites nucleate uniformly at the bottom of the trench on top of TiO_2 surface which merge together to form a continuous surface covering the full width of the trench as shown in Fig. 3.10. The vertical growth then occurs epitaxially. Important to note that we do not get pandeo-epitaxy type of growth with internal voids or dislocations as reported in a previous study [25]. In hindsight, this may have been caused by incomplete etching of the trench bottom. Depending on the direction of growth, the actual width of the wires varies. For the wires along [001] and [010] the width is same as the width of the trench and we do not see any lateral overgrowth on the SiO_2 surface outside the trench. For any other intermediate direction of nanowires, we found lateral overgrowth outside the trench wall, thereby making the actual width of wires larger than the trench width as shown in Fig. 3.11, 3.13 and in Table 3.2. As we increase the time of growth the sideways growth also increases.

a

b
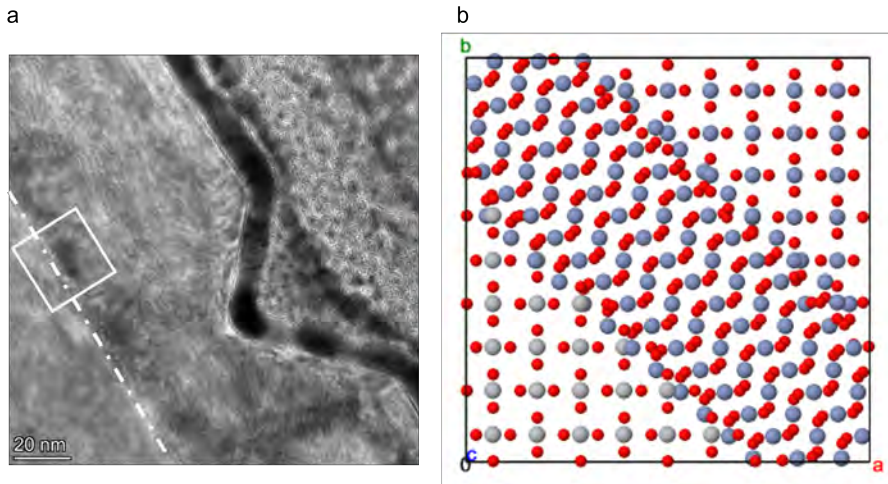
Figure 3.10: (a) TEM image of the same easy wire as depicted in Fig. 3.4(a) in the main text. The CrO_2 wire covers the entire surface of the trench. However, there are areas with different contrast along the interface between the TiO_2 substrate and the CrO_2 wire. A high-magnification TEM image of the area in the white box is displayed in Fig. 3.4 (main text). (b) An atomic model of the interface between the TiO_2 substrate and the CrO_2 wire. The model represents the area in Fig. 3.4(b) (main text), where there are two CrO_2 crystal domains with different orientations.
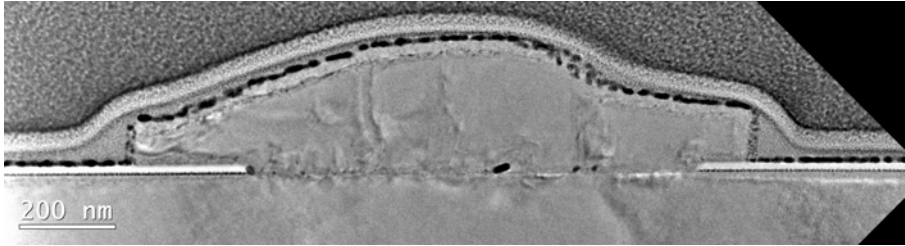
Figure 3.11: Low magnification TEM image of a CrO$_2$ nanowire where the z-axis is rotated 30° from the easy axis. The nanowire has grown over the SiO$_x$ mask. The nanowire is 1280 nm wide even though the mask is only 925 nm wide.
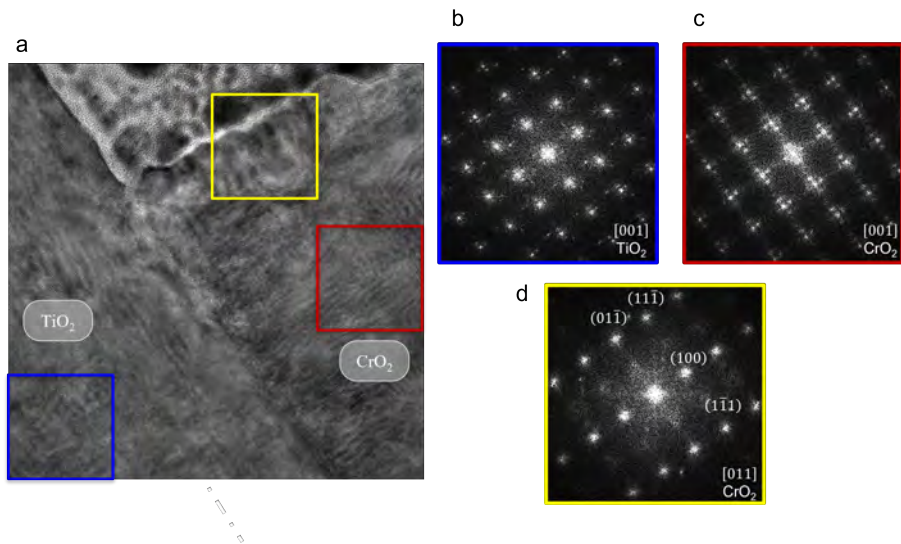
Figure 3.12: High-resolution TEM image of an easy CrO$_2$ nanowire on top of a TiO$_2$ substrate at the bottom. The center of the CrO$_2$ nanowire (red box) has grown epitaxially on the TiO$_2$ substrate. The FFT of both regions (b-c) shows that both the CrO$_2$ wire and the TiO$_2$ substrate (blue box) are oriented in the [001] zone axis. The edge of the CrO$_2$ nanowire (yellow box) has a different crystal orientation. The FFT of this region (d) is oriented in the [011] zone axis.

3.8.4. The height and width of the CrO_2 nanowire as measured by TEM cross-section

The length and height of the CrO_2 nanowires are measured using TEM images:

Angle (°)	width trench	width wire	max-height wire	min-height wire
0	936	936	177	71
30	925	1280	272	106
45	946	1234	275	175
90	930	982	252	213

Table 3.1: The length and height in nanometers of the nanowires from sample AG_2 for 4 different angles.
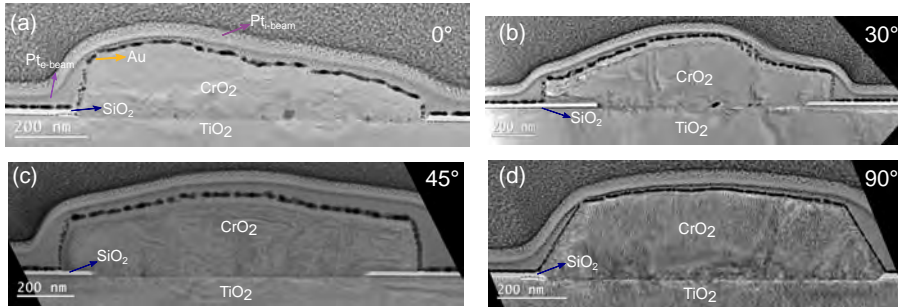
Figure 3.13: TEM image of the sample AG_2 shows the CrO_2 nanowires grown along 4 different angles (0°, 30°, 45°, 90°) with respect to the (100) oriented TiO_2 substrate, where [001] is along the horizontal direction. TiO_2 is at the bottom part, SiO_2 is the narrow white region on both sides of the trench at the interface of TiO_2 and CrO_2 and has been shown with blue arrow while CrO_2 is at the top part. (a) shows the CrO_2 nanowire grown along 0° which is the easy-axis of growth. (b) is at 30° (c) is at 45° and (d) shows the hard-axis CrO_2 nanowire. Both (b) and (c) shows lateral overgrowth of CrO_2 over SiO_2 while (a) and (d) don't show lateral overgrowth.

AG_2 was annealed for 1 hr at 390°C in O_2 at 140 sccm and grown at 260°C for 30 min.

Angle	width trench	width wire	max-height wire	min-height wire
0	514	530	82	41
15	498	528	75	65
30	736	926	77	72
45	498	547	83	80
60	506	559	83	73
90	502	529	104	96

Table 3.2: The length and height in nanometers of the nanowires from sample AJ$_2$ for 6 different angles.
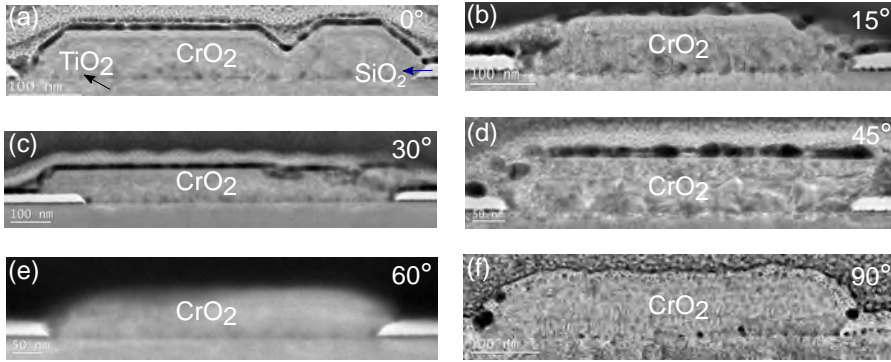
Figure 3.14: TEM image of the sample AJ$_2$ shows the CrO$_2$ nanowires grown along 6 different angles (0°, 15°, 30°, 45°, 60° and 90°) w.r.t. TiO$_2$ substrate where [001] is along the horizontal direction. TiO$_2$ is at the bottom part, SiO$_2$ is the narrow white region on both sides of the trench at the interface of TiO$_2$ and CrO$_2$ and has been shown with blue arrow while CrO$_2$ is at the top part. (a) shows the CrO$_2$ nanowire grown along 0° which is the easy-axis of growth. (b) is at 15° (c) is at 30° (d) is at 45° (e) is at 60° and (f) is at 90° which is the hard-axis of CrO$_2$ nanowire.

AJ$_2$ was annealed for 1hr at 390°C in O$_2$ at 140 sccm and grown at 260°C for 15 min.

3.8.5. TEM images of wider hard nanowires (width $\geq 1\mu m$)

The height and width of the CrO$_2$ nanowires is measured using TEM images:

AQ$_5$ was annealed for 1hr at 390°C in O$_2$ at 140 sccm and grown at 260°C for 35 min.

width trench	width wire	max-height wire	min-height wire
1103	1208	369	332
1672	1810	428	396
2255	2361	472	421

Table 3.3: The height and width in nanometers of the nanowires from sample AQ_5 for three different trench widths.
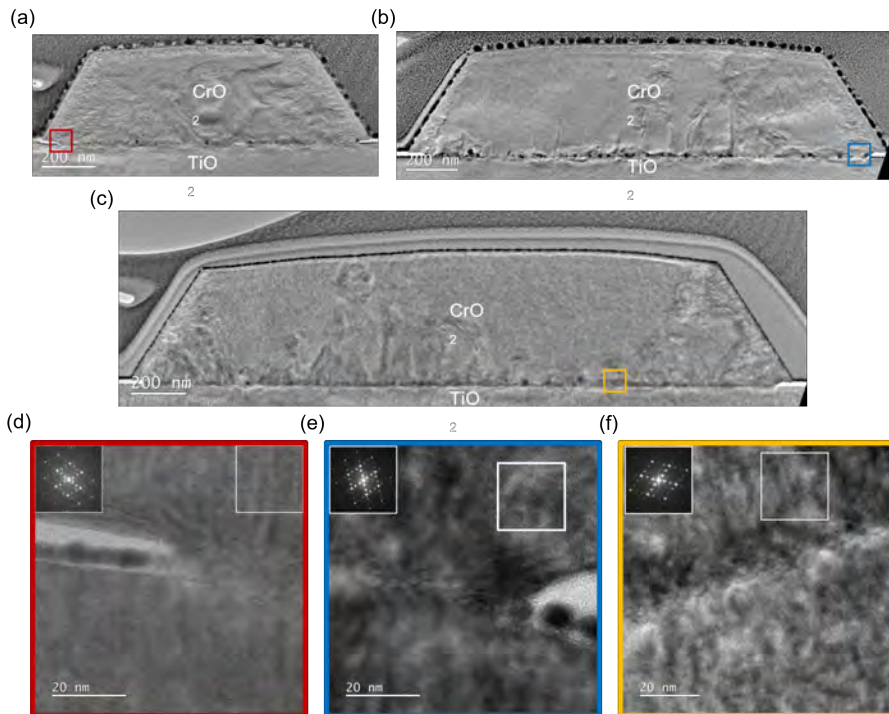
Figure 3.15: TEM images of the sample AQ_5 shows CrO_2 nanowires oriented along the hard axis (90° w.r.t. the [001] TiO_2 substrate). In the first three images (a-c), the TiO_2 substrate is at the bottom, with the CrO_2 nanowire on top. (a) has a trench width of 1103 nm, (b) has a trench width of 1672nm, and (c) has a trench width of 2255 nm. (d-f) HT-TEM images from the CrO_2 and TiO_2 interface for all three nanowires depicted in a-c. The inset shows the FFT of the areas indicated in white. The same Moiré pattern can be seen for all three nanowires. Indicating no change in the CrO_2 morphology for the different nanowire widths.

3.8.6. Indexation of the fast Fourier transform shown in Fig. 3.6(d) in main text

Fig. 3.16 contains a FFT of a hard axis CrO$_2$ nanowire with a zone-axis of [010]. The FFT contains the six diffraction spots belonging to the (200), (101) and ($\bar{1}$01) family of planes and their inverse. These diffraction spots in this main grouping are denoted by the red letters (A-F). The rest of the diffraction spots belong to the remaining family of planes, listed in the table 3.4-b and labeled by the numbers (1-8). The numbered diffraction spots with the same color all belong to the diffraction grouping. Each grouping of diffraction spots is rotated and/or magnified with respect to the main diffraction grouping (Red A-F). The rotation and magnification factor for each diffraction grouping are listed in table 3.4-a. A clockwise rotation is denoted by a positive angle and a anti-clockwise rotation is denoted by a negative angle.
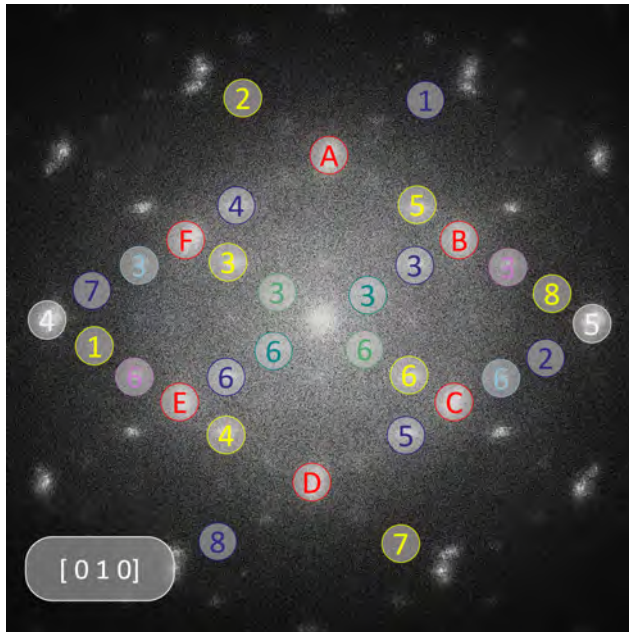
Figure 3.16: Indexation of the FFT of a hard CrO$_2$ nanowire with a [010] zone-axis

(a) Grouping	Rotation Angle (°)	Magnification
Red	0	1x
Yellow	-56.7	1x
Dark blue	56.7	1x
Light green	-56.7	2x
Dark green	56.7	2x
Light Blue	-74.6	0.5x
Purple	74.6	0.5x
White	0	0.5x

(b) Letter	(hkl)		Number	(hkl)
A	(200)		1	(20$\bar{1}$)
B	(101)		2	(201)
C	($\bar{1}$01)		3	(100)
D	($\bar{2}$00)		4	(00$\bar{1}$)
E	($\bar{1}$0$\bar{1}$)		5	(001)
F	(10$\bar{1}$)		6	($\bar{1}$00)
			7	($\bar{2}$0$\bar{1}$)
			8	($\bar{2}$01)

Table 3.4: Reference tables for the diffraction indexation of the FFT in Fig. 3.16. (a) Table with the relative rotation and magnification of a diffraction grouping compared to the main diffraction grouping, denoted with the red letters (A-F). (b) Table with the indexation of the family of planes. The main diffraction spots are detonated with the red letters (A-F). The secondary diffraction spots are denoted with by the numbers (1-8).

References

[1] Soulen, R. J. et al. Measuring the Spin Polarization of a Metal with a Superconducting Point Contact. Science **282**, 85–88 (1998).

[2] Zhu, Z. H. et al. Anomalous antiferromagnetism in metallic RuO_2 determined by resonant x-ray scattering. Physical Review Letters **122**, 017202 (2019).

[3] Šmejkal, L., González-Hernández, R., Jungwirth, T. & Sinova, J. Crystal time-reversal symmetry breaking and spontaneous Hall Effect in collinear antiferromagnets. Science Advances **6**, eaaz8809 (2020).

[4] Fujiwara, K. et al. $5d$ iridium oxide as a material for spin-current detection. Nature Communications **4**, 2893 (2013).

[5] Zhang, Z. et al. The high magnetoresistance performance of epitaxial half-metallic CrO_2-based magnetic junctions. Phys. Chem. Chem. Phys. **25**, 1848 (2023).

[6] Qian, L. J., Zhou, S., Wanga, K. & Xiao, G. Resistance of single domain walls in half-metallic CrO_2 epitaxial nanostructures. Nanoscale **13**, 20034 (2021).

[7] Zhang, Z. et al. Ultralow Gilbert damping in CrO_2 epitaxial films. Physical Review B **102**, 14454 (2020).

[8] Qian, L. J., Chen, W., & Xiao, G. Spin curvature induced resistivity in epitaxial half-metallic CrO_2 thin films. Nanoscale **12**, 3958 (2020).

[9] Coey, J. M. D. & Venkatesan, M. Half-metallic ferromagnetism: Example of CrO_2 (invited). Journal of Applied Physics **91**, 8345 (2002).

[10] Kämper, K. P., Schmitt, W., Güntherodt, G., Gambino, R. J. & Ruf, R. CrO_2 - a New Half-Metallic Ferromagnet ? Physical Review Letters **59**, 2788 (1987).

[11] Li, X. W., Gupta, A., McGuire, T. R., Duncombe, P. R. & Xiao, G. Magnetoresistance and Hall Effect of chromium dioxide epitaxial thin films. Journal of Applied Physics **85**, 5585–5587 (1999).

[12] Gupta, A., Li, X. W. & Xiao, G. Magnetic and transport properties of epitaxial and polycrystalline chromium dioxide thin films (invited). Journal of Applied Physics **87**, 6073–6078 (2000).

[13] Miao, G., Xiao, G. & Gupta, A. Variations in the magnetic anisotropy properties of epitaxial CrO_2 films as a function of thickness. Physical Review B **71**, 094418 (2005).

[14] König, C. et al. Micromagnetism and magnetotransport properties of micron-sized epitaxial CrO_2(100) wires. Physical Review B **75** (2007).

[15] Anwar, M. S. & Aarts, J. Anomalous transport in half-metallic ferromagnetic CrO_2. Physical Review B **88**, 085123 (2013).

[16] Anwar, M. S. & Aarts, J. Inducing supercurrents in thin films of ferromagnetic CrO_2. Superconducting Science and Technology **24**, 024016 (2011).

[17] Keizer, R. S. et al. A spin triplet supercurrent through the half-metallic ferro-magnet CrO_2. Nature **439**, 825 (2006).

[18] Gönnenwein, S. T. B. et al. Planar Hall Effect and magnetic anisotropy in epitaxially strained chromium dioxide thin films. Applied Physics Letters **90**, 142509 (2007).

[19] Miao, G., Xiao, G. & Gupta, A. Influence of substrate treatment on the growth morphology and magnetic anisotropy of epitaxial CrO2 films. Physica Status Solidi (a) **203**, 1513 (2006).

[20] Gupta, A., Li, X. W., Guha, S. & Xiao, G. Selective-area and lateral over-growth of chromium dioxide (CrO_2) films by chemical vapor deposition. Applied Physics Letters **75**, 2996–2998 (1999).

[21] Zou, X. & Xiao, G. Magnetic domain configurations of epitaxial chromium dioxide (CrO_2) nanostructures. Applied Physics Letters **91**, 113512 (2007).

[22] Zou, X. & Xiao, G. Half-metallic chromium dioxide (CrO_2) nanostructures and field-dependent magnetic domain evolution. Journal of Applied Physics **103**, 07D710 (2008).

[23] Zou, X., Xiao, G., Huang, S., Chen, T. & Chien, C.-L. Magnetotransport properties of polycrystalline and epitaxial chromium dioxide nanowires. Journal of Applied Physics **103**, 07D710 (2008).

[24] Zou, X. & Xiao, G. Electronic transport and magnetoresistance in polycrys-talline and epitaxial CrO_2 nanowires. Physical Review B **77**, 054417 (2008).

[25] Singh, A., Jansen, C., Lahabi, K. & Aarts, J. High-Quality CrO_2 Nanowires for Dissipation-less Spintronics. Physical Review X **6**, 041012 (2016).

[26] Chen, W., Qian, L. & Xiao, G. Resistance of domain-wall states in half-metallic CrO_2. Physical Review B **98**, 174402 (2018).

[27] See Supplemental Material at
http://link.aps.org/supplemental/xxx for additional details on the growth mor-phology of the nanowires as indicated in the main text.

[28] Ye, J. et al. Berry phase theory of the Anomalous Hall Effect: Application to Colossal Magnetoresistance manganites. Physical Review Letters **83**, 3737 (1999).

[29] Yanagihara, H. & Salamon, M. B. Skyrmion strings and the Anomalous Hall Effect in CrO_2. Physical Review Letters **89**, 187201 (2002).

[30] Branford, W. R. et al. Coexistence of universal and topological Anomalous Hall Effects in metal CrO_2 thin films in the dirty limit. Physical Review Letters **102**, 227201 (2009).

[31] Anwar, M. S., Czeschka, F., Hesselberth, M., Porcu, M. & Aarts, J. Long-range supercurrents through half-metallic ferromagnetic CrO_2. Physical Review B **82**, 100501R (2010).

[32] Sousa, P. M. et al. Influence of growth temperature and carrier flux on the structure and transport properties of highly oriented CrO_2 on Al_2O_3(0001). Chemical vapor Deposition **13**, 537 (2007).

[33] CrO_2 crystal structure: Datasheet from "Pauling File Multinaries Edition – 2012" in Springer Materials (https://materials.springer.com/isp/crystallographic/docs/sd_-0534987) (2012). URL https://materials.springer.com/isp/crystallographic/docs/sd_0534987. Copyright 2016 Springer-Verlag Berlin Heidelberg & Material Phases Data System (MPDS), Switzerland & National Institute for Materials Science (NIMS), Japan.

[34] TiO_2 crystal structure: Datasheet from "Pauling File Multinaries Edition – 2012" in Springer Materials (https://materials.springer.com/isp/crystallographic/docs/sd_-0304559) (2012). URL https://materials.springer.com/isp/crystallographic/docs/sd_0304559. Copyright 2016 Springer-Verlag Berlin Heidelberg & Material Phases Data System (MPDS), Switzerland & National Institute for Materials Science (NIMS), Japan.

[35] Bernal, S. et al. High-resolution electron microscopy investigation of metal–support interactions in Rh/TiO_2. J. Chem. Soc., Faraday Trans. **92**, 2799–2809 (1996). URL http://dx.doi.org/10.1039/FT9969202799.

[36] Pérez-Omil, J. Tem-uca user global server (2018). URL http://www.temserver.uca.es. University of Cádiz.

4

Moving Domain Walls in Permalloy and CrO$_2$ Nanowires

The manipulation of domain walls (DW) in ferromagnets using current or pulse-driven techniques has been the subject of research for almost two decades, and its fundamental tenets have been extensively explored. One significant limitation is the relatively high threshold current (J_c) of 10^{12} A/m^2 for moving DW in traditional ferromagnets which are not fully spin-polarized, resulting in substantial Joule heating. In contrast, half-metallic ferromagnets like CrO$_2$ holds the promise to lower J_c. In this work, we built a high frequency setup to allow injection of current pulses and investigated the pinning and depinning of DW using a triangular constriction (notch) in two ferromagnets: Permalloy, as a reference material and CrO$_2$ to study a fully spin-polarized material. We have also characterized domain wall resistance in CrO$_2$, and found it to decrease from 25 mΩ at 10 K to 18.2 mΩ at 80 K, then rise to roughly 23 mΩ at 300 K. We find that in general, the the notch size affects J_c. While a deep notch (> 50% of wire width) increases the DW resistance, it also leads to strong pinning potential for both Py and CrO$_2$ samples which makes depinning difficult. Additionally, CrO$_2$ devices are more sensitive to the notch depth, with a 5% deeper notch on a wire of similar size results in a 2.5 times higher J_c. The depinning critical current densities in CrO$_2$ are comparable to that of Py samples and are unaffected by strong spin polarization.

4.1. Introduction

Over the past two decades, spintronics has been at the forefront of research in the pursuit for CMOS alternatives for next-generation 3D data storage and logic devices [1]. One such approach is a "racetrack" memory that uses magnetic domains to store information [2]. Architectures relying on magnetic domain walls leverage the benefits of high velocity, high density, non-volatility and flexible design of domain walls to process and store information. These systems rely on controlled movement between precise distinct positions of domain walls in magnetic elements, such as a ferromagnetic wire, where a domain wall (DW) is formed at the boundaries between magnetic domains magnetized in opposite directions. Patterned geometrical traps, artificial constrictions, or others, are utilized to precisely locate DW and produce an attractive pinning potential. Traditionally magnetic fields were employed to manipulate DWs. A magnetic field however, cannot facilitate the simultaneous movement of many domain walls in the same direction, making it unsuitable for DW-motion-based memory systems. Since the pioneering work of Berger *et al.* on current-driven domain-wall motion [3], the spin-transfer torque has been recognized to be useful in manipulating magnetization in nanomagnets.

Most of the studies on current-induced DW motion have been done on conventional ferromagnets like permalloy (Py) or Co. A threshold current J_c on the order of 10^{12} A/m^2 was observed for DW-motion in Py nanowires [4] and Py rings [5]. Kläui et al. also showed that pulse injections can transform domain structure from a vortex wall to a transverse wall. Others have also made similar observations [6]. An important drawback of these studies is the high J_c which leads to increased nanowire temperature due to Joule heating [7]. In severe instances, nanowire temperatures can even reach the Curie temperature T$_C$. In comparison, CrO$_2$, a half-metal ferromagnet with 100% spin polarization holds the promise to lower J_c [8]. There have been several attempts with limited success to investigate the pinning and depinning of DW in CrO$_2$ [9, 10]. Biehler et. al fabricated CrO$_2$ wire of widths (0.5-2) μm from full films using Ar-etching and found that a pulse of duration 10 μs corresponding to a J_c of 5×10^{10} A/m^2 was required to alter the magnetic domain configurations at room temperature. However, the pulses led to increase in the sample temperatures beyond T$_C$. More recently, Chen et al. investigated the DW resistance in an anvil-shaped epitaxial CrO$_2$ structure. Their structure allowed the generation and annihilation of a DW by measuring the resistance jump between a single-domain state and a domain-wall state through field sweeps [11]. However, a precise control and manipulation of DW through currents on CrO$_2$ has not yet been performed.

Experiments on moving domain walls (DWs) can take different forms. One way is to induce a DW in a wire F$_1$ by sending a current pulse through a cross-wire,

inducing the DW in F_1 by the Oersted fields of the current. By also applying a current in F_1, the DW can then be moved [12, 13]. Here, we address a slightly different question. Using a ferromagnetic wire with a narrow triangular constriction (a so-called 'notch'), we first pin a DW in the constriction by applying small in-plane magnetic fields. We detect the presence of the DW by measuring the anisotropic magnetoresistance (AMR) of the wire and observing a change in resistance when the DW is caught. Then we use pulsed currents to find the critical current I_c that depins the DW again. A magnetic field can be applied to investigate its effects on I_c. In this work, we investigate the pinning and depinning of domain walls on Py and CrO_2 nanowires and compare the results.

4.2. Experimental setup

The MR measurements were performed in a Physical Property Measurement System (PPMS) that could be cooled down to a base temperature of 2 K. We used a Keithley model 6221 low Noise Precision AC/DC Current Source to provide dc currents and a Keithley model 2182A digital nanovoltmeter to measure voltage. Firstly, two-probe measurements were performed at room temperature to characterize a new sample and confirm that all contact leads and connected nanostructures were intact. Next, we connected the sample in a four-point method as shown in Fig. 4.1(a), with the inner leads for the voltage and the outer leads for the current, allowing a direct measurement of sample resistance without the contact wire resistance. Samples were routinely cooled down to 10 K for the measurements. For the pulsed current measurements, we designed and developed a high-frequency pulse generator in-house. The schematics for this will be presented later.

We used two different ferromagnets for the experiments. Permalloy (Py) was used as a reference material, because much is known about DW motion in this weakly anisotropic material with medium-sized spin-polarization. CrO_2 was used to study the situation of a fully spin-polarized material, for which actually only few experiments exist. We used similar dimensions for the Py and CrO_2 wires. Below, we first discuss the sample fabrication, the characterization of the notched wires by magnetotransport measurements, and we present the setup for generating current pulses. The latter comes in two flavors. With the initial design that reached current densities around 2×10^{11} [A/m^2], DWs could be depinned in the Py wire, but not in the CrO_2 wire. The modified design increased the applied current by an order of magnitude, and allowed depinning to be observed in both wires.

4.2.1. Sample fabrication

CrO_2 devices were grown using the Selective Area growth technique via Chemical Vapor Deposition as described in detail in sec. 3.2. We also fabricated Permalloy (Py) nanowires with Cu contacts for pulse measurements as a standard device to test our experimental setup. To make Py devices, we first patterned the desired nanostructures on a Si substrate that has a 300 nm wet thermal oxide layer on top, using electron beam lithography. The Py was then deposited using e-beam evaporation at a very low pressure of 8×10^{-9} mbar, which was followed by a lift-off process to obtain the central Py structure as shown in Fig. 4.3 (in gray). Subsequently, to make Cu contacts on the Py nanowire, we patterned the contacts using e-beam lithography. This was followed by Ar etching to remove the top dead layer of Py before e-beam evaporation of Cu and lift-off steps. For both the CrO_2 and Py devices, the notch was made in the center of the nanowire using Focused Ion Beam (FIB) milling. In our samples, we used two types of notch : single notches (a triangular shape pointing inward from one side of the wire) or double notches (two triangles pointing inward from the two sides). They act as artificial pinning centers for the domain walls.

4.2.2. Sample characterization

CrO_2 devices: We designed a CrO_2 device as shown in Fig. 4.1(a) consisting of a central CrO_2 wire of width = 500 nm, and length between the inner contact leads (V^+ and V^-) = 1.5 μm. The centre of the wire has a double notch where the width of the CrO_2 wire had been reduced to 91 nm. The left end the CrO_2 wire consists of a large contact pad. It ensures that the central CrO_2 wire has a different switching field than the contact pad. This is necessary for the nucleation of the domain wall in the contact pad, which then propagates along the wire through the notch (if not pinned) and terminates at the right end of the wire, which has a pointed shape. The movement of the domain wall is always from the contact pad to the wire, regardless of the direction of the magnetic field, as it is energetically favorable. Conversely, it is energetically prohibited for the domain wall to travel from the wire to the contact pad, preventing its movement from the right end of the wire to the left.

The growth of the CrO_2 nanowire was immediately followed by electrical characterization. We measured the resistance R as a function of the temperature T of the nanowire before and after FIB milling. As seen in Fig. 4.1 (b) (green curve), the resistance at room temperature (300 K) is 96.2 Ω which corresponds to a resistivity ρ_{300} of 190 $\mu\Omega$.cm while the resistance at low temperature (10 K) is 6.9 Ω, corresponding to ρ_{10} of ~ 12 $\mu\Omega$.cm. This gives a residual-resistivity ratio (RRR, the ratio between ρ_{300} and ρ_{10}) of about 16. Next, using FIB, we made a double notch and
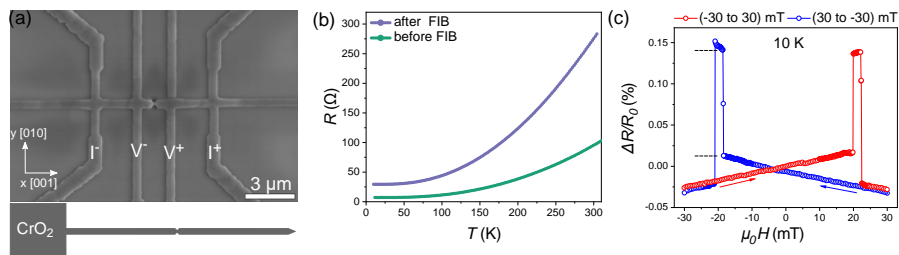
Figure 4.1: (a) SEM image of a CrO_2 device used in this study (see details in the text). The wire axis is along the [001] direction. The four contact leads (I^+, I^-, V^+ and V^-) are used for the four-point resistance measurement. The contacts leads are also made of CrO_2. The center of the wire contains a narrow constriction of the double notch type made with using Focused Ion Beam milling. The bottom part of the image shows the full design of the CrO_2 wire where the contact pad is at the left end of the wire and the right end has a pointed edge termination. (b) Resistance of the CrO_2 device as a function of temperature from 300 K down to 10 K before making the notch (green) and after the notch (purple). (c) In-plane longitudinal magneto-resistance along [001] as measured at 10 K by sweeping the magnetic field from -30 mT to $+30$ mT and back. R_0 was measured to be 28.34 Ω. The step size is 0.5 mT. The interval between the dotted lines in (c) defines Δr_{DW}. The current used in both resistance and MR measurement is 100 μA.

measured $R(T)$ again (Fig. 4.1(b) purple curve). We notice a rise in the resistance both at room temperature and at 10 K. The RRR value is now ~ 9. We estimated the resistance of the notched part of the wire. Assuming that the ρ_{10} stayed the same, we get a resistance R_{notch} of 3.84 Ω. But, the total resistance of the wire after FIB is around 29 Ω which suggests either some FIB damage, which would increase resistivity, or a decrease of thickness (the same). The observed reduction in RRR, a measure of crystal quality can then be attributed to the damage from the Ga ions to CrO_2 nanowire during FIB process.

We further performed magnetoresistance (MR) measurements at 10 K. Fig. 4.1(c) shows the longitudinal MR behavior defined as $[R(\mu_0 H) - R_0]/R_0 = \Delta(R)/R_0$, where $\mu_0 H$ is the magnetic field along the wire axis [001] which is also the magnetic easy-axis of CrO_2 and $R(0) \equiv R_0$ is the resistance at zero field. The value of R_0 in Fig. 4.1(c) is 28.34 Ω. Initially, the field was kept at -500 mT so that the magnetization direction of both the wire and the contact pad was along the negative x-axis. We then reduced the field to -30 mT before starting the measurement. We swept the field in steps of 0.5 mT until 10 mT. After that the step size was decreased to 0.1 mT from 10 mT until 25 mT. Thereafter, the step size was increased to 0.5 mT until we reached 30 mT. This completes the first half of the measurement (blue curve in Fig. 4.1(c)). The field was then increased to $+500$ mT to saturate the magnetization direction of both the wire and contact pad, but now along x-axis, and the same steps of field sweep were done, now from $+30$ mT until -30 mT (red curve in fig. 4.1(c)) to finish the loop.

The MR loop shows a high resistance state between 19.9 mT and 22.1 mT and between −18.5 mT and −20.9 mT. This can be understood by contemplating the magnetic domain state. The magnetic easy axis of CrO$_2$ is along [001], which is parallel to the wire axis of our device. As mentioned above, the difference in the size of the wire and contact pad ensures different switching fields for them. In this case the contact pad will switch magnetization at lower fields because it has a larger area. At ±500 mT, both the central wire and the contact pad have a uniformly aligned parallel magnetization along the ±x axis respectively. At -30 mT, the magnetization is still homogeneous, and the resistance measured between V$^+$ and V$^−$ is low. Next, we gradually increase the field to 30 mT. The magnetization of the contact pad starts to switch, and at 19.9 mT, the wire starts to switch, meaning a DW propagates along the length of the wire. The field helps in the movement of the DW and it gets pinned at the notch, leading to the higher resistance R_{high}. The DW remains pinned with further increase of the field until 22.1 mT. Beyond that, the DW depins and moves out of the wire at the pointed end. The resistance returns to its lower value R_{low} between 22.2 mT and 30 mT. Similarly, when we sweep the field from +30 mT to −30 mT, we obtain a high resistance state between −18.5 mT and −20.9 mT. The slight asymmetry in the (de)pinning fields is due to the asymmetry in the device coming from the edges of the wire and the notch.

Next, we performed MR measurements at different temperatures and calculated the evolution of $\Delta r_{DW} = R_{high} − R_{low}$ for each temperature. Fig. 4.2 (a) and (b) show MR measurements done at 50 K and 100 K as an example. Fig. 4.2(c) gives the plot of Δr_{DW} as a function of temperature from 10 K to 300 K. We find a weak temperature dependence over the entire temperature range. Δr_{DW} decreases slightly from 25.7 ± 1.5 mΩ at 10 K to 18.2 ± 1.1 mΩ at 80 K. Above 80 K, Δr_{DW} appears to increases again reaching a value of around 23 $m\Omega$ at 300 K. Fig. 4.2 (d) shows temperature dependence of ratio $\Delta r_{DW}/R_0$. We found that as temperature increased $\Delta r_{DW}/R_0$ decreased monotonically.

We calculate the area of the DW of CrO$_2$ wire (see 4.1 (a)) from the depth of notch (d) of 91 nm and wire thickness (t) of 60 nm. Then, the resistance-area product for the DW is defined as $RA_{DW} = \Delta r_{DW} \times d \times t$. At 10 K, we obtain RA_{DW} of 1.4 × $10^{-16}\,\Omega\text{m}^2$, which is comparable to the values reported for LSMO nanostructures [14] and other conventional ferromagnets like Co and Py [15]. However, this value is around 3 orders of magnitude smaller than RA_{DW} of 0.65 × $10^{-13}\,\Omega\text{m}^2$ at 77 K reported by ref. [16].

It is instructive to compare Δr_{DW} and $\Delta r_{DW}/R_0$ data with experiments reported by Chen *et al.*[11], who performed measurements on a slightly different geometry. Rather than a notch in the middle of a wire, they used a CVD-grown structure with the shape of a sharp point into anvil. A DW can be caught at that point contact
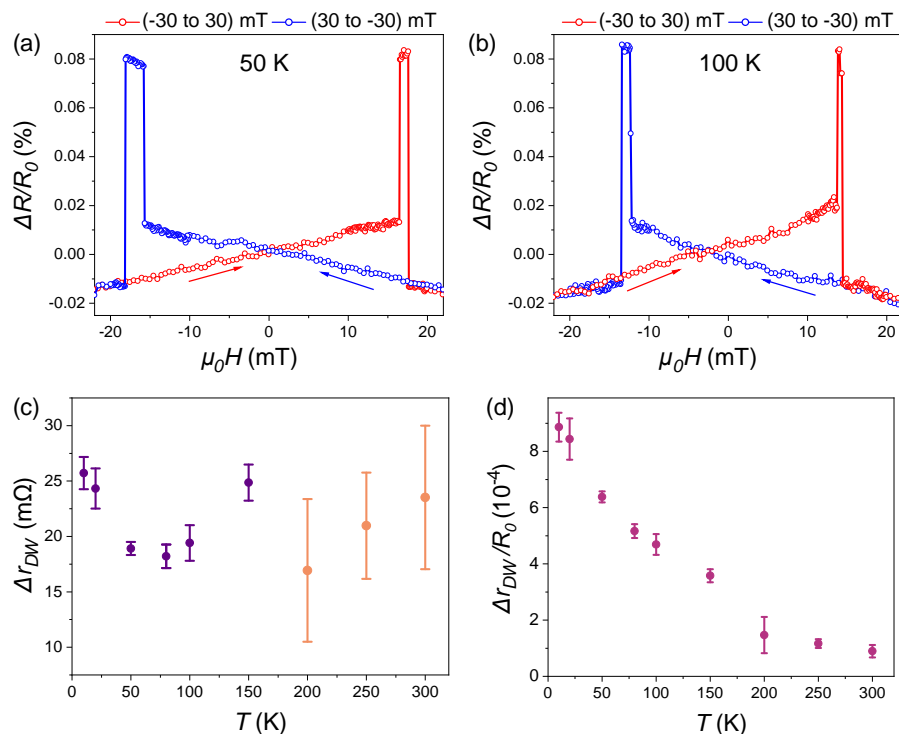
Figure 4.2: Two MR measurements on the same CrO$_2$ device as used in Fig. 4.1, with the magnetic field along [001] at (a) 50 K, where R$_0$ = 29.64 Ω and (b) 100 K, where R$_0$ = 41.32 Ω. The field was swept between 25 mT and −25 mT. The step size is 0.5 mT. The current used for both is 100 μA. (c) Resistance difference (Δr_{DW}) between the high-resistance and the low-resistance states as a function of temperature, showing a weak temperature dependence over the range from 10 K to 300 K. (d) Temperature dependence of ratio $\Delta r_{DW}/R_0$ indicates that as temperature increases $\Delta r_{DW}/R_0$ decreases. Multiple measurements were done for each temperature to calculate the error bars indicating the data fluctuations.

(where the width of the constriction is 50 nm), and they could measure Δr_{DW} and $\Delta r_{DW}/R_0$ (in our terminology). Their values for the DW resistance (DWR) are significantly smaller (around 4.5 mΩ), indicating a different wall structure, but they also find a decrease with increasing temperature until about 80 K. Then Δr_{DW} rises sharply and reaches values an order of magnitude higher than the value at low temperature. They argued that there are two competing temperature-dependent terms in play, spin-dependent scattering and spin disorder, both to be assessed in the DW. Following Levy and Zhang [17], and Viret [18], $\Delta r_{DW}/R_0$ for currents perpendicular to the wall depends on a factor $(\alpha - 1)^2/\alpha$, with $\alpha = \rho_0^\uparrow/\rho_0^\downarrow$, where $\rho_0^{\uparrow,\downarrow}$ are the spin-dependent resistances. When the minority spin channel is populated by e.g. spin excitations (magnons), α, and therefore the DWR, will decrease with increasing temperature. Furthermore, it stands to reason that spin disorder will
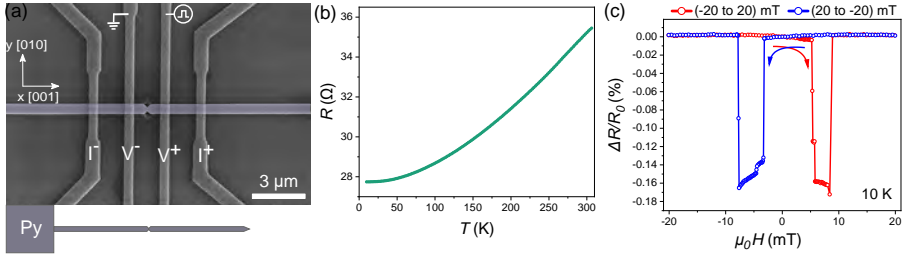
Figure 4.3: (a) SEM image of a Py device (Py wire shown in false color is along [001]) used in this study (see details in the text). The contacts leads are made of Cu. The four contact leads (I$^+$, I$^-$, V$^+$ and V$^-$) are used for the four-point resistance measurement. The center of the wire has a narrow constriction (a double notch) made by Focused Ion Beam milling. The bottom part of the image shows the full design of the Py wire where the contact pad is at the left end of the wire while the right end has a pointed edge termination. (b) Resistivity of the Py device as a function of temperature from 300K down to 10 K after the notch. (c) In-plane longitudinal magneto-resistance along [001] , measured at 10 K by sweeping the magnetic field between 20 mT and −20 mT. The step size is 0.5 mT. The current used in both resistivity and MR measurements is 100 μA.

increase with increasing temperature. That the spin disorder wins from the spin-dependent scattering above 80 K may be connected to the appearance of skyrmion-like topological defects in the magnetic state of CrO$_2$ [19, 20] that not only effect the bulk, but also the DW.

Py-Cu devices: We also made Py nanowires with Cu contacts using the fabrication steps described in detail in sec. 4.2.1. The Py nanowire (along [001]), as shown in fig. 4.3(a) has the following dimensions: width (w) = 500 nm, thickness (t) = 50 nm and the length (l) = 1.5 μm (between V$^+$ and V$^-$). The centre of the wire has a double notch where the width of the Py wire is 165 nm. We characterized the device by first measuring resistance as a function of temperature. As shown in Fig. 4.3(b), R(300 K) is 35.23 Ω while R(10 K) is 27.74 Ω. This gives a typical residual-resistivity ratio of 1.3 which is quite low compared to CrO$_2$. Since Py is a disordered alloy, this is to be expected.

We next measured the MR hysteresis loop by sweeping field along the $\pm$ x-axis of the wire between $\pm$ 20 mT. We followed the same protocol as for CrO$_2$ sample. As shown in Fig. 4.3(c), the resistance of the homogeneously magnetized state is now higher than the state in which a domain wall is trapped by the notches. Again this is a well known effect, caused by the fact that for these ^3d magnets, the resistance is lower when the current is perpendicular to the magnetization, which is the situation for the domain wall in the notch. We obtain the low resistance state in between 5.2 mT and 8.9 mT and from −7.9 mT to −3.3 mT.
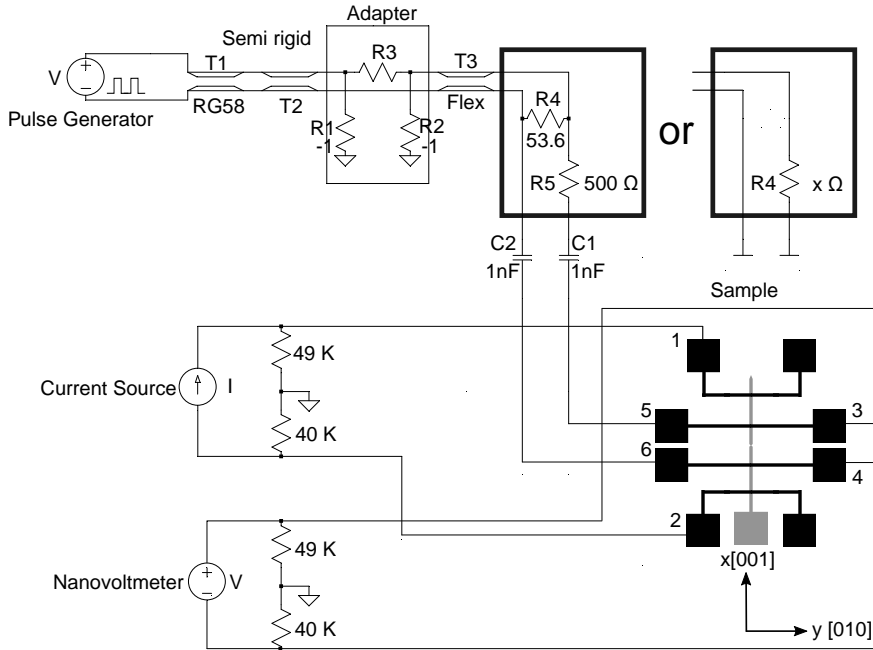
Figure 4.4: Schematic diagram illustrating the circuit design employed in the high frequency setup used for pulse injection. See detailed description in the text. The two rectangular boxes separated by "or" in between show the two different ways the current limiting resistances were designed. The left box depicts the configuration for the initial setup. The revised version, shown in the right box, incorporates a variable resistance (shown as "x" Ω) instead of R4 and R5, enables the injection of current by an order of magnitude larger as compared to the initial setup. In the circuit diagram following notations have been used. V: Voltmeter, RG: Radio Guide, R: Resistance, C: Capacitance. Crystal Orientation of the sample is also displayed. The easy axis of the Py/CrO_2 device shown in grey lies along [001] direction.

4.2.3. High frequency setup for pulse injection

We designed and developed a high frequency setup in-house that could be used to inject pulses to study current-induced domain wall motion. For this, the general purpose PPMS multi-functional probe insert (model 450A) was modified. Apart from the mechanical modifications made to accommodate the parts needed for sample holding, thermal anchoring etc., two semi rigid co-axial cables were introduced in the insert, which were connected to a pulse generator at one end and to the sample at the other end as shown in Fig. 4.4. The circuit was designed to achieve impedance matching as close as possible to 50 Ω. This design objective aims to minimize loss and maximize power and voltage of the pulse that is fed to the sample. We used an Instek AFG-3081 80 MHz Arbitrary Function Generator for pulse injection. The internal output resistance of 50 Ω of the pulse generator

was connected to contacts 5-6 of the sample, schematically shown in the Figure. For our measurements, we applied square pulses of the following parameters : frequency = 10 MHz, duty cycle = 20% while amplitude is varied. The two rectangular boxes separated by "or" in between show the two different ways the current limiting resistances were connected. The left box depicts the configuration for the initial setup. The revised design, shown in the right box, incorporates a variable resistance (shown as "x" Ω) instead of R4 and R5, hence allowing the injection of a current into the devices we used, that is an order of magnitude larger compared to the initial setup.

In order to determine the combinations of current and field that result in domain wall motion, the following experimental sequence was executed multiple times for each combination of field strength, current density of the pulse, and temperature:

(i) A full MR hysteresis loop was measured to get an idea about the switching fields for different states i.e. the single domain state or a DW pinned at the notch (as an example shown in Fig. 4.1(c)).

(ii) Then, a field driven DW motion experiment was performed to observe the critical pinning and depinning fields without injecting pulses (as an example shown in fig. 4.5)

(iii) Next, the pulse measurements were done similar to the last step: the DW is first pinned with the help of the field. Then the field was changed to a desired value where we wanted to depin the DW. Then square pulses of the desired amplitude, time-period and the pulse count were injected (as an example shown in fig. 4.6).

(iv) The resistance values were continuously measured, and if the resistance changed and returned to the value of the single domain state, it would be interpreted as the depinning of the DW from the notch. The experiment was repeated multiple times to check its reproducibility (as an example shown in fig. 4.7(b)).

(v) The field was changed and step (iii) and (iv) were repeated in order to determine the dependence of the (de)pinning critical current on an applied magnetic field ('field-assisted depinning').

Pulses were applied as voltage pulses. For the initial high frequency set up the current can be extracted as $I = V/(500 + R_s)$ where V is the amplitude of pulse and R_s is the device resistance. For the revised set up $I = V/(x + R_s)$ where "x" is the variable resistance added in series with device to make the total resistance as close
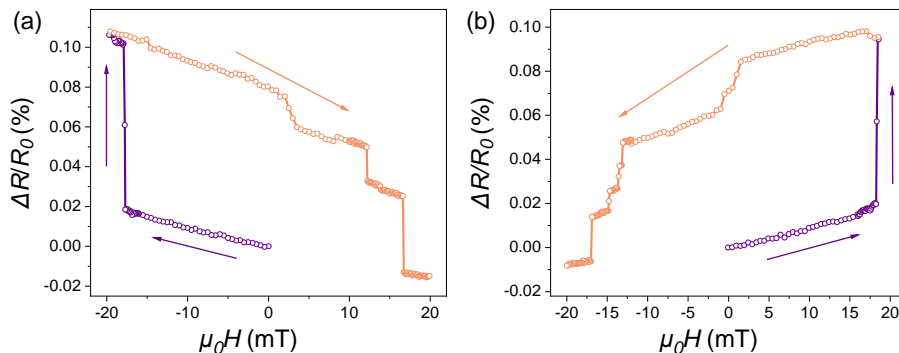
Figure 4.5: Field-driven DW motion. (a) The field is swept from 0 mT to −19.5 mT (the pinning field) where R jumps to the high resistance state (purple curve). Next, the field is swept back until the low resistance state (orange curve) is reached at 16.7 mT (the depinning field). (b) Same as in (a) but in the reversed direction. We find the pinning field at 18.5 mT and the depinning field at −17 mT.

as possible to 50 Ω. Using the size of the device, the critical depinning current density can be computed. Estimating the size of these voltage pulses at the position of the sample is difficult because of reflection and losses in the leads, so we made an estimate with a table-top experiment, which led to the conclusion that it is of the order of 22% of the amplitude of the applied voltage. We have taken this factor into account when computing the current density.

4.3. Investigating domain wall motion in CrO$_2$ nanowires

We used the same CrO$_2$ sample as shown in Fig. 4.1 (a) of w = 500 nm, t = 60 nm and l = 1.5 μm. The centre of the wire has a double notch where the width of the CrO$_2$ wire is 91 nm. The sample was connected to the high frequency setup which was initially designed in the left rectangular box configuration as shown in Fig. 4.4. We applied a constant d.c. current of 100 μA between contacts 1 and 2 and measured the voltage between the contact 3 and 4. The field was applied along the central CrO$_2$ nanowire axis (shown in grey in Fig. 4.4) which was along $\pm x$, which is also the easy magnetic axis of CrO$_2$. The temperature was set to 10 K.

4.3.1. Field-driven measurements on CrO$_2$

We measured the full MR hysteresis loop as shown in Fig. 4.1(b) during the characterization of the sample. Next, we investigated field driven DW motion as shown in Fig. 4.5(a,b). In Fig. 4.5(a), the field was first set to +500 mT to saturate the magnetization direction of both the wire and the contact pad along the positive
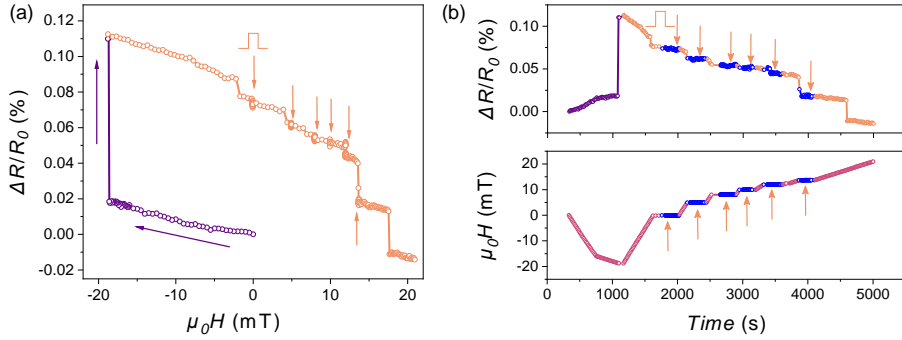
Figure 4.6: Current Induced DW motion. (a) The field is first swept from 0 mT to -19.5 mT to pin the DW (purple curve) and then the field is lowered to 0 mT to attempt depinning of the DW by applying pulses (orange curve) at magnetic fields indicated by the orange arrows. No depinning is observed until the depinning field is reached at 16.7 mT. (b) Upper panel: time dependent change in the MR when applying the pulses. The purple curve is prior to pinning, the pulse events are indicated by orange arrows, the data points taken during the pulse events are blue. Lower panel: the changes in applied field as function of time.

x-axis corresponding to low resistance state. We reduced the field to 0 mT and then increased it along the negative x-axis (the negative quadrant) until we saw the sharp increase in R that is the signature of catching a magnetic domain wall, at -19.5 mT. Next, we reversed the sweep direction until we reached the low resistance state again, corresponding to the depinning field of the DW at 16.7 mT. The same experiment was performed in the positive quadrant (see Fig. 4.5(b)). We observed small jumps in resistance before reaching the depinning field, which we attribute to changes in the spin texture of the magnetic domain wall in the notch. The variations are approximately the same in both experiments, as required by the symmetry of magnetic states under positive and negative magnetic fields along the x axis. The slight differences come from the asymmetry in the sample due to the notch and small irregularities along the edges of the wires.

4.3.2. Pulse measurements on CrO$_2$

Following the field-driven measurements, we applied the pulses. Again, the DW was pinned at the notch, following the procedure outlined above. Next, we changed the field back to 0 mT and injected pulses (frequency : 10 MHz, duty cycle : 20%, single pulse) at the fields indicated in Fig. 4.6 (a). The amplitude was increased in steps of 0.1 V starting from an initial value of 1 V (peak) until reaching a maximum value of 10 V corresponding to an estimated current of 18 mA and a critical current density of 7.5×10^{11} A/m^2. We did not see any change in the resistance, indicating that the DW was not depinned. Following that, we increased the field along + x-axis in steps
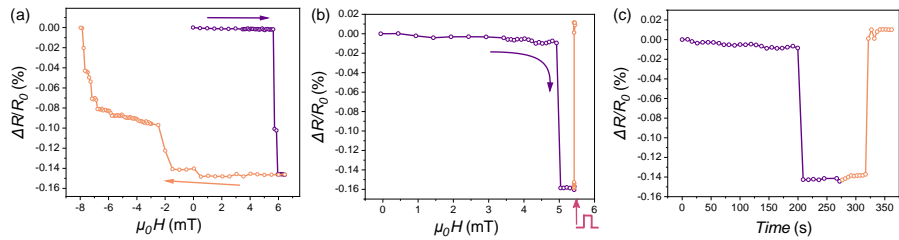
Figure 4.7: Current Induced DW motion in a Py sample. (a) The field is swept from 0 mT to 6 mT where pinning occurs (purple curve). Then the field is swept back to 0 mT and further increased until depinning occurs at −8 mT (orange curve). (b) The field is swept from 0 mT to 5 mT to pin the DW (purple curve). Then it is further increased to 5.5 mT and pulses are applied to depin the DW (orange curve). (c) Time dependent MR to show pinning and depinning events of the plot shown in (b).

(shown with orange arrow in Fig.4.6(a) to value of 5, 7.5, 10, 12.5) mT to 'field-assist' the depinning, since an increased field could help to reduce the critical current density required for depinning, and repeated the pulse injection and resistance measurement. Fig. 4.6 (b) top and bottom shows the moments in time (s) where the pulses were injected with arrows (orange) indicating clearly that the depinning did not occur when pulses were injected. Instead, the changes in resistances and finally depinning happened at the original and unchanged field value of ~ 17 mT.

We conducted the same measurement on additional CrO_2 devices with similar dimensions but featuring shallower notch width up to 150 nm. However, the results did not change. To understand this better, we next turned to similar measurements on Py devices.

4.4. DW motion in Py nanowires

Py samples have been studied extensively with respect to DW motion[4, 5, 21, 22]. We fabricated a Py-Cu device of the dimensions similar to CrO_2 device : w = 500 nm, t = 50 nm and l = 1.5 μm. The centre of the wire was milled using FIB to make a double notch where the width of the Py wire is ~ 101 nm. We first performed the field-driven DW motion experiments, as shown in Fig. 4.7a. The field was initially set to −500 mT to saturate the magnetization of the Py device. Then, we swept the field in opposite direction starting from 0 mT until we observed a sharp decrease in the resistance and a low resistance state corresponding to the pinning field of DW at 6 mT. Remember that for Py, the low resistance state means a domain wall is present in the notch. After that, we swept back the field along the negative x-axis until we got back the high resistance state corresponding to the depinning field of the DW at −8 mT.

Next, we conducted the pulse assisted DW depinning measurements. First, we pinned the DW at the notch with the help of the field following the steps as described above and shown in Fig. 4.7(a) and (b) in purple. In the next step (not shown), we reduced the field to 4 mT and injected the pulses (frequency: 10 MHz, duty cycle: 20%, single pulse). However, we did not see the resistance returning to the starting level, even at the maximum applied current, estimated to correspond to $1.9 \times 10^{11}\,\text{A/m}^2$. On the other hand, when we further *increased* the field from 5 mT (the pinning field) to 5.5 mT, we observed the resistance changed from low resistance state to high resistance state at the maximum applied current as shown in Fig. 4.7(b). Fig. 4.7(c) shows the plot of the time dependent change in MR. We see that when we started to apply the pulses of lower current on the device, the resistance stayed at the low level and only at maximum J_c, the resistance level jumped back to the starting level. This corresponds to the successful depinning of the DW from the notch.

The pulse measurements on Py-Cu demonstrated successful injection of pulses on our devices. However, we also recognized that higher currents were needed for further measurements. The setup's initial configuration imposes a limitation on the current that can be applied, primarily due to the presence of a series resistance of 500 Ω, which was incorporated into the initial design of the setup as a preventive measure, to safeguard the device against excessive heating caused by high current densities. To address this issue, we made adjustments to the setup by eliminating the series resistance R5 (500 Ω), as well as the parallel resistance R4 (53.6 Ω). These modifications are shown in Fig. 4.4. In the revised setup, the resistance of the sample is initially measured at 10 K. Based on the resistance value obtained, either a series or parallel resistor of desired value was added. This addition was necessary to achieve a total impedance of approximately 50 Ω, which is the desired value for optimal transmission. This enabled us to increase the current density by one order of magnitude.

4.5. DW motion in Py nanowires in the modified setup

After the modifications in the setup, we tested it with the Py-Cu devices. For this, we made similar Py nanowire device as shown in Fig. 4.3(a) of the following dimensions: w = 500 nm, t = 50 nm and l = 1.5 μm. The centre of the wire has a double notch where the width of the Py wire is 175 nm. After the standard characterization processes where we measured the resistivity and the MR hysteresis loop, we attempted the pulse measurements. First, we pinned the DW at the notch with the help of the field and then attempted to depin the DW by gradually increasing the current of

---

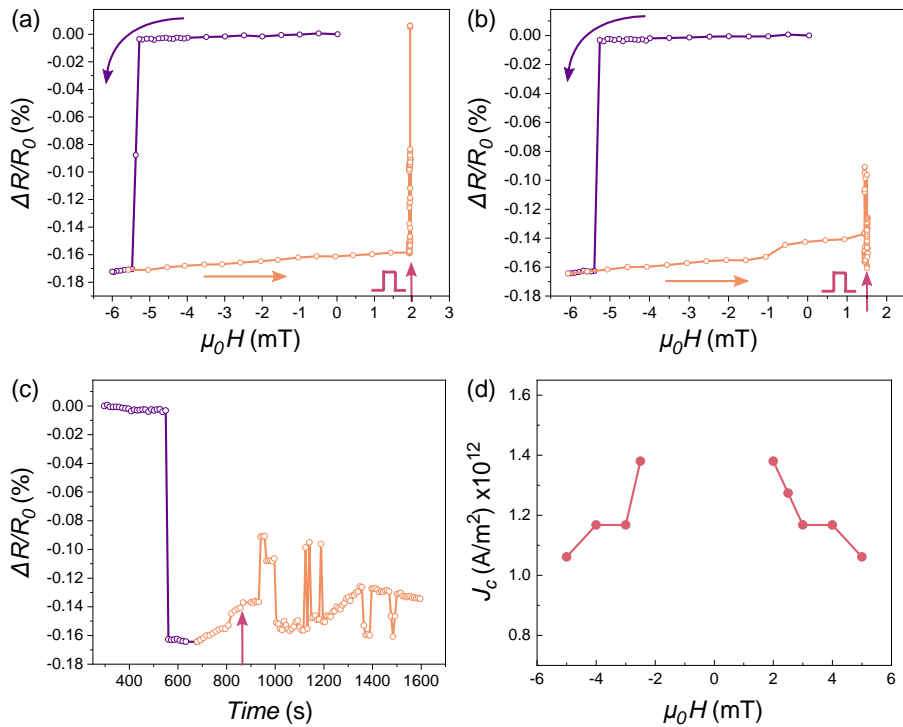All DW measurements were studied at 10 K in the modified setup

Figure 4.8: Pulse measurement on a Py sample in the modified setup. (a) Field is swept from 0 mT to −5.5 mT where pinning occurs (purple curve) and then field is reversed and swept back till 2 mT (orange curve) and pulse is applied (red arrow) to depin (orange curve). (b) Same as in (a) but now the pulse is applied at field of 1.5 mT. (c) Time dependent MR to show pinning and pulse events for the plot shown in (b). Arrow indicates point in time 1.5 mT was reached. (d) Critical current density as a function of field needed to depin shows that as the field is decreased towards 0 mT from either side the depinning current density increases.

the injected pulses. In Fig. 4.8(a) we show the successful depinning at 2 mT which was the lowest field where we could successfully depin the DW. Fig. 4.8(b,c) show the unsuccessful pulse-assisted depinning attempt at 1.5 mT. We measured the depinning current density at different fields as shown in Fig. 4.8(d), starting from ±5 mT and decreasing the field in steps of 1 mT At ±5 mT, we found that J_c was $1.06 \times 10^{12}\,\text{A/m}^2$ which increased to $1.38 \times 10^{12}\,\text{A/m}^2$ at ±2 mT. As expected, J_c started to increase as we approached 0 mT field from either direction.

We next made changes to the dimensions of the sample to further reduce the field needed to depin. We fabricated a Py device as shown in Fig. 4.9(a) with w = 253 nm, t = 40 nm and l = 1.5 μm. The centre of the wire has a single notch where the width of the Py wire is 150 nm. We performed the standard characterization
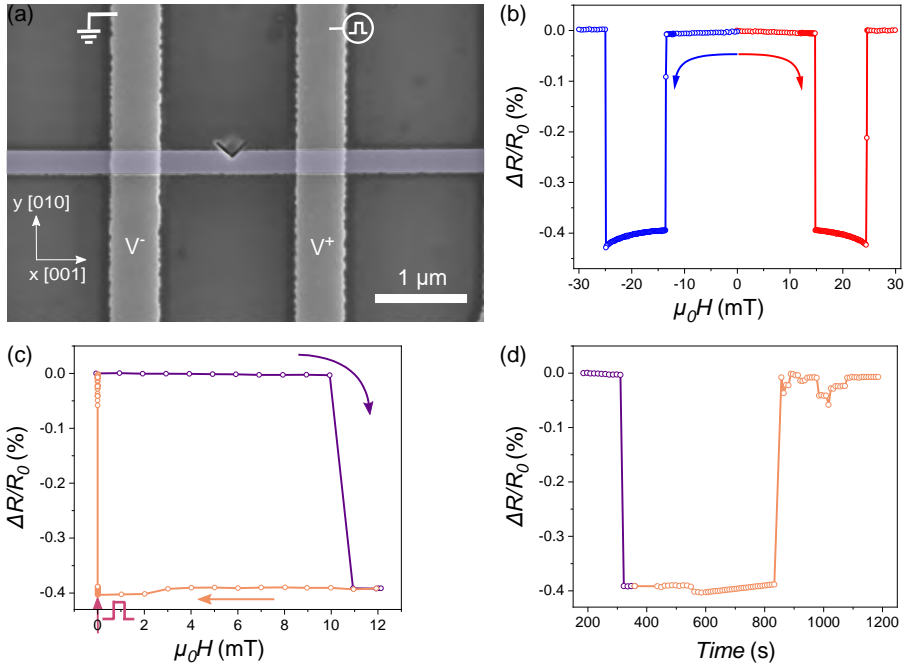
Figure 4.9: Pulse measurement on Py sample in modified setup. (a) SEM image of the Py device (the Py wire shown in false color is along [001]). The center of the wire has a single notch made with Focused Ion Beam milling. (b) In-plane longitudinal magnetoresistance along [001], measured at 10 K by sweeping the magnetic field from 0 mT to 30 mT (red curve) and 0 mT to −30 mT (blue curve). The step size is 0.5 mT. The current used for the MR measurement is 100 μA. (c) A pulse measurement. The field is swept from 0 mT to 12 mT where pinning occurs (purple curve). Then the direction is reversed and swept back to 0 mT. At that field, a pulse is applied (red arrow) to depin (orange curve). The critical depinning current density (J_c) is calculated to be 2.85×10^{12} A/m^2. (d) Time dependent MR to show pinning and depinning events for the plot shown in (c).

processes where we measured the resistivity and the MR hysteresis loop before attempting the pulse measurements. The decreased width and thickness of the wire results in higher pinning and depinning fields as seen in Fig. 4.9(b). We also observed that the change in resistance (Δr_{DW}) between single domain state and DW state has more than doubled.

Next, we attempted the pulse measurement on the sample by field assisted pinning of DW and then followed by pulse assisted depinning. As seen in Fig. 4.9(c), we were able to successfully depin at zero field by applying pulses corresponding to a current density J_c of 2.85×10^{12} A/m^2. This pulse assisted depinning at zero field for Py sample shows that setup is working and that we fixed the initial issues of too low current injection. After this, we moved back to CrO$_2$ devices to attempt the pulse measurements.

4.6. DW motion in CrO_2 nanowires in the modified setup

We fabricated a CrO_2 sample as shown in Fig. 4.10(a) with w = 625 nm, t = 80 nm and l = 4 μm. The centre of the wire has a double notch where the width of the CrO_2 wire is 475 nm. After initial resistivity measurements, we first performed a field driven DW motion without pulses to measure the depinning field of −5.3 mT, shown in Fig.4.10(b), and 5.1 mT, shown in Fig. 4.10(c). We also notice that the percentage change in MR has lowered from nearly 0.15 % as seen in Fig. 4.1 (c) for a neck width of 91 nm to approximately 0.02 % when the neck width is 475 nm. The depinning field has also decreased, from nearly ±17 mT as seen in Fig. 4.5 (a) and (b) to nearly ±5 mT.

Next, we attempted the pulse assisted depinning measurements on the sample. We observed successful depinning through pulse injection as shown in Fig. 4.10 (d,e) for fields above and including ±3 mT. However, we could not depin below 3 mT. Fig. 4.10(g) gives the plot of the depinning current density (J_c) as a function of the field. At ±6 mT, the value for J_c was 1.5×10^{11} A/m^2, which increased by a factor 6 to 9.7×10^{11} A/m^2 when field was reduced to 3 mT. We observed a small asymmetry in J_c, which may be attributed to the intrinsic asymmetry of the device. Furthermore, it is evident, as expected, that the size of the notch makes an impact to J_c. While a deep notch assists in obtaining a strong MR signal, it also leads to strong pinning potential for both Py and CrO_2 samples which makes depinning challenging. Conversely, a shallow notch makes the DW's pinning weaker, but it facilitates depinning during pulse measurements.

Finally, similar to the Py samples, we attempted to make a single notch on the CrO_2 wire as shown in Fig. 4.11(a) of similar width of 625 nm and thickness of 91 nm. The wire width at the notch is around 450 nm. The MR hysteresis loop displayed in Fig. 4.11(b) shows similar behavior as the previous sample with double notch (see Fig. 4.10(b,c)) with a MR change of around 0.025%. For this sample, we could depin using pulses until 5 mT. J_c was calculated to be 6.8×10^{11} A/m^2 which is about 2.5 times higher than 2.5×10^{11} A/m^2 measured for the previous sample. This indicates, not surprisingly, that the CrO_2 devices are very sensitive to variations in the width of the notch and probably also the shape of the notch. The depinning current density reveals a sharp rise even in response to minor variations in the devices. As seen in Fig. 4.11(c), we could not depin at field of 4 mT and below while in the last device it was possible to depin up to 3 mT.

Another significant point is that we used evaporation and liftoff methods to deposit Py-Cu samples in order to fabricate the devices. This provided us with the ability to control the thickness of the nanowires. However, in the case of CrO_2, we used Chemical Vapor Deposition technique to grow CrO_2. This makes achieving

Figure 4.10: Pulse measurement on a CrO$_2$ sample in the modified setup. (a) SEM image of the CrO$_2$ device (see details in the text). The length of the wire is along [001]. The center of the wire has a small double notch made with FIB milling. (b) The field is swept from 0 mT to 5 mT where we see the change in resistance (from low to high resistance) corresponding to DW pinning (purple curve). Then the field is swept back until we obtain the low resistance state (orange curve) corresponding to the depinning field at −5.3 mT. (c)Same as in (b) but in the reversed direction. We find the pinning field at −5.5 mT and the depinning field at 5.1 mT. (d), (e), (f), (g) The field is swept from 0 mT to 5.3 mT where pinning occurs (purple curve) and then swept back until 5 mT, 4 mT, 3 mT and 2.5 mT (orange curve) respectively. At these fields, pulses are applied (red arrow) to depin (orange curve). (h) Critical current density as a function of field needed to depin. As the field is decreased towards 0 mT from either side the depinning current density increases. There was no depinning found between −2.5 mT and 2.5 mT.
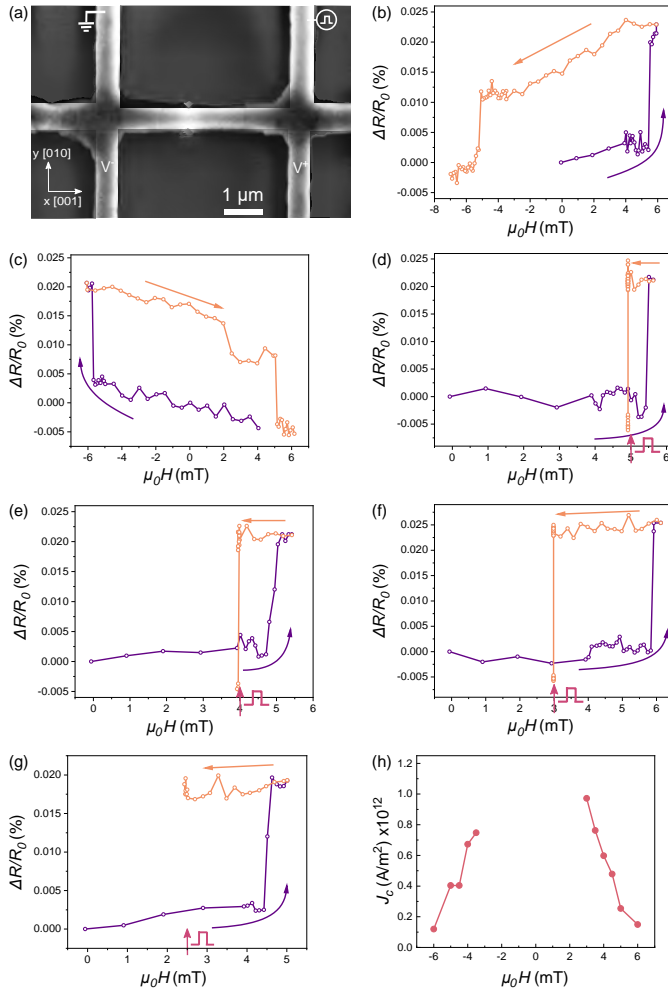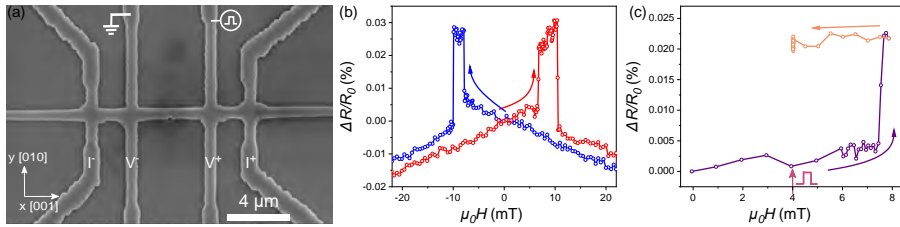
Figure 4.11: Pulse measurement on a CrO$_2$ sample in the modified setup. (a) SEM image of the CrO$_2$ device (see details in the text). The length of the wire is along [001]. The center of the wire has a small single notch made with FIB milling. (b) In-plane longitudinal magnetoresistance along [001], measured at 10 K by sweeping the magnetic field between +30 mT and −30 mT. The step size is 0.5 mT. The current used in the MR measurement is 100 μA. (c) The field is swept from 0 mT to 7.5 mT where pinning occurs (purple curve). Then field is reversed and swept back until 4 mT (orange curve) and a pulse is applied (red arrow) to attempt depinning (orange curve).

precise control over the thickness of the nanowires more challenging. Hence, it was not easy to grow thin nanowires in the range of 10 − 40 nm which has been used in previous studies on other ferromagnets [4, 5, 22]. In order to address this issue, attempts were made to remove the top layer of CrO$_2$ devices using an Argon (Ar) etcher. However, that resulted in no pinning of DW (see Appendix Fig. 4.13). This lack of pinning may likely be attributed to the surface being damaged during the etching process and the introduction of contaminants from the use of Ar ions. Another experimental approach that we would have been interested in pursuing, but were unable to, owing to challenges in growth and fabrication process, included reducing the width of the CrO$_2$ wire. This was motivated by our findings indicating that decreasing wire width had a positive effect on depinning in the instance of Py.

An important factor that merits consideration is Joule heating. The injection of pulses results in high currents and current densities due to small dimensions of our devices, and heating is a well-known issue in the study of current-induced domain wall motion, mostly performed on Py. When similar measurements are performed at room temperature, the observed effect becomes more significant since the temperature may approach the Curie temperature (T_C). In certain cases, when these measurements are conducted at room temperature the effect may even exceed T_C[7, 22]. However, when the measurements were conducted at low temperatures, the effect is diminished. Laufenberg et. al.[22], working with Py rings, showed that below 20 K the sample heats up by $\Delta T \approx 100$ K at a current density of 2.1×10^{12} A/m^2 when applying pulses. Biehler et al. observed similar results below 50 K on CrO$_2$ wires etched out of films [8]. In our case, we conducted all the pulse measurements at 10 K. This most likely suggests that while the actual sample temperature of the sample may well be significantly higher than 10 K, it will still remain significantly lower than the T_C of about 650 K for Py and 390 K for CrO$_2$.

4.7. Conclusion

In summary, we have built and developed a high frequency setup to study current driven domain wall motion. The setup allows to inject current pulses to assist in depinning of DW. The setup was tested on Py samples and the critical fields and critical current densities necessary to move a domain wall in Py nanowires were measured. The pulse measurements on different widths and thickness of Py nanowires show that, the depinning is easier on a narrow and shallow notched wire (< 30%) as compared to wider wires and deep notch.

In CrO$_2$ nanowires, the temperature dependence of MR effects was studied. We observed that Δr_D initially decreased between 10 and 80 K and above 80 K, started to increase, although the trend was not clear above 150 K due to difficulty in measuring a clear and sharp MR signal. CrO$_2$ samples also show that it is possible to move a DW using pulses. However, depinning current density increases sharply with decreasing magnetic field as compared to Py devices where the rise in current density is gradual. Furthermore, CrO$_2$ devices are more sensitive to the width of the notch and slight variations can bring about a large change in depinning current density. The magnitude of critical current densities are comparable to that of Py samples and high spin polarization does not reduce the current densities. The main difficulty with CrO$_2$ remains it's extremely difficult and sensitive fabrication process which makes it hard to systematically study to make fast progress with the measurements.

4.8. Appendix

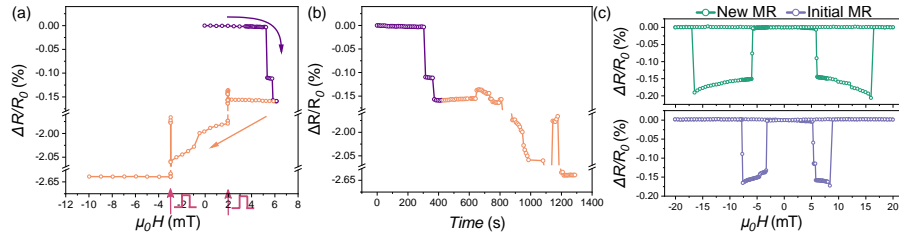### 4.8.1. Pulse measurement on a Py-Cu device with a deep notch in the modified setup

Figure 4.12: Pulse measurement on a Py-Cu device in the modified high frequency setup. (a) The field is swept from 0 mT to 5.5 mT where pinning occurs (purple curve). Then the field is swept back until 2 mT (orange curve) and pulses are applied (red arrow) to attempt depinning. The resistance decreases sharply on applying the pulse, indicating damage to the device. Afterwards, the field was further swept to −3 mT and pulses were again injected. The resistance dropped again. (b) The time dependent MR plot of (a) shows the drop in resistance when pulses are applied. (c) Comparison between the MR plots before injecting any pulses to the device (blue curve) and after injecting pulses (green curve) in the same device. The depinning of the DW with pulses does not work anymore at any field including 5 mT.

A Py-Cu device of the following dimensions: w = 500 nm, t = 50 nm, l = 1.5 μm and notch width = 165 nm was measured in the modified high frequency setup. The pulse assisted depinning worked normally above 2 mT. However, at 2 mT and below, the depinning did not work. When the pulses were injected, we observed a sharp drop in resistance instead of the resistance going up as usual. The corresponding current density was 5.4×10^{12} A/m^2. This change of resistance was permanent and probably came from damage to the device due to the high current. After several failed attempts with the pulse measurement at different fields, where we observed similar sharp drop in resistance, we measured the MR hysteresis loop of the sample again. As seen in Fig. 4.12(c), we find that the behavior has changed from the last measurement. The low resistance state window in new MR has become very wide compared to the initial MR. Also, now the depinning of DW with pulses does not work anymore at any field including 5 mT, suggesting damage to the sample from the high current. To better understand the damage caused to the device, we would need further investigation.
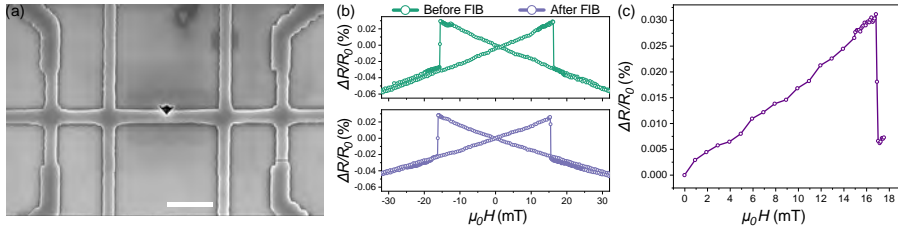
4.8.2. Measurements on an Ar etched CrO$_2$ device with a single notch

Figure 4.13: (a) SEM image of a CrO$_2$ device width w = 431 nm, t = 82 nm, l = 4 μm and notch width = 355 nm after FIB. (b) Comparison between the MR plots following a 2-minute argon (Ar) etching process on a CrO$_2$ device both before FIB (green curve) and after making a notch with FIB (blue curve) shows almost no change in MR plot. (c) Failed attempt to pin the DW using field. Instead we see an instantaneous change in magnetization direction from negative x-axis to positive x-axis.

In the preceding sections, we observed in Py-Cu devices that a decrease in the thickness of the Py wire allowed for the depinning of DW to occur at lower fields with the pulse injection. We attempted to replicate the same with CrO$_2$ wire. Due to the challenges encountered in achieving the desired thin wire growth using CVD compared to the evaporation for Py wires, we Ar-etched the CVD grown wire of dimensions width w = 431 nm, t = 82 nm and l = 4 μm, for 2-min to thin it down. Following the Ar-etch, t was measured to be around 75 nm. Fig. 4.13(b) shows the MR plot (green curve) of the wire after Ar-etching. Since, the MR doesn't show pinning of a DW, we made a notch using FIB similar to other devices. Fig. 4.13(a) gives the SEM image of the wire with a single notch after FIB milling. Next, we measured the MR again and found the plot (blue curve) to be of same nature as for the wire before FIB. This observation suggests that notch didn't help with pinning the DW, which typically appears as a high resistance state within a narrow range of applied magnetic field before transitioning to a low resistance state, as we had found for earlier devices which were not etched. One of the plausible reason could be that Ar-etching leads to damage to the surface of CrO$_2$ wire which affects the pinning site. Fig. 4.13(c) gives one of the failed attempts to pin the DW on this wire. Instead of a high resistance state, we observed an instantaneous change in magnetization direction from - x-axis to + x-axis.

4.8.3. Pulse measurement on a CrO_2 device at 80 K and 100 K
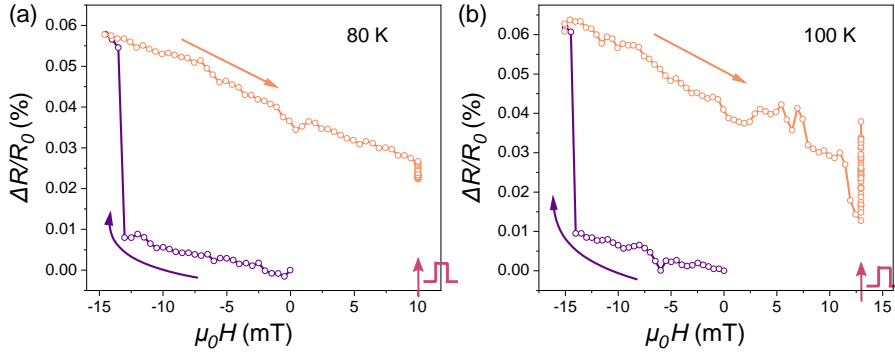
Figure 4.14: Pulse measurement on CrO_2 device at 80 K and 100 K. (a) Pulse measurement at 80 K. Field is swept from 0 mT to -14.5 mT where pinning occurs (purple curve) and then field is reversed and swept back till 10 mT (orange curve) and pulse is applied (red arrow) to attempt depin (orange curve). (b) Pulse measurement at 100 K. Field is swept from 0 mT to -15 mT where pinning occurs (purple curve) and then field is reversed and swept back till 13 mT (orange curve) and pulse is applied (red arrow) to attempt depin (orange curve). In both cases, the depinning didn't occur.

As discussed before in sec.4.3, pulse measurements were attempted on a CrO_2 device (see Fig. 4.1 (a) of w = 500 nm, t = 60 nm and l = 1.5 μm, with a central double notch of width around 91 nm) at 10 K in the intial high frequency set up. After, the failed attempts of depinning DW at 10 K, we also attempted the pulse measurements at higher temperatures of 80 K and 100 K. As shown in Fig. 4.14 (a) and (b), depinning was not observed for either temperature.

References

[1] Allwood, D. A. et al. Magnetic domain-wall logic. Science **309**, 1688–1692 (2005).

[2] Parkin, S. S. P., Hayashi, M. & Thomas, L. Magnetic domain-wall racetrack memory. Science **320**, 190–194 (2008). URL https://www.science.org/doi/abs/10.1126/science.1145799. https://www.science.org/doi/pdf/10.1126/science.1145799.

[3] Berger, L. Emission of spin waves by a magnetic multilayer traversed by a current. Phys. Rev. B **54**, 9353–9358 (1996). URL https://link.aps.org/doi/10.1103/PhysRevB.54.9353.

[4] Yamaguchi, A. et al. Real-space observation of Current-Driven Domain Wall Motion in Submicron Magnetic Wires. Phys. Rev. Lett. **92**, 077205 (2004). URL https://link.aps.org/doi/10.1103/PhysRevLett.92.077205.

[5] Kläui, M. et al. Controlled and reproducible domain wall displacement by current pulses injected into ferromagnetic ring structures. Phys. Rev. Lett. **94**, 106601 (2005). URL https://link.aps.org/doi/10.1103/PhysRevLett.94.106601.

[6] Hayashi, M. et al. Dependence of current and field driven depinning of domain walls on their structure and chirality in permalloy nanowires. Phys. Rev. Lett. **97**, 207205 (2006). URL https://link.aps.org/doi/10.1103/PhysRevLett.97.207205.

[7] Yamaguchi, A. et al. Effect of joule heating in current-driven domain wall motion. Appl. Phys. Lett. **86**, 046602 (2004). URL https://aip.scitation.org/doi/10.1063/1.1847714.

[8] Biehler, A. et al. Domain structures and the influence of current on domains and domain walls in highly spin-polarized Cro_2 wire elements. Phys. Rev. B **75**, 184427 (2007). URL https://link.aps.org/doi/10.1103/PhysRevB.75.184427.

[9] Laufenberg, M. Interactions Between Current and Domain Wall Spin Structures. Ph.D. thesis, Universität Konstanz, Germany (2006).

[10] König, C. Nanomagnetismus von epitaktischen Fe (110)-und CrO_2 (100)-Strukturen im Hinblick auf potentielle spinelektronische Anwendungen. Ph.D. thesis, Aachen, Techn. Hochsch., Diss., 2006, Germany (2006).

[11] Chen, W., Qian, L. & Xiao, G. Resistance of domain-wall states in half-metallic CrO_2. Phys. Rev. B **98**, 174402 (2018). URL https://doi.org/10.1103/PhysRevB.98.174402.

[12] Chiba, D. et al. Control of multiple magnetic domain walls by current in a co/ni nano-wire. Applied Physics Express **3**, 073004 (2010). URL https://dx.doi.org/10.1143/APEX.3.073004.

[13] Koyama, T. et al. Observation of the intrinsic pinning of a magnetic domain wall in a ferromagnetic nanowire. Nature Materials **10**, 194–197 (2011). URL https://doi.org/10.1038/nmat2961.

[14] Yao, J. Spin Transport and Superconductivity in Half-metallic Nanowires and Junctions. Ph.D. thesis, Leiden University (2023).

[15] Kent, A. D., Yu, J., Rüdiger, U. & Parkin, S. S. Domain wall resistivity in epitaxial thin film microstructures. Journal of Physics: Condensed Matter **13**, R461 (2001).

[16] Zou, X. Magnetic Domain Configurations and Huge Wall Resistivity in Half-metallic Chromium Dioxide (CrO_2) Nanostructures. Ph.D. thesis, Brown University, Providence, Rhode Island, 5 (2010).

[17] Levi, P. & Zhang, S. Resistivity due to domain wall scattering. Phys. Rev. Lett. **79**, 5110 (1997). URL https://doi.org/10.1103/PhysRevLett.79.5110.

[18] Viret, M. et al. Spin scattering in ferromagnetic thin films. Phys. Rev. B **53**, 8464 (1996). URL https://doi.org/10.1103/PhysRevB.53.8464.

[19] Ye, J. et al. Berry phase theory of the anomalous hall effect: Application to colossal magnetoresistance manganites. Phys. Rev. Lett. **83**, 3737 (1999). URL https://doi.org/10.1103/PhysRevLett.83.3737.

[20] Yanagihara, H. & Salamon, M. B. Skyrmion strings and the anomalous hall effect in CrO_2. Phys. Rev. Lett. **89**, 187201 (2002). URL https://doi.org/10.1103/PhysRevLett.89.187201.

[21] Vernier, N., Allwood, D. A., Atkinson, D., Cooke, M. D. & Cowburn, R. P. Domain wall propagation in magnetic nanowires by spin-polarized current injection. Europhysics Letters **65**, 526 (2004). URL https://dx.doi.org/10.1209/epl/i2003-10112-5.

[22] Laufenberg, M. et al. Temperature dependence of the spin torque effect in current-induced domain wall motion. Phys. Rev. Lett. **97**, 046602 (2006). URL https://link.aps.org/doi/10.1103/PhysRevLett.97.046602.

5

Fabrication and Properties of Lateral Josephson Junctions with a RuO$_2$ Weak Link

Ruthenium dioxide (RuO$_2$) is a metallic rutile oxide with a number of interesting properties. For a long time, it was considered to be a highly conductive normal metal and a Pauli paramagnet. Recently, it was found that the material is antiferromagnetic, with small magnetic moments of the order of 0.05 Bohr magneton and an ordering temperature above 300 K. The presence of magnetic moments should have clear consequences when trying to induce superconductivity in RuO$_2$. We used a selective area chemical vapor deposition method to grow nanowires of RuO$_2$ on TiO$_2$ substrates. On these wires, superconducting contacts were made of MoGe, and a weak link was fabricated with a Focused Ion Beam. We find that the device behaves as a Josephson junction, including a Fraunhofer-like response to a magnetic field, for distances between the contacts below 70 nm. We estimate the induced singlet coherence length ξ to be about 12 nm, which seems a reasonable number when small magnetic moments are present.

5.1. Introduction

In recent years, there has been a revival of interest in the properties of the metallic rutile oxides CrO_2, RuO_2 and IrO_2, mainly in connection with magnetism, non-trivial Fermi surfaces, and possible spintronics applications [1, 2]. CrO_2 is a half-metallic ferromagnet that in bulk form was long used in magnetic tapes [3] and in thin film form was found of particular interest to study superconducting long rang range proximity effects [4–6]. IrO_2 was researched from a spintronics perspective as a material with large spin-orbit coupling [7, 8]. RuO_2 was long thought to be a normal metal, and in film form often used in low-temperature thermometry, because of ease of use and insensitivity of the resistance to even high magnetic fields. However, in 2017 itinerant antiferromagnetism was discovered [9], with magnetic moments of the order of 0.05 μ_B (with μ_B the Bohr magneton) and a (Néel) ordering temperature above 300 K. This was confirmed in another study [10], and also prompted renewed studies of the anomalous Hall effect [11, 12]. On the other hand, also superconductivity was recently reported in slightly strained films of RuO_2 [13].

Long range proximity effect has been recently observed in Mn_3Ge, resulting from the chiral non-collinear antiferromagnetic spin structure that creates a non-zero Berry phase [14]. The same study also reported that IrMn, a collinear antiferromagnet with moments on the Mn site of the order of 3 μ_B (Bohr magneton) [15], only shows short range supercurrents owing to its trivial topological spin arrangement. RuO_2, although also a collinear antiferromagnet, has been shown to have crystal inversion asymmetry arising from spin-splitting and time-reversal symmetry breaking in the band structure [16–18]. RuO_2 has also been identified as a promising candidate to allow for spin polarized currents which has been substantiated by recent transport measurements conducted on RuO_2 [19–21]. In this work, we investigate the proximity effect in RuO_2 nanowires by fabricating lateral Josephson junctions, using superconducting amorphous MoGe as electrodes. Since the resistivity of RuO_2 is quite low, we can expect a quite long induced coherence length if the material behaves as a normal metal. Instead, and confirming the presence of (small) magnetic moments, we find a short decay length (ξ) of around 12 nm which indicates the presence of only short range singlet Cooper pairs and absence of long range spin triplets. The chapter is organized in the following manner. We begin by examining the nanofabrication process that leads to Selective Area (SA)-grown nanowires. Subsequently, we proceed to characterize these RuO_2 nanowires through electrical and magneto-transport measurements. Then we focus on making Josephson junctions (JJ) in which superconducting MoGe are contacted on top of RuO_2 nanowires with varying lateral gaps and present the results on these junctions.

5.2. Selective area growth of RuO$_2$ nanowires

We grow RuO$_2$ nanowires on (100) oriented TiO$_2$ substrates using the same selective area growth technique as CrO$_2$ nanowires [22] since the lattice parameters of TiO$_2$, RuO$_2$ and CrO$_2$ are comparable and they all crystallize with a rutile structure and a tetragonal unit cell. RuO$_2$ has the attice parameters a = b = 0.4499 nm and c = 0.3107 nm while TiO$_2$ has the values of a = b = 0.4594 nm and c = 0.2958 nm. Compared to the TiO$_2$ lattice, the [010] and [001] directions of bulk RuO$_2$ have a lattice mismatch of approximately -2.1 % and +5.0 % respectively. Thus, RuO$_2$ thin films experience tensile strain along [010] while compressive strain along [001].

The fabrication of the RuO$_2$ nanowire starts with an HF etch of TiO$_2$ substrate. This is then followed by depositing a SiO$_x$ layer, which in our case has a thickness of approximately 25 nm, and electron beam patterning to create a positive resist mask with the desired device structure. Subsequently, the trench is selectively etched using reactive ion etching (RIE). We have observed that both underetching and overetching the trench is detrimental for a successful growth, similar to the case of CrO$_2$. RuO$_2$ nanowires are subsequently grown in the trenches using Chemical Vapor Deposition (CVD) in a two-zone furnace. During this process, the substrate temperature is maintained at 390°C while the precursor (C$_5$H$_5$)$_2$Ru is heated to 80°C in the presence of an O$_2$ carrier gas flow. Fig. 5.1(a) shows the SEM image of an epitaxially grown RuO$_2$ nanowire along the [001] direction. RuO$_2$ also grows on the surface of SiO$_x$[23] albeit much more slowly than on TiO$_2$ which helps to prevent merging of small crystals of RuO$_2$ of a few tens of nanometers in diameter that also form during nanowire growth.

Fig. 5.1(b) shows the temperature dependence of the resistivity, ρ_{xx}(T) of a typical RuO$_2$ nanowire, that was patterned as a Hall Bar of width around 650 nm, thickness around 100 nm and with a distance between the contacts around 2.6 μm. The 300 K resistivity ρ_{300} is 71 $\mu\Omega$.cm while the low-temperature (10 K) specific resistance ρ_{10} is 13.5 $\mu\Omega$.cm. This gives a residual-resistivity ratio (RRR, the ratio between ρ_{300} and ρ_{10}) of around 5.3. The wire has positive temperature coefficient of resistance at all temperatures including at low temperatures, as seen in inset of Fig. 5.1(b), which suggests very little or no grain boundary scattering of electron and a high crystal quality of the RuO$_2$ nanowires.

We further characterized RuO$_2$ wires through Hall measurements at different temperatures. Fig. 5.1(d) shows measurements of the Hall resistivity as a function of an out-of-plane magnetic field for different temperatures in a range from 300 K to 10 K. The data are represented as ρ_{xy} as function of magnetic field, with $\rho_{xy} = \frac{V_{xy}t}{I}$. Here, V$_{xy}$ is the transverse voltage, I is the measurement current, and t is the thickness of the wire. $\rho_{xy}(\mu_0 H)$ is linear for all the measured temperatures and
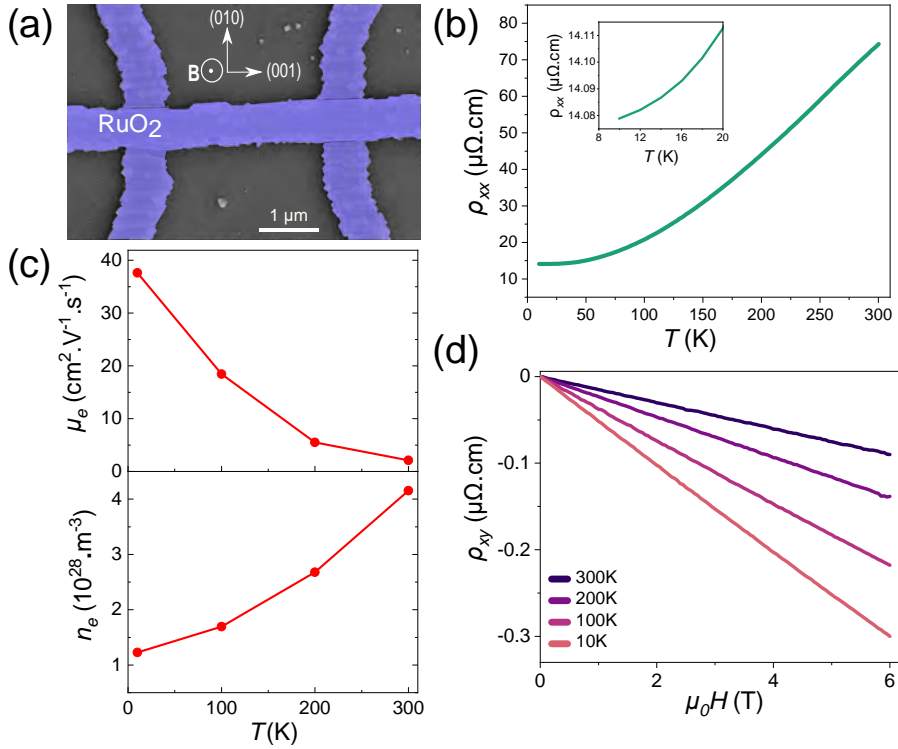
Figure 5.1: (a) SEM image (false color) of a RuO$_2$ nanowire grown using Selective Area Growth. The magnetic field B is applied out of the plane for Hall characterization measurements. (b) Longitudinal resistivity as a function of temperature for a RuO$_2$ nanowire with dimensions of approximately 2.6 μm in length between contacts and 650 nm in width; inset shows the positive temperature coefficient of resistance at lower temperature indicating that high crystal quality. (c) mobility (μ_e) (top) and charge carrier density (n_e) (bottom) at different temperature indicating that the behavior is unlike normal metal where n_e stays constant with temperature (d) Hall resistivity as a function of applied field measured at various temperature between 10 K to 300 K.

the field with a slope that corresponds to electron-like charge carriers. Carrier density (n) and mobility (μ_e) follow in a one-band model from $\rho_{xy} = -\frac{\mu_0 H}{e \cdot n}$ and $\mu_e = \frac{\sigma_{xx}}{e \cdot n}$ where, σ_{xx} is $1/\rho_{xx}$. Their values and temperature dependence are plotted in Fig. 5.1c. It is interesting to note that charge carrier density decreases with temperature and is nearly 4 times lower at 10 K than at 300 K.

5.3. Methods

Junction fabrication: To fabricate the lateral JJs (Fig. 2a), the initial step involved using SA technique to grow RuO$_2$ nanowires with dimensions of approximately
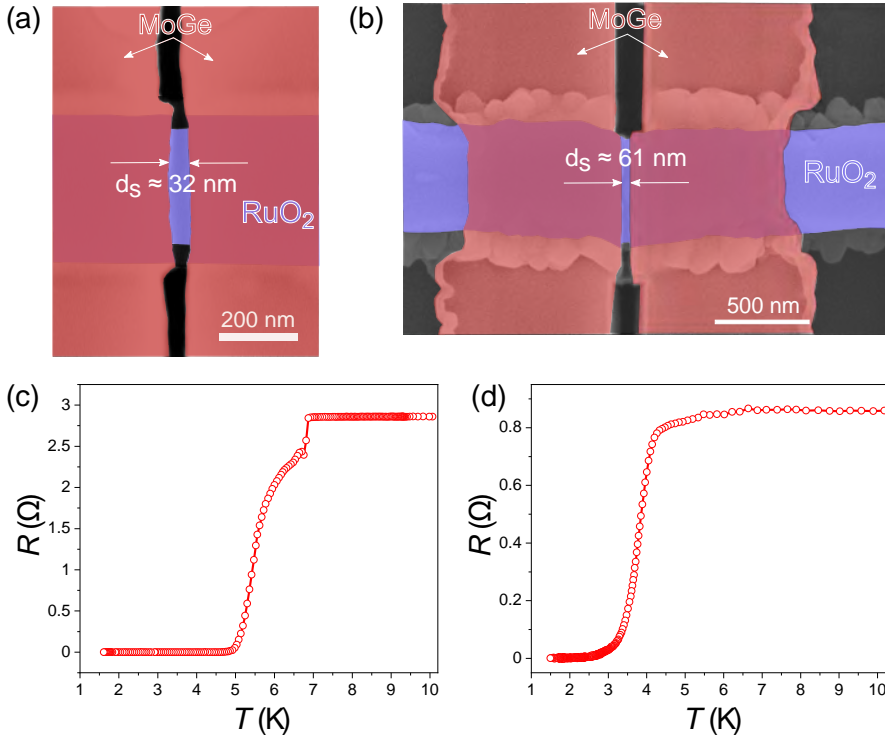
Figure 5.2: SEM image (false color) of the fabricated Josephson junctions (JJ) comprising RuO$_2$ nanowire (in blue) and MoGe as the superconducting contacts (in peach) that are laterally edge to edge separated by (a) 32 nm for J1 and (b) 61 nm for J2. (c), (d) Resistance vs temperature plot between (10 to 1.5) K showing the transition temperature (T_c) for the junctions (c) J1 and (d) J2. We have taken T_c as the temperature at which the resistance has decreased to 50% of the normal resistance value, which for J1 is 5.5 K and for J2 is 3.8 K.

30 μm in length and 250 nm in width, along the [001] direction. The contacts were subsequently patterned on top of the RuO$_2$ nanowire using e-beam lithography. 100 nm of MoGe sputter deposited at a pressure of 5×10^{-3} mbar, which was followed by a lift-off process. Finally, the weak link was created using Focused Ion Beam (FIB) etching. In this way, three different junction devices were fabricated, with an edge-to-edge gap between the MoGe contacts of 32 nm (J1), 61 nm (J2) and 105 nm (J3). Here, a caveat is needed. In particular the 32 nm trench is both hard to make uniform, and proved not easy to measure in the SEM. The estimate should rather be 27 nm - 38 nm. Moreover, the cut for this sample also made the wire locally smaller. For the wider bridges, fewer issues were experienced. Also, generally, the cuts were quite deep, meaning that the RuO$_2$ bridge was thinner than it nominal value. Still, some clear conclusions can be drawn, as we will discuss below.
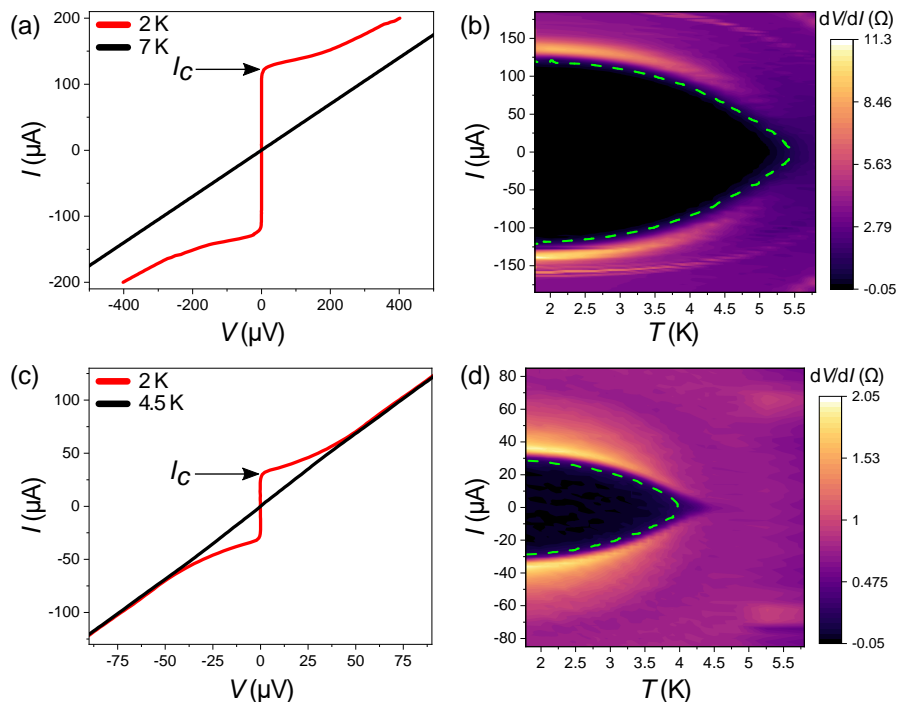
Figure 5.3: (a) and (c) I-V measurements taken above (black) and below (red) superconducting transition of J1 and J2 devices respectively. (b) and (d) shows I-dV/dI plot measured over different temperatures in steps of (b) 200 mK and (d) 100 mK. The dotted green line is the associated critical current I_c as a function of temperature T at dV/dI of 0.42 for both J1 and J2.

Device	T (K)	I_c (μA)	R_n (Ω)	d_s (nm)	V_c (μV)
J1 (E5-2.1)	1.8	121	2.85	32 ±6	345
J2 (H4-1.1)	1.8	29.3	0.86	61	25.2
J3 (E5-1.2)	1.5	0	3.11	105	0

Table 5.1: Critical current at measured temperature, normal resistance, junction length and the corresponding critical voltage of three Josephson junction devices based on RuO_2 nanowires.

Fig. 5.2(a), (b) shows the SEM images (false color) of the devices J1 and J2 respectively, consisting of RuO_2 nanowire (blue) and MoGe electrodes (peach) on top of RuO_2. Fig. 5.2(c), (d) give their corresponding resistive transitions. The critical temperature of the MoGe is about 7 K, and visible as a tiny step (in J1), or a deviation from constant resistance (J2). A clear drop in resistance due to the contacts going superconducting is not expected, since this is a 4-point measurement. The normal state resistance in both cases (about 3 Ω for J1, 0.8 Ω for J2) is quite different, mainly due to the difference in trench depth. The transition temperature T_c, defined by
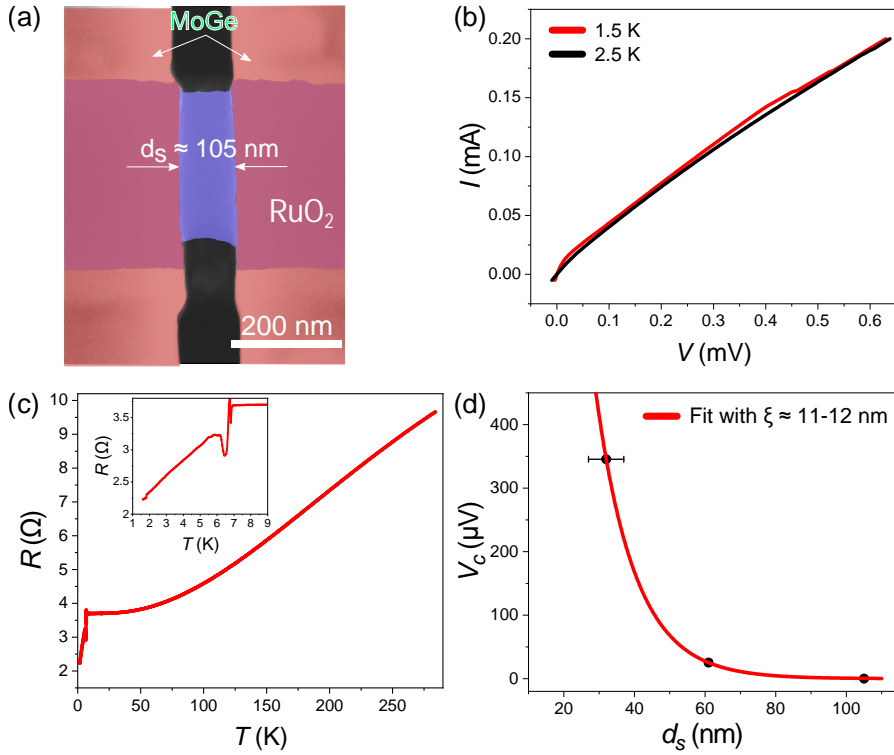
Figure 5.4: (a) SEM image of the device J3 where d_s = 105 nm. (b) I-V characteristics measured at 2.5 K (black) and 1.5 K(red) at zero-field shows very small non-linearity. (c) R(T) behavior of J3 measured from 280 K down to 1.5 K. Inset shows the R-T for temperature between 9 K to 1.5 K. A sharp drop in resistance is measured around 6.8 K signalling the superconducting transition MoGe. By 1.5 K, the normal state resistance of the wire has dropped by 41% which is a clear signature of partial proximization of the junction. (d) $V_c = I_c R_n$ as a function of d_s for the 3 JJ devices. The red curve is the fitted exponential decay function which gives coherence length (ξ) in RuO$_2$ of around 12 nm.

the midpoint of the resistive transition, was also different, about 5.5 K for J1, and about 4 K for J2. These devices, with the smallest gaps, showed clear Josephson junction behavior. Device J3 with a 105 nm gap proximized only partially, meaning that zero resistance was not reached till 1.5 K. Table 5.1 summarizes the basic device parameters.

5.4. Results and Discussion

We measured the zero-field current(I)-voltage(V) behavior of the two JJs J1 and J2 as function of temperature. Typical IV characteristics are shown in Fig. 5.3(a),

(c) while Fig. 5.3(b), (e) shows the color plot of I versus the derivative-dV/dI. We extracted the $I_c(T)$ from the onset of a change in the derivative, shown by the dotted line (green) in the Fig. 5.3(b), (e). We observed that the temperature of the onset of supercurrent coincides with the temperature of the midpoint of the resistive transition. At the lowest temperatures, I_c has become nearly constant. These low-temperature values show a strong decrease of I_c with increasing gap, dropping from 121 μA in J1 to 30 μA in J2.

We further fabricated and measured device J3 with a gap d_s = 105 nm, which did not reach zero resistance. Fig. 5.4a shows the R(T) measurement from 300 K down to 1.5 K. We observe that the resistance becomes constant below 10 K, with a value of 3.7 Ω around 8K. When the MoGe electrodes become superconducting at 6.8 K the resistance starts to decrease again (after a small dip-peak excursion) but does not reach 0 Ω. This behavior indicates that the RuO$_2$ wire did not proximize completely over the whole length of the junction. In contrast, a reduction of around 41% in resistance from the normal state resistance is seen when the temperature is lowered to 1.5 K. This reduction translates to a proximity length of about 20 nm extending from each contact.

Using the three JJ devices parameters, the coherence length ξ of the supercurrents can be estimated. For this we use the decay of the coupling strength, given by the product $I_c R_N = V_c$. This ensures that the actual dimensions of the bridge, as given by R_N, are taken into account correctly. We fit $V_c(d_s)$ using an exponential decay function $V_c(d_s) \propto exp(-\frac{d_s}{\xi})$. For our devices we estimate, $\xi \approx 12$ nm as shown in the Fig. 5.4(c). This matches quite well with the proximity length that we estimated to be induced in the longer junction J3. We also note that the order of magnitude reflects the size of the Ru-moment: in the collinear AF magnet IrMn, with a Mn moment of 3 μ_B, the coherence length was estimated 3 - 5 nm[14] (even quite large for such moments, possibly because it is an AF); in weak ferromagnets such as Pd$_{1-x}$Ni$_x$ or Cu$_{1-x}$Ni$_x$, it is found that the superconducting decay length (the dirty-limit coherence length ξ_F) is of the order of 5 nm for magnetic moments in the range 0.1 - 0.2 μ_B [24–26]. Finding 12 nm for an AF with moments of 0.05 μ_B appears quite reasonable. We further measured our devices in the magnetic field and observed a Fraunhofer-like damped oscillatory response of I_c, as expected for a Josephson Junction. Fig. 5.5(a), (b) shows the color plot of the magnetic field interference pattern $I_c(\mu_0 H)$. In the case of J1, we measured at a temperature of 2.5 K while the field was varied between -130 mT to 130 mT. For J2, we measured at 1.5 K while the field was varied from 0 to 185 mT. For J2 in particular, the first and second minimum, and thereby the width of the lobes, can be estimated fairly well to be about 45 mT. To interpret these data, we have to consider the following. In conventional Josephson junctions that are formed by a barrier sandwiched between two superconducting
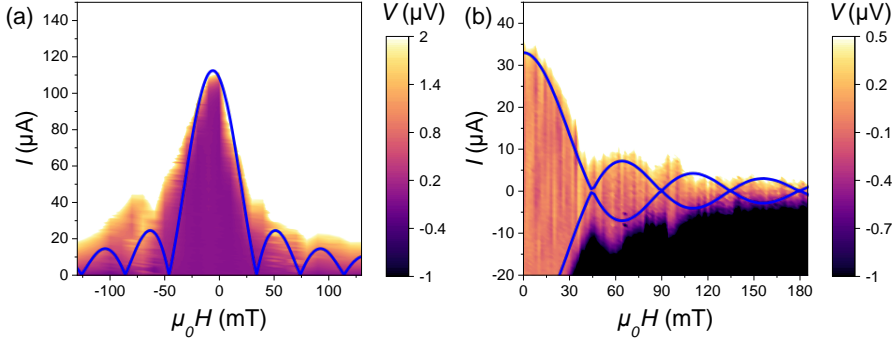
Figure 5.5: I-V characteristics of the JJ devices (a) J1 at 2.5 K and (b) J2 1.2 K when applying out of plane magnetic field. The blue curve is the simulated Fraunhofer pattern for our devices dimensions, representing the relation between critical current I_c and the applied magnetic flux.

electrodes, sometimes called overlap-type junctions, the (Fraunhofer) interference patterns can be described by

$$I_c(\mu_0 H) = I_c^{max} \left| \frac{\sin\left(\frac{\pi\Phi}{\Phi_0}\right)}{\frac{\pi\Phi}{\Phi_0}} \right| \qquad (5.1)$$

where I_c^{max} is the maximum critical current of the junction at zero field and $\Phi_0 = \frac{h}{2e}$ is the magnetic flux quantum (fluxoid). The magnetic flux ϕ is given by

$$\Phi = \mu_0 H A_{flux}^{eff}. \qquad (5.2)$$

Here, $\mu_0 H$ is the external applied magnetic field *in* the interface plane of the junction, and A_{flux}^{eff} is the effective area of the junction given by $(2\lambda_L + d_s)w$, with λ_L the London penetration depth and w the width of the junction device. Using this overlap-junction description for our planar junctions, but with the applied field now perpendicular to the junction plane, we note that zero values for I_c are reached when $\Phi = n\Phi_0$ (with n an integer), so the width of the lobes $\Delta(\mu_0 H) = \Delta B$ is given by $\Delta B = \Phi_0 / A_{flux}^{eff}$. Using the lobe width of 45 mT, this would lead to $A_{flux}^{eff} \approx$ 0.045 μm^2. However, when calculating A_{flux}^{eff} from the values of w ≈ 250 nm (width of the devices), and $\lambda_L \approx 580$ nm[27, 28], we obtain $A_{flux}^{eff} \approx 0.32\ \mu m^2$, which is a very different and also unrealistic number. For completeness, we display a simulated Fraunhofer pattern for the measured lobe width in Fig. 5.5(a), (b) (blue curve).

The reason for erroneous calculation of A_{flux}^{eff} is that the junction physics becomes different when the thickness of the superconducting electrodes is less than their London penetration depth, as is often the case for planar junctions. Additionally, when the junction width w becomes smaller than the Josephson penetration

length ℓ_J given by $\Phi_0/(4\pi\mu_0\lambda_L^2 j_c(0))$, with j_c being the (presumed homogeneous) critical current density of the junction. In this scenario, as has been discussed in numerous studies, the electrodynamics becomes non-local, and $I_c(B)$ becomes independent of λ_L and is solely determined by the geometry of the device [29–33]. In our junctions, the thickness d of the MoGe layer (100 nm) is smaller than the bulk London penetration depth (580 nm). Consequently, the relevant penetration depth for the electrodes is given by the Pearl length $\Lambda = 2\lambda_L^2/d$. The calculated Λ is $\approx$ $6.7\mu m$, which is significantly larger than the size of electrodes. Using the measured $I_c(0)$ of about 0.1 mA through a cross-section of $w = 250$ nm and thickness $t = 100$ nm, we estimate ℓ_J to be ≈ 97 nm. The junction width is actually somewhat lager than this, but it was discussed in Ref.[32] that non-local electrodynamics still apply. The simple answer for the lobe width in the interference pattern is that $\Delta B = 1.84\Phi_0/w^2$[31, 33].The lobe width $\Delta B = 45$ nm then corresponds to a junction width of 290 nm, quite close to the actual number. We conclude that, under a perpendicular magnetic field, our junctions show the behavior expected for planar junctions.

5.5. Summary

In summary, we have grown high quality RuO_2 nanowires using the Selective Area (SA) growth on a TiO_2 substrate and used these to fabricate planar Josephson junctions with the RuO_2 wire as a weak link. We find these links not to behave as a normal metal; rather, the pair breaking effects are similar to what is found in weak ferromagnets such as CuNi and PdNi. The estimated coherence length of the weak link is about 12 nm. Moreover, the junctions behave as expected for planar junctions of such dimensions under the application of a magnetic field.

5.6. Appendix

5.6.1. A shorted junction

We also measured a device where voltage probes are shorted. Fig. 5.6(a) shows that at the device becomes superconducting below the T_c of MoGe. The response of the device in magnetic field as expected shows the current hardly varies. This is in sharp contrast to the Fraunhofer-like pattern of junctions in Fig. 5.5.
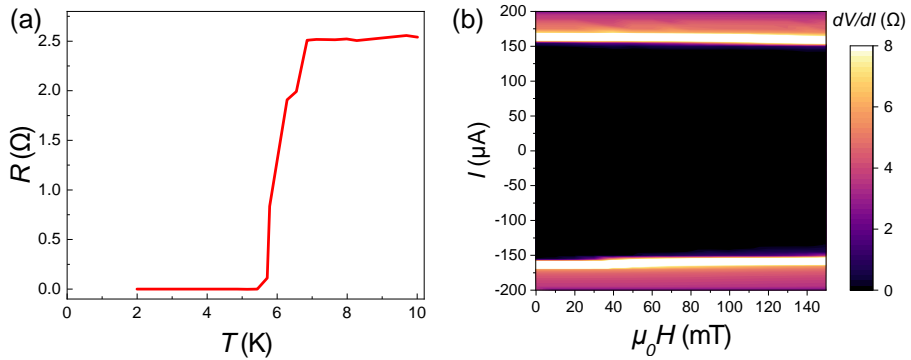

Figure 5.6: (a) R(T) between 10 K to 2 K of a shorted -junction device. The device becomes superconducting below 6K. (b) Color plot of I($\mu_0 H$)of a shorted-junction device measured at 2 K. Field is applied out of plane to the device interface and varied from 0 to 150 mT. As expected current (I) stays almost constant under the whole range of field.

5.6.2. Closeup of a RuO$_2$ nanowire
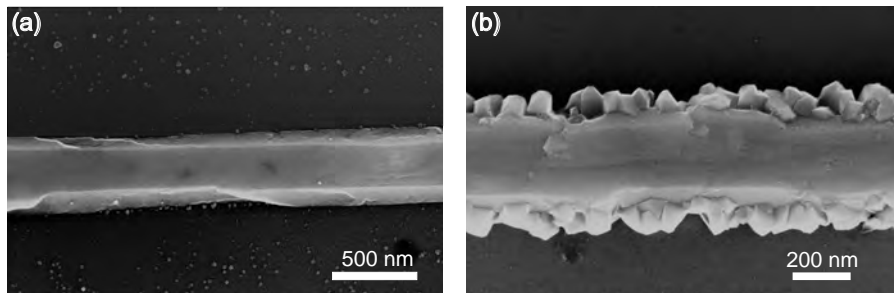
Figure 5.7: High resolution close up SEM images of two RuO$_2$ nanowires

Fig. 5.7 shows a high resolution scanning eletron micrograph of two epitaxially grown RuO$_2$ nanowires of similar width of around 250 nm. In both cases, well defined crystal facets can be seen clearly. In (a) the width of the wire is completely inside the trench. There are very small and thin crystals on SiOx but away from the trench. However, for (b) thin crystal shards are attached to the side along the length of the wire. A probable explanation is that RuO$_2$ is known to grow on SiOx surface. The growth on SiOx is at a much slower rate. At the edge of the trench on both sides, these small crystals merged with the wire to give the above irregular growth.

References

[1] Sun, Y., Zhang, Y., Liu, C.-X., Felser, C. & Yan, B. Dirac nodal lines and induced spin hall effect in metallic rutile oxides. Phys. Rev. B **95**, 235104 (2017). URL https://link.aps.org/doi/10.1103/PhysRevB.95.235104.

[2] Wang, R. et al. Nodal line fermions in magnetic oxides. Phys. Rev. B **97**, 241111 (2018). URL https://link.aps.org/doi/10.1103/PhysRevB.97.241111.

[3] Dismukes, J. P., Martin, D. F., Ekstrom, L., Wang, C. C. & Coutts, M. D. Ferromagnetic chromium dioxide for magnetic tape. Ind. Eng. Chem. Prod. Res. Dev. **10**, 319 (1971). URL https://doi.org/10.1021/i360039a013.

[4] Keizer, R. S. et al. A spin triplet supercurrent through the half-metallic ferromagnet CrO_2. Nature **439**, 825–827 (2006). URL http://dx.doi.org/10.1038/nature04499.

[5] Anwar, M. S., Veldhorst, M., Brinkman, A. & Aarts, J. Long range supercurrents in ferromagnetic CrO_2 using a multilayer contact structure. Appl. Phys. Lett. **100**, 052602 (2012). URL http://aip.scitation.org/doi/10.1063/1.3681138.

[6] Singh, A., Jansen, C., Lahabi, K. & Aarts, J. High-Quality CrO_2 Nanowires for Dissipation-less Spintronics. Phys. Rev. X **6**, 041012 (2016). URL https://link.aps.org/doi/10.1103/PhysRevX.6.041012.

[7] Fujiwara, K. et al. 5d iridium oxide as a material for spin-current detection. Nature Comm. **4**, 2893 (2013). URL http://dx.doi.org/10.1038/ncomms3893.

[8] Qiu, Z., Hou, D., Kikkawa, T., i Uchida, K. & Saitoh, E. All-oxide spin seebeck effects. Appl. Phys. Express **8**, 083001 (2015). URL http://dx.doi.org/10.7567/APEX.8.083001.

[9] Berlijn, T. et al. Itinerant antiferromagnetism in RuO_2. Phys. Rev. Lett. **118**, 077201 (2017). URL https://doi.org/10.1103/PhysRevLett.118.077201.

[10] Zhu, Z. H. et al. Anomalous antiferromagnetism in metallic RuO_2 determined by resonant x-ray scattering. Phys. Rev. Lett. **122**, 017202 (2019). URL https://link.aps.org/doi/10.1103/PhysRevLett.122.017202.

[11] Šmejkal, L., González-Hernández, R., Jungwirth, T. & Sinova, J. Crystal time-reversal symmetry breaking and spontaneous hall effect in collinear antiferromagnets. Science Advances **6**, eaaz8809 (2020). URL https://www.science.

org/doi/abs/10.1126/sciadv.aaz8809. https://www.science.org/doi/pdf/10.1126/sciadv.aaz8809.

[12] Feng, Z. et al. An anomalous hall effect in altermagnetic ruthenium dioxide. Nature Electronics **5**, 735–743 (2022). URL https://doi.org/10.1038/s41928-022-00866-z.

[13] Uchida, M., Nomoto, T., Musashi, M., Arita, R. & Kawasaki, M. Superconductivity in uniquely strained RuO_2 films. Phys. Rev. Lett. **125**, 147001 (2020). URL https://doi.org/10.1103/PhysRevLett.125.147001.

[14] Jeon, K.-R. et al. Long-range supercurrents through a chiral non-collinear antiferromagnet in lateral josephson junctions. Nature Materials **20**, 1358–1363 (2021). URL https://doi.org/10.1038/s41563-021-01061-9.

[15] Selte, K., Kjekshus, A., Andresen, A. F. & Pearson, W. B. A neutron diffraction study of magnetic ordering in the irmn phase. Acta Chem. Scand. **22**, 3039 (1968).

[16] Ahn, K.-H., Hariki, A., Lee, K.-W. & Kuneš, J. Antiferromagnetism in RuO_2 as d-wave pomeranchuk instability. Phys. Rev. B **99**, 184432 (2019). URL https://link.aps.org/doi/10.1103/PhysRevB.99.184432.

[17] Hayami, S., Yanagi, Y. & Kusunose, H. Momentum-dependent spin splitting by collinear antiferromagnetic ordering. Journal of the Physical Society of Japan **88**, 123702 (2019). URL https://doi.org/10.7566/JPSJ.88.123702. https://doi.org/10.7566/JPSJ.88.123702.

[18] Šmejkal, L., Sinova, J. & Jungwirth, T. Beyond conventional ferromagnetism and antiferromagnetism: A phase with nonrelativistic spin and crystal rotation symmetry. Phys. Rev. X **12**, 031042 (2022). URL https://link.aps.org/doi/10.1103/PhysRevX.12.031042.

[19] Bai, H. et al. Observation of spin splitting torque in a collinear antiferromagnet ruo₂. Phys. Rev. Lett. **128**, 197202 (2022). URL https://link.aps.org/doi/10.1103/PhysRevLett.128.197202.

[20] Bose, A. et al. Tilted spin current generated by the collinear antiferromagnet ruthenium dioxide. Nature Electronics **5**, 267–274 (2022). URL https://doi.org/10.1038/s41928-022-00744-8.

[21] Karube, S. et al. Observation of spin-splitter torque in collinear antiferromagnetic RuO_2. Phys. Rev. Lett. **129**, 137201 (2022). URL https://link.aps.org/doi/10.1103/PhysRevLett.129.137201.

[22] Prateek, K. et al. Magnetotransport properties of CrO_2 nanowires fabricated by selective area growth. Journal of Physics and Chemistry of Solids **178**, 111350 (2023). URL https://www.sciencedirect.com/science/article/pii/S0022369723001403.

[23] Si, J. & Desu, S. B. RuO_2 films by metal-organic chemical vapor deposition. Journal of Materials Research **8**, 2644–2648 (1993). URL https://doi.org/10.1557/JMR.1993.2644.

[24] Cirillo, C. et al. Superconducting proximity effect and interface transparency in nb/pdni bilayers. Phys. Rev. B **72**, 144511 (2005). URL https://link.aps.org/doi/10.1103/PhysRevB.72.144511.

[25] Rusanov, A., Boogaard, R., Hesselberth, M., Sellier, H. & Aarts, J. Inhomogeneous superconductivity induced in a weak ferromagnet. Physica C **369**, 300 (2002).

[26] Oboznov, V. A., Bol'ginov, V. V., Feofanov, A. K., Ryazanov, V. V. & Buzdin, A. I. Thickness dependence of the josephson ground states of superconductor-ferromagnet-superconductor junctions. Phys. Rev. B **96**, 197003 (2006). URL https://link.aps.org/doi/10.1103/PhysRevLett.96.197003.

[27] Motta, M. et al. Controllable morphology of flux avalanches in microstructured superconductors. Phys. Rev. B **89**, 134508 (2014). URL https://link.aps.org/doi/10.1103/PhysRevB.89.134508.

[28] Draskovic, J. et al. Measuring the superconducting coherence length in thin films using a two-coil experiment. Phys. Rev. B **88**, 134516 (2013). URL https://link.aps.org/doi/10.1103/PhysRevB.88.134516.

[29] Kogan, V. G., Dobrovitski, V. V., Clem, J. R., Matawari, Y. & Mints, R. G. Josephson junction in a thin film. Phys. Rev. B **63**, 144501 (2001). URL https://link.aps.org/doi/10.1103/PhysRevB.63.144501.

[30] Moshe, M., Kogan, V. G. & Mints, R. G. Edge-type josephson junctions in narrow thin-film strips. Phys. Rev. B **78**, 020510R (2008). URL https://link.aps.org/doi/10.1103/PhysRevB.78.020510.

[31] Clem, J. R. Josephson junctions in thin and narrow rectangular superconducting strips. Phys. Rev. B **81**, 144515 (2010). URL https://link.aps.org/doi/10.1103/PhysRevB.81.144515.

[32] Boris, A. A. et al. Evidence for nonlocal electrodynamics in planar josephson junctions. Phys. Rev. Lett. **111**, 117002 (2013). URL https://link.aps.org/doi/10.1103/PhysRevLett.111.117002.

[33] Fermin, R., de Wit, B. & Aarts, J. Beyond the effective length: How to analyze magnetic interference patterns of thin-film planar josephson junctions with finite lateral dimensions. Phys. Rev. B **107**, 064502 (2023). URL `https://link.aps.org/doi/10.1103/PhysRevB.107.064502`.

6

Josephson Junctions with CrO$_2$ Nanowires

Half-metallic systems such as CrO$_2$ are an ideal candidate to investigate very long range proximity effects in S/F hybrids. Although CrO$_2$ holds great potential for superconducting spintronics, its metastability at ambient temperatures has slowed research. In this work, we have fabricated CrO$_2$ junctions with two distinct methods to address this issue. The first method involves removing the Cr$_2$O$_3$ layer by standard Ar-etching of the top surface of CrO$_2$. We evaluated the impact of etching on interface transparency in over many (> 50) devices and observed a very wide spread of interface resistance for the same etch parameters, indicating lack of control and consistency required to observe the desired effects. The second approach employs a protective layer of RuO$_2$ which was grown in situ with CrO$_2$ in CVD with customized arrangements. The RuO$_2$ layer results in low contact resistances of around 1 Ω. However, we found the thickness of RuO$_2$ to be above 50 nm for a very short growth time of 5 sec. Due to its short coherence length of 12 nm, the considerable thickness of RuO$_2$ prevents the long range proximity effect in these devices. Further optimization of growth settings is needed to attain the target thickness of around 5 nm.

6.1. Introduction

The interplay between conventional superconductivity and ferromagnetism in superconductor-ferromagnet (S/F) hybrid structures produces a novel form of equal spin triplet superconducting correlations [1]. The triplets, denoted as $|\uparrow\uparrow\rangle$ and $|\downarrow\downarrow\rangle$ in Dirac notation, have parallel spins. Consequently, they are less affected by the pair breaking due to exchange field in the ferromagnet. This facilitates the propagation of triplet pairs over significantly greater distances within the F layer [2]. The phenomenon known as long range proximity (LRP) effect was first proposed by Bergeret et al. in 2001. Since then, in the last two decades, this field has been studied extensively [3–15], primarily focusing on generation and control of superconducting triplet correlations. The key ingredient in conversion from singlet-to-triplet is the engineering of magnetic inhomogeneity through spin mixing and spin rotation at the S/F interface. Experimentally, magnetic inhomogeneity can be introduced through vertical multilayer stacks with different magnetic materials and magnetization directions (for eg. $S/F_0/F/F_0/S$) [16, 17] or magnetic textures like ferromagnetic domain walls [1, 18–20] or interfaces with magnetic disorder [21, 22]. Triplet supercurrents are by definition spin-polarized, and they bear great promise for a new kind of superconducting electronics, in which not only the charge and the superconducting phase, but also the spin is utilised. Some of the potential applications include : use of the supercurrent to generate a spin torque on a nanomagnet and bring its magnetization into motion which can lead to high-frequency oscillators and cryogenic memories; use of the supercurrent to move domain walls; Josephson φ_0-junction-based phase batteries to provide phase shifts in superconducting circuits [23]; or Josephson diodes where the superconducting critical current of the junction depends on the direction of the current [24].

Half-metallic ferromagnets (HMF) like CrO_2 are particularly interesting due to their ability to sustain remarkably high supercurrents (of the order of 10^{10} A/m^2) over hundreds of nanometers [3, 12, 14]. This is in sharp contrast to conventional ferromagnets like Ni, Co, and Fe, which typically exhibit supercurrents over much shorter distances, in the range of a few tens of nanometers. In 2006, Keizer et. al. first reported spin triplet supercurrent in a Jospehson Junction (JJ) device comprising two s-wave superconducting electrodes of NbTiN separated by distances of up to 1 μm on a 100 nm thick film of CrO_2 grown on a TiO_2 substrate (see Fig. 6.1 (b)). However, they found large spread in the critical currents for different devices which suggested that the mechanism responsible for the singlet to triplet conversion was not very clear. In particular a quantitative analysis, comparing the critical current of HMF-based Josephson junctions with the existing theoretical framework [21], was not feasible. In 2010, Anwar *et al.* reported similar results on CrO_2 films grown on Al_2O_3 substrates with MoGe as superconducting contacts. These devices again had

no built-in triplet generator, and the reproducibility was poor (less than 30%) [12]. Later in 2012, Anwar et al. observed long range suppercurrents on CrO_2 deposited on TiO_2 substrates. A thin sandwich layer of Ni (2 nm)/Cu (5 nm) was used between CrO_2 film and the superconducting MoGe to introduce the necessary magnetic inhomogeneity for spin triplet generation.

The above three work were conducted on 'full-film' devices which suffers from a significant limitation due to presence of grain boundaries and ill-defined current paths and an insufficient understanding of the magnetization state at the local level. Fig. 6.1(c) (top) shows the AFM image of the morphology of a CrO_2 film in which the grain boundaries are clearly visible; while Fig. 6.1(c)(bottom) shows its corresponding MFM image. The contrast in the MFM image is due to stray field and indicates that the magnetic configuration over the film is not homogeneous. This may result in poorly controlled magnetic inhomogeneity at the S/F interface which is crucial for triplet generation. Fig. 6.1(d) shows an $R(T)$ plot for two different junctions based on a CrO_2 wire obtained by Ar etching the full film. One of the junction proximizes while the other junction does not, which suggests poor reproducibility of these junctions.

In 2016, Singh et. al. reported SA-grown CrO_2 nanowires based lateral JJs. A sandwich layer of Cu (or Ag)/Ni at the interface of CrO_2 and MoGe was used to provide the necessary magnetic non-collinearity. The junctions could sustain supercurrents of the order of 10^9 A/m^2 below 5 K for a junction length of 500 nm [25]. The potential of CrO_2 for superconducting spintronics is evident; however, advancements in this area have been hindered due to the metastability of CrO_2 at room temperature. CrO_2 reduces into insulating Cr_2O_3 (see Sec. 6.2 for details) resulting in a poorly controlled S-F interface transparency which is critical for generation of spin triplets. In this study, we have fabricated junction devices with CrO_2 nanowires using two distinct methods to address this issue. The first method employs Ar-etching of the top surface of CrO_2 to remove Cr_2O_3 before depositing the contacts. We have systematically analyzed the effects of etching on the interface transparency between CrO_2 and the contact electrodes comprising Ag/Ni/MoGe trilayer stack by varying the etching time. Similar to the initial studies and contrary to report by Singh *et. al.* we found a lack of reproducibility across multiple measurements for the same growth and etch parameters. In the second method a thin layer of RuO_2 is grown in situ on CrO_2 before contacting the wires. This method demonstrates initial potential wherein very high transparency of interface is achieved. However, the growth of the RuO_2 layer, specifically its thickness, needs further optimization to observe LRP effects in the devices. In the following sections both methods of junction fabrication are discussed and the results on them presented.
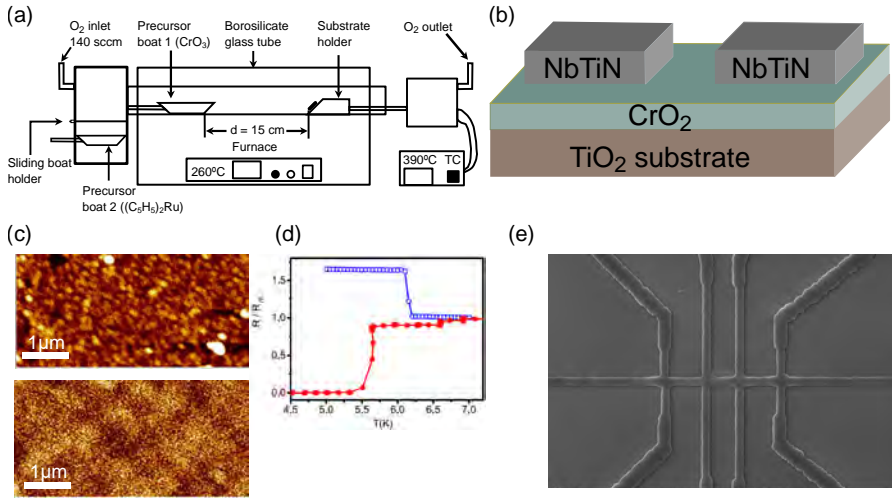
Figure 6.1: (a) Schematic of the CVD setup used for growth of CrO$_2$. The same setup allows for in-situ deposition of a RuO$_2$ layer on top of CrO$_2$. To grow RuO$_2$, precursor boat1 containing CrO$_3$ is pulled back out of the glass tube and can be placed in the sealed chamber; and precursor boat2 containing ruthenocene (C$_5$H$_5$)$_2$Ru is introduced in the glass tube. The temperature of the furnace when growing RuO$_2$ is kept at 80 °C. The substrate temperature is maintained at 390 °C for whole the duration of growth. (b) Schematic of the SFS junction fabricated by depositing superconducting NbTiN electrodes over CrO$_2$ film on a TiO$_2$ substrate with lateral gaps of the order of micron. Adapted from Ref. [3]. (c) Atomic force microscopy (AFM) image (top) and magnetic force microscopy (MFM) image (bottom) of a CrO$_2$ film. The contrast in the MFM image is due to stray fields and shows that magnetic configuration of the CrO$_2$ film is random, which may result in ill-defined magnetic inhomogeneity at the S-F interface. (d) Resistance vs temperature plot for two junctions based on a CrO$_2$ wire, obtained by Ar etching the full film, shows the poor reproducibility of these junctions. The success rate of CrO$_2$-film junctions was less than 10%. Taken from Ref. [25]. (e) SEM image of a selective area grown CrO$_2$ nanowire. Making junctions based on SA-grown nanowires should result in more control over the local magnetization due to shape anisotropy. *Schematic not drawn to scale.

6.2. Experimental details

As mentioned above, CrO$_2$ is metastable at ambient conditions and decomposes to a more thermodynamically stable Cr$_2$O$_3$ state, which is antiferromagnetic and an insulator [26, 27]. Cheng et al. used photoemission and inverse photoemission to characterize the thickness of Cr$_2$O$_3$ layer and they found it to be much thicker than the oxygen core level photoelectron mean free path (around 2 nm) for organometallic chemical vapor deposition grown CrO$_2$. This insulating barrier prevents developing a good metallic contact on CrO$_2$ and complicates the fabrication process. From angle resolved x-ray photoemission (ARXPS) and ultraviolet photoemission experiments, it is known that the deposition of transition metal on CrO$_2$ surface leads to further oxidation and reduction, making the metal-CrO$_2$

interface very inhomogeneous [28].

Since CrO_2 is metastable, conventional methods for film growth such as sputtering, pulsed laser deposition, or molecular-beam epitaxy cannot be used. Instead chemical-vapor deposition (CVD) has to be employed which prevents in-situ deposition of a protective metal layer over CrO_2. Furthermore, cool-down in the CVD furnace is already an uncontrolled event that may start the Cr_2O_3 conversion. In this work, CrO_2 based lateral S−F−S Josephson junctions (JJs) devices were fabricated using two different approaches to work around the Cr_2O_3 layer problem, which will be discussed in the following sections. Both methods start with the growth of epitaxial CrO_2 wires along [001] direction on a TiO_2 (100) substrate using the Selective Area growth technique via chemical vapor deposition (CVD). Schematic of the CVD set up is shown in Fig. 6.1 (a). and details of the growth process has been described in Chapter 3.2.

For the first method (see Fig. 6.2(a)), CrO_2 wires were grown followed by patterning desired contacts using e-beam lithography. The top surface of CrO_2 was then etched using an argon (Ar) plasma to remove the Cr_2O_3 layer prior to contacts deposition. The tri-layer contacts comprising Ag (5 nm), Ni (2 nm) and the superconductor $Mo_{70}Ge_{30}$ (150 nm; for simplicity called MoGe) were sputter deposited at a pressure of 5×10^{-3} mbar. This was followed by a lift-off process. The etching was carried out in the same sputtering system without breaking the vacuum by reversing the polarity of the plasma, using a pressure of 5×10^{-3} mbar and a bias voltage of 700 V. The Ag (or Cu) acts as a spacer layer and is used to decouple the two ferromagnets. Ni acts as a mixer layer and is used to achieve magnetic inhomogeneity at the interface. By ensuring Ni magnetization perpendicular to the CrO_2 wire, maximum possible magnetic non-collinearity at the S-F interface can be achieved, resulting in an efficient triplet Cooper pair generation.

In the second approach, Ag was substituted with a layer of RuO_2 which is a weak antiferromagnet and a metal. RuO_2 is inert when exposed to typical atmospheric conditions, and can be deposited epitaxially on top of CrO_2 (see Fig. 6.1 (a)) due to their similar lattice parameters. To grow RuO_2 specific arrangements were made in the CVD set up to accommodate the two precursors boats which can be introduced into the glass tube sequentially without affecting the other precursor using the sliding holder. Initially, CrO_2 is grown as shown in Fig. 6.1 using the precursor boat1 in the glass tube. The furnace temperature is set at 260 °C. After the growth of CrO_2 is finished, precursor boat1 containing CrO_3 is pulled back out of the glass tube and can be placed in a closed chamber by shifting the sliding holder up. The temperature of the furnace is brought down to 80 °C. After that, precursor boat2 containing ruthenocene is placed in the glass tube for RuO_2 growth for around 5 sec before boat2 is also removed from the glass tube. The temperature of substrate holder is
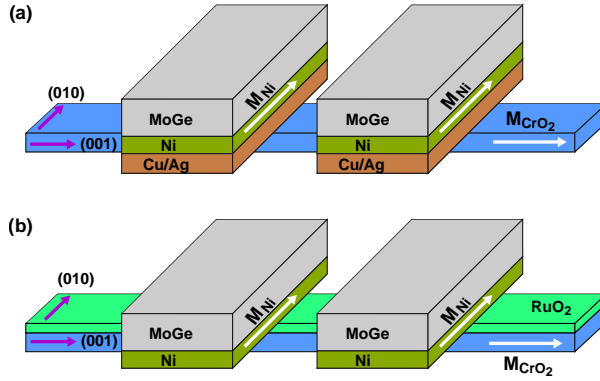
Figure 6.2: Schematic representation of the two different approaches used for fabrication of CrO$_2$-based lateral S−F−S Josephson junctions (JJs). White arrows indicate the magnetization direction of CrO$_2$ (M$_{CrO_2}$) and Ni (M$_{Ni}$) while purple arrows show the crystal axis. (a) In first approach, the central CrO$_2$ wire (blue) is first etched to remove the insulating oxide layer of Cr$_2$O$_3$ and then tri-layer contacts comprising Cu or Ag/Ni/MoGe were deposited to make the device. (b) In the second approach, a thin layer of RuO$_2$ was grown in situ on top of CrO$_2$ wire and then bi-layer Ni/MoGe contacts were deposited without the need of etching. *Schematic not drawn to scale.

maintained at 390 °C for the whole duration of growth. RuO$_2$ is inert at ambient conditions, so it prevents the formation of Cr$_2$O$_3$ and protects the CrO$_2$ layer, thus eliminating the need for further etching. Next, the contacts were patterned, followed by deposition and lift-off of bi-layer of Ni(2 nm)/MoGe(200 nm).

The fabrication process was followed by the characterization of the device. Initially, two-probe measurements were done at room temperature to check the contact leads, followed by a four-point connection (Current leads: 9-7, Voltage leads: 11-10) as shown in Fig. 6.3(b) (inset)) that allowed a direct measurement of the central CrO$_2$ wire resistance without the contact wire resistance. Further, electrical and magnetotransport measurements were performed in a Physical Property Measurement System (PPMS) that could be cooled down to a base temperature of 2 K. The magnetic field could be applied along z-axis up to 9 T. We used a Keithley model 6221 low Noise Precision AC/DC Current Source to provide dc current and a Keithley model 2182A digital nanovoltmeter to measure the voltage.

6.3. CrO$_2$ junctions fabricated by etching process

It is by now well established that a thin insulating layer of Cr$_2$O$_3$ forms on top of the CrO$_2$ surface exposed to atmospheric conditions. To get a comprehensive understanding of the impact of such a barrier on CrO$_2$ junctions, our initial emphasis
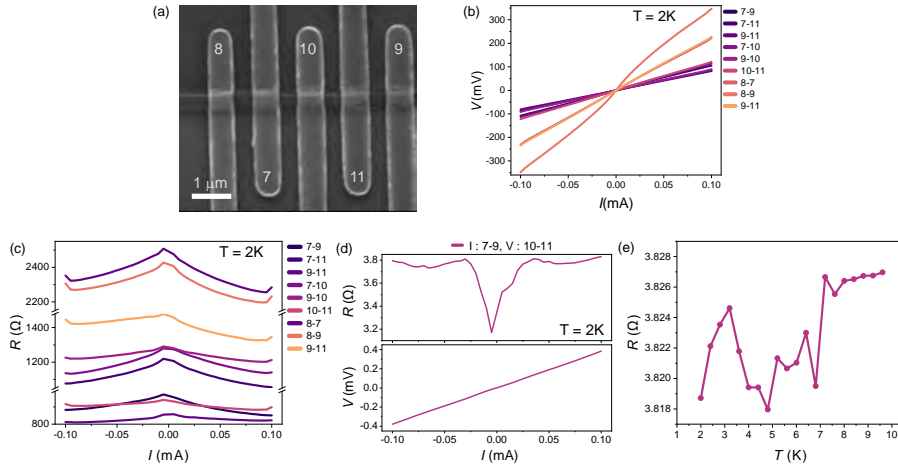
Figure 6.3: No-etch CrO$_2$ junctions. (a) SEM image of the device consisting of CrO$_2$ wire of width 370 nm along [001] and multiple contact leads comprising a Ag/Ni/MoGe stack across the CrO$_2$. The contact leads have edge to edge separation of around 405 nm. (b) Two-point voltage vs current (I-V) plots for different contact configurations on device B measured at 2 K. (c) The corresponding 2 probe resistance as a function of current (R-I). (d) Four-point I-V and the corresponding R-I plot of the central CrO$_2$ wire. (e) Four-point $R(T)$ measurement between 10 K and 2 K of the central CrO$_2$ wire between contacts 10-11. A small drop in resistance is observed around T$_c$ of MoGe; after that it oscillates to finally reach 3.818 Ω at 2 K, without a visible proximity effect.

was on a device without etching. This would help with the basic characterization of the device and thereafter serve as a reference point for correlating with the effect of etching of the CrO$_2$ surface. Subsequently, a series of devices was fabricated with varying etch times in order to determine the optimal time required for our devices. Etching plays a critical role in achieving a good metallic interface between CrO$_2$ and Ag/Ni/MoGe contact leads. The outcome of underetching is evident as it would result in partial removal of Cr$_2$O$_3$ layer. Overetching is also detrimental as it would damage the underlying CrO$_2$ surface. It should be feasible to manipulate the interface transparency by varying the duration of etching in a systematic manner and identify an appropriate range of etch time for the fabrication of proximized CrO$_2$ JJs.

6.3.1. Device without etching

In this section, we present the results of measurements conducted on CrO$_2$ junction device fabricated without etching step. Fig. 6.3(a) shows the scanning electron micrograph of a fabricated junction device consisting of a central CrO$_2$ wire of width around 370 nm along [001] and multiple contact leads comprising Ag/Ni/MoGe

stack across the CrO$_2$ wire. The contact leads have lateral edge to edge separation of around 405 nm. To characterize the interface between CrO$_2$ and contact leads, the device was measured in a 2-probe configuration. Fig. 6.3(b) shows the two-probe voltage vs current (I-V) plots for different contact lead configurations, with the contacts labeled in the SEM image. The measurement (e.g. 7-8 meaning from contact 7 to contact 8) gives the combined resistance of two interfaces. The measurements were at 2 K, which is well below the superconducting transition temperature (T_c) of 6.5 K for MoGe. At 2 K, the measured resistance should have most of the contribution from the interface resistance. While certain I-V curves may appear linear, leading one to assume an ohmic nature of the interfaces, the non-ohmic behavior becomes apparent in the resistance vs current plot (see Fig. 6.3(c)) which indicates that the interfaces are indeed not metallic and the CrO$_2$ layer is effectively decoupled from the contact leads. Each measurement shows a high resistance of the interfaces, the minimum being above 800 Ω and maximum around 2400 Ω. This suggests local variation among the five interfaces on the same device. We also measured the behavior of the central CrO$_2$ wire without the contribution coming from contact leads in 4-point geometry. Fig. 6.3(d)) shows the I-V plot (bottom) and the corresponding R-I plot of CrO$_2$ wire between inner contact leads. The resistance was found to be around 3.8 Ω at 2 K which is typical for CrO$_2$ wires of such dimensions. However, the R-I plot shows non-ohmic type behavior of the wire, the underlying cause of which remains unclear to us. Finally, we measured 4-point geometry resistance vs temperature measurement on a junction device between 10 K and 2 K as shown in Fig. 6.3(e). The resistance at 10 K is around 3.827 Ω. A small drop in resistance is observed around T$_c$ of MoGe but after that it oscillates to finally reach 3.818 Ω at 2 K and as anticipated, no proximity effect was detected.

6.3.2. Device with etching

After measuring devices without etching, we made a series of devices with different etching times in our quest to find the optimal range. Fig. 6.4(a) shows the resistance vs etch time plot of different devices, measured in a 4-point geometry at 2 K, as the etching time is varied from 0 s up to 90 s. We fabricated multiple devices with the same etch time and in the Figure we chose a random device from the series to represent an etch time. We observed a non-monotonous behavior up to 40 sec of etching beyond which the resistance goes up sharply, suggesting that we are overetching and probably damaging the CrO$_2$ wire. We found the best results on our devices around 20-25 sec of etch time, but no clear window of the etch times was observed which led to proximization of the CrO$_2$ junction. This result is contrary to the earlier report by Singh et al. where they found a well defined etching time to see proximity effect [25].
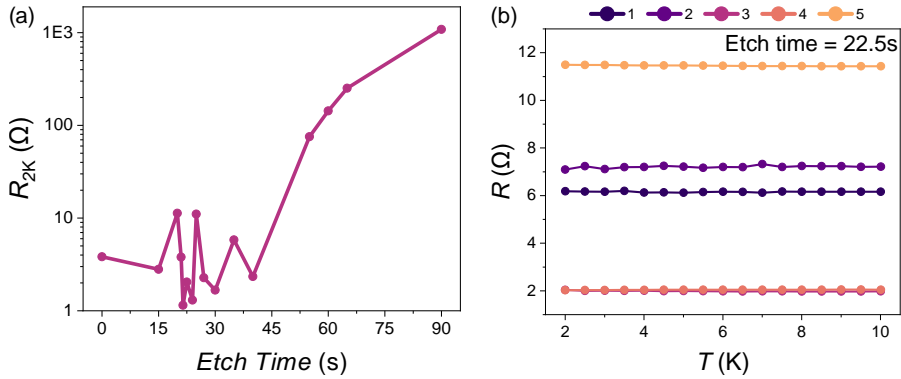
Figure 6.4: (a) Resistance vs etch time plot of different devices measured at 2 K as the etch time is varied from 0 s up to 90 s. Multiple devices were measured for the same etch times, out of which we chose one of the device randomly to be represented in the graph. (b) Four-point resistance vs temperature of CrO$_2$ wire for five different devices etched for same time of 22.5 s, showing small differences in the measured resistance.

We observed a large spread in interface resistances for the same etching time not only across various devices but even on the same CrO$_2$ wire. We found interface resistances to be at their lowest for etch time around 20-25 sec. Around this time, the observed interface resistance ranged from as low as 20 Ω to as high as 10 KΩ (not shown in figure). Although the interfaces showed large variations in resistances, we found the 4-point geometry wire resistance (without interfaces) to be consistent. This indicates that the quality of CrO$_2$ wire is not a factor. Fig. 6.4(b) gives the four-point resistance vs temperature of CrO$_2$ wire in five different devices etched for same time of 22.5 s. These devices show small spread in the measured resistance which is probably due to small difference in the device dimensions, however none of them showed a proximity effect.

In Fig.6.5, we present the measurements of one of the CrO$_2$ junction device which was etched for 22.5 s. Fig.6.5 (a) shows the SEM image of the device comprising CrO$_2$ wire of width (w) = 512 nm, thickness (t) = 65 nm and multiple Ag/Ni/MoGe contact leads. The two inner contact leads are edge to edge separated by 350 nm. Fig.6.5 (b) gives the 2-point I-V (top) and corresponding R-I plots of the contact leads (without interface) measured at 10 K, well above T_c. R-I plots confirm that the contact leads are ohmic and indeed metallic. Subsequently, we measured the device in the quasi 4-point geometry configuration. This configuration allows to measure the resistance of CrO$_2$ wire along the two interface between CrO$_2$ and Ag/Ni/MoGe on either side of the central CrO$_2$ wire (see Fig. 6.2). Fig. 6.5(c,d) show the I-V and corresponding R-I plots in different combinations measured at 2 K. We calculated the interface resistance at each of the four interfaces. Moving from left to right,
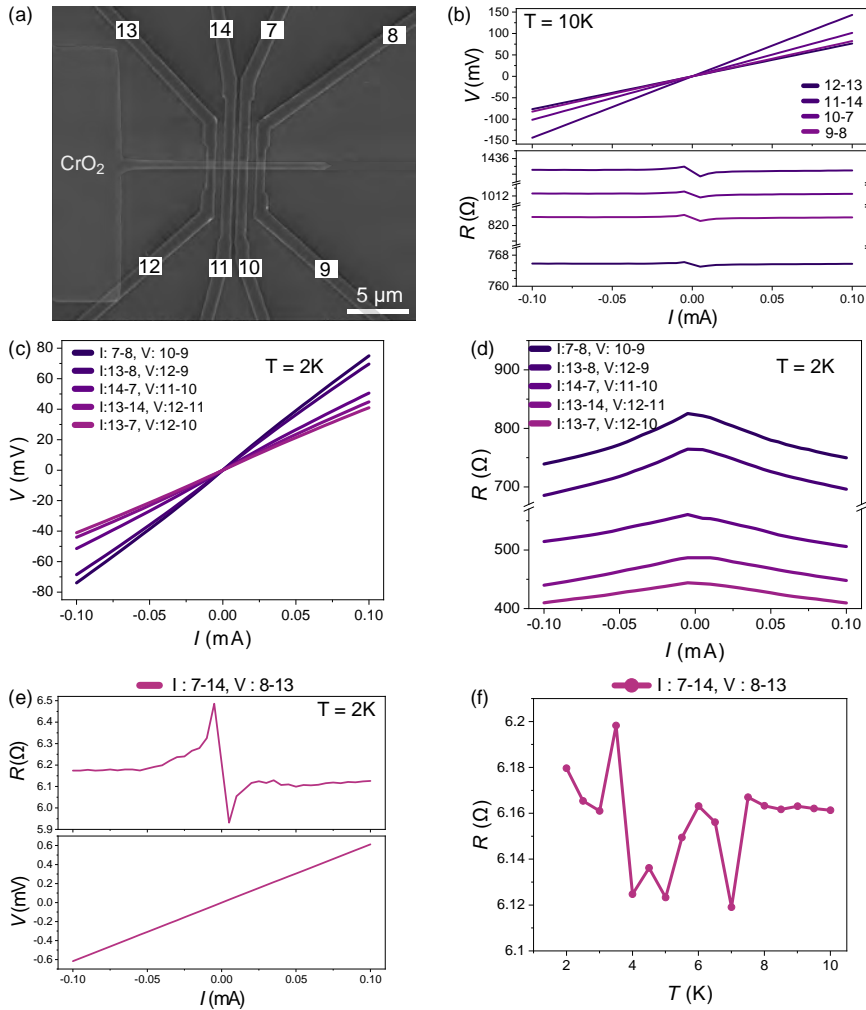
Figure 6.5: SEM image (false color) of one of the CrO$_2$ junctions fabricated using the first approach of etching the top surface of CrO$_2$ before depositing tri-layer (Ag/Ni/MoGe) contacts. The two inner contacts are laterally edge-to-edge separated by ∼ 350 nm. This device was etched for 22.5 s. (b) 2-point I-V and corresponding R-I plots of the contact leads (without interface) measured at 10 K before T_c. R-I shows good ohmic behavior. (c) Quasi 4-point I-V and the corresponding (d) R-I plot of the central CrO$_2$ wire and the two interfaces in different configurations measured at 2 K. The interfaces have resistances varying between 400 Ω and 800 Ω. (e) 4-point I-V and the corresponding R-I plot of the central CrO$_2$ wire without interface. (f) Resistance vs temperature plot of the device between 10 K and 2 K shows the resistance fluctuating around ∼ 6.16 Ω.

the resistances were roughly 180 Ω, 300 Ω, 250 Ω and 570 Ω, respectively. We can also calculate the resistance-area product (RA) for these interfaces. From the cross

sectional area of 512×65 nm^2 and interface resistance of 180 Ω, we find an RA of 0.6×10^{-13} Ω.m^2. Similar to the observation on earlier devices, we found a large local variation in resistance among each of the interfaces.

Next, we measured the 4-point I-V and R-I curves (see Fig. 6.5(d)) for the central CrO$_2$ wire at 2 K. We found that the wire showed typical ohmic characteristics. Finally, we took the resistance vs temperature measurement of the CrO$_2$ wire between 10 K and 2 K. As expected, a proximity effect was not observed. Instead we found that the resistance fluctuated around 6 Ω after the superconducting transition at 6.5 K. Similar to the above junction device, we measured many (> 50) devices but the interface transparency issue remained unresolved. The earlier studies on proximity effect reported the interface resistance to be around 20 Ω [25]. However, we were not able to fabricate a device with such a low contact resistance, mostly because of the above-mentioned local variation in resistance.

Based on the above observations, we can certainly conclude that the large heterogeneity in resistance not only between the devices etched from same duration but also in the interface resistances of contact leads and CrO$_2$ wire separated by few hundreds of nm within a single device, limits the precise control required to fabricate a device with a defined resistance. Additionally, the growth of CrO$_2$ wires based on chemical vapor deposition limits the control of the final shape of the wire in the sense that the top surface of wire is not very flat. Instead we found surface roughness of about 10 nm along the width of the wire when measuring the topography with atomic force microscopy (see Appendix Fig. 6.7). This roughness in turn hinders with control of the etching process of CrO$_2$ and reliable metallic connection of contact electrodes with high interface transparency, a critical requirement for these junctions.

6.4. CrO$_2$ junctions fabricated with RuO$_2$

The lack of control with etching and difficulty to achieve a low interface resistance on our junctions required us to find another approach of fabrication. This is where RuO$_2$ emerged as a choice of material. The main advantage is that it is a metal, inert in ambient conditions and it can also be grown epitaxially in situ with CrO$_2$ via CVD due to similar lattice parameters. Further details of growth of RuO$_2$ can be found in sec. 5.2 In this section, we present the results of measurements conducted on one of the CrO$_2$/RuO$_2$ junction device.

Fig. 6.6 (a) shows the false colored SEM image of CrO$_2$/RuO$_2$ wire (green) of width around 500 nm and four Ni/MoGe contact leads. The two inner contact leads are laterally edge to edge separated by ~300 nm. Next, one of the contact lead,

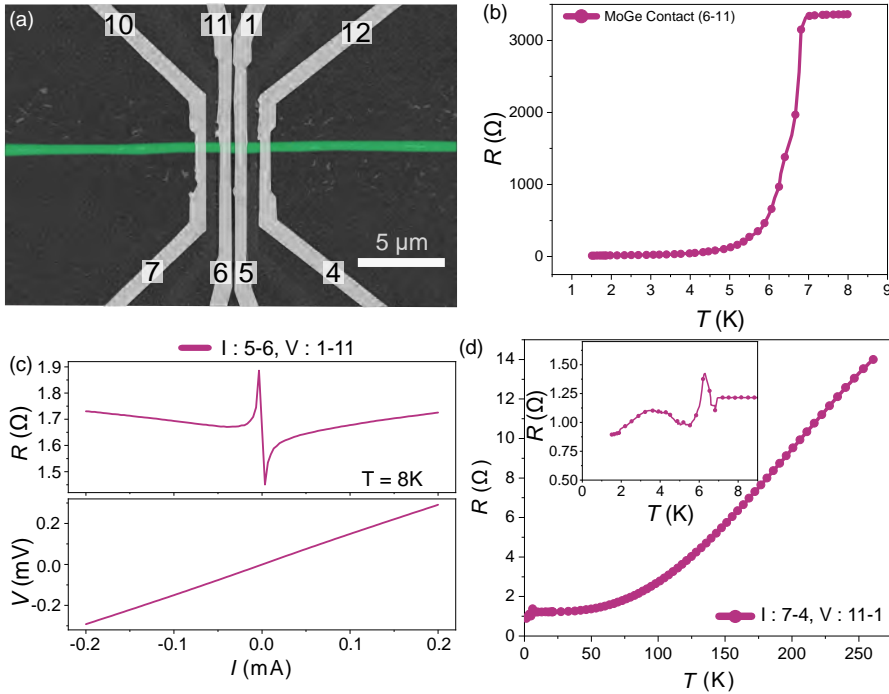Figure 6.6: (a) SEM image (false color) of a CrO$_2$/RuO$_2$ junction fabricated using the second approach where RuO$_2$ was grown in situ on top of CrO$_2$ wire, followed by deposition of contact leads comprising Ni/MoGe. The two inner contacts are laterally edge-to-edge separated by ~ 300 nm. (b) 2-point resistance vs temperature plot of contact lead 6-11 shows a superconducting transition (T_c) at T_c of ~ 6.5 K. (c) Quasi 4-point I-V and corresponding R-I plot of the central CrO$_2$/RuO$_2$ wire and the two interfaces measured at 8 K before T_c. (d) $R(T)$ plot of the junction measured between 250 K and 1.5 K. The inset shows a small upturn and then a dip in the resistance near T_c of the contact leads. Below T_c the resistance fluctuates around 1 Ω up to 1.5 K.

6-11 was measured in a 2-probe configuration to observe the T_c. Fig. 6.6 (b) shows typical T_c of around 6.5 K. After that, we measured I-V and the corresponding R-I plot (Fig. 6.6(c)) of the central CrO$_2$/RuO$_2$ wire and the two interfaces at 8 K. We observed a low resistance value of around ~ 1.7 Ω and a good ohmic behavior from R-I plot, indicating the transparent nature of the interface. Finally we measured $R(T)$ of the junction in 4-point geometry between 270 K and 1.5 K (Fig. 6.6(d)). We observed that the resistance of the device became constant below 10 K (inset), with a values of 1.214 Ω at 7.5 K. When the MoGe contact leads became superconducting at 6.5 K, the resistance started to fall again (after a small dip-peak excursion) but did not reach 0 Ω, indicating that the CrO$_2$ wire did not proximize completely over the length of the junction. Instead, we observed that the resistance reduced to 0.953 Ω at 2 K, which was nearly 20% decrement from the normal state resistance (R_N) at

7.5 K. This roughly translates to a proximity length of about 30 nm extending from contact leads on either side.

Further investigation into similar junctions fabricated with RuO_2 on top of CrO_2 revealed that the total height of the central CrO_2RuO_2 wire stack is around 150 nm to 180 nm. From our experience with growing CrO_2 for similar duration of time we can safely assume that the thickness of the CrO_2 wire would be ≤ 100 nm. This would mean that the thickness of RuO_2 is ≥ 50 nm. Both CrO_2 and RuO_2 are good metal and have comparable low residual resistance below 10 K. Since the thickness of RuO_2 is quite close to the thickness of the CrO_2 wire, the current would flow through both the materials. However, we know that RuO_2 is a weak antiferromagnet with a short coherence length of around 12 nm (see sec. 5.4). This would hamper the observation of long range proximity effect in these junctions. Ideally, we want to deposit a thin layer (~ 5 nm) of RuO_2 on top of CrO_2 so that maximum current flows through CrO_2. We found that the rate of growth of RuO_2 when growing above CrO_2 layer was very high. Even a growth for ~ 5 s leads to a thick layer of RuO_2 around (50-80) nm. We tried to change the growth parameters by changing the temperature, oxygen pressure but we did not get the desired outcome. Further investigation into the growth conditions is required to obtain thin RuO_2 wires.

6.5. Summary and Outlook

In summary, CrO_2 based lateral Josephson junctions were fabricated using two different approaches. The first method involved the etching of the top surface of CrO_2 to remove insulating layer of Cr_2O_3. Following this, a stack of Ag/Ni/MoGe contacts was deposited. This method of fabrication demanded a significant level of precision and control throughout various stages, posing challenges in achieving the desired outcomes. Significant resistance variations observed across multiple measurements, without any parameter modifications, indicate a lack of reproducibility. This lack of consistency poses challenges in conducting systematic investigations on the junctions.

The second approach of fabrication using RuO_2 as a spacer layer demonstrate initial potential. The measured devices exhibited high degree of transparency in the interfaces, with interface resistance being as low as 1 Ω. However, the thickness of RuO_2 layer remained a significant concern as it plays a crucial role in the observation of the long-range proximity effect in these devices. Additional research is required to achieve successful control of the growth of thin layer of RuO_2 on top of CrO_2 surface.

6.6. Appendix

6.6.1. AFM image of CrO$_2$ wire after CVD growth
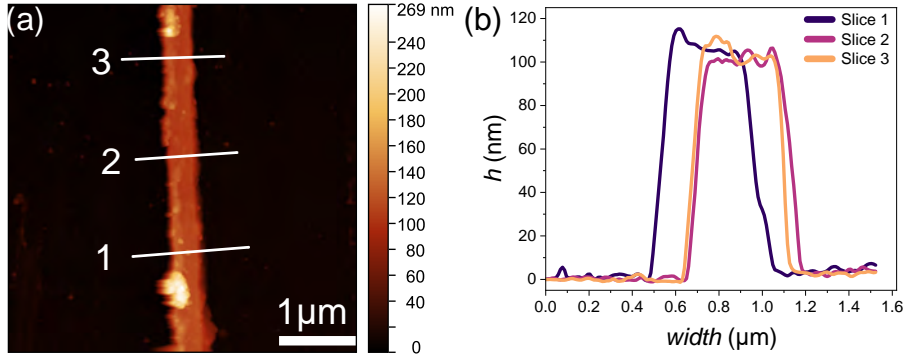

Figure 6.7: (a) Atomic force microscope image of the topography of a CrO$_2$ wire after CVD growth over an area of 5 X 5 μm^2. 3 slices were taken at random over a cross-section of the wire. (b)Corresponding height profiles of the 3 slices show the uneven top surface of the wire. The maximum roughness is around ∼ 14 nm.

The growth of CrO$_2$ wires using chemical vapor deposition (CVD) has limitations in controlling the ultimate wire shape, in contrast to alternative deposition processes like as sputtering and evaporation. These procedures allow for layer-by-layer deposition, often resulting in the formation of very smooth and flat films. Fig. 6.7(a) gives the atomic force microscope image of the topography of a CrO$_2$ wire of width (w) ≈ 500 nm. We took slices at three different positions on the wire (labeled 1, 2 and 3) and found that the top surface of the wire reveals a lack of flatness. Upon examination, a surface roughness of about 10 nm was detected over the width of the wire, as seen in the line profile of the three slices (Figure 6.7(b)). The presence of surface roughness poses a challenge to the precise control of the etching process of CrO$_2$ and the establishment of reliable metallic connections between contact electrodes, while maintaining a high level of interface transparency. This need is a critical requirement for the successful fabrication of these junctions.

References

[1] Bergeret, F. S., Volkov, A. F. & Efetov, K. B. Long-Range Proximity Effects in Superconductor-Ferromagnet Structures. Phys. Rev. Lett. **86**, 4096–4099 (2001). URL https://link.aps.org/doi/10.1103/PhysRevLett.86.4096.

[2] Bergeret, F. S., Volkov, A. F. & Efetov, K. B. Odd triplet superconductivity and related phenomena in superconductor-ferromagnet structures. Rev. Mod. Phys. **77**, 1321–1373 (2005). URL https://link.aps.org/doi/10.1103/RevModPhys.77.1321.

[3] Keizer, R. S. et al. A spin triplet supercurrent through the half-metallic ferromagnet CrO_2. Nature **439**, 825–827 (2006). URL https://doi.org/10.1038/nature04499.

[4] Khaire, T. S., Khasawneh, M. A., Pratt, W. P. & Birge, N. O. Observation of Spin-Triplet Superconductivity in Co-based Josephson Junctions. Phys. Rev. Lett. **104**, 137002 (2010). URL https://link.aps.org/doi/10.1103/PhysRevLett.104.137002.

[5] Robinson, J. W. A., Witt, J. D. S. & Blamire, M. G. Controlled Injection of Spin-Triplet Supercurrents into a Strong Ferromagnet. Science **329**, 59–61 (2010). URL https://www.science.org/doi/abs/10.1126/science.1189246. https://www.science.org/doi/pdf/10.1126/science.1189246.

[6] Robinson, J. W. A., Halász, G. B., Buzdin, A. I. & Blamire, M. G. Enhanced Supercurrents in Josephson Junctions Containing Nonparallel Ferromagnetic Domains. Phys. Rev. Lett. **104**, 207001 (2010). URL https://link.aps.org/doi/10.1103/PhysRevLett.104.207001.

[7] Leksin, P. V. et al. Evidence for Triplet Superconductivity in a Superconductor-Ferromagnet Spin Valve. Phys. Rev. Lett. **109**, 057005 (2012). URL https://link.aps.org/doi/10.1103/PhysRevLett.109.057005.

[8] Witt, J. D. S., Robinson, J. W. A. & Blamire, M. G. Josephson junctions incorporating a conical magnetic holmium interlayer. Phys. Rev. B **85**, 184526 (2012). URL https://link.aps.org/doi/10.1103/PhysRevB.85.184526.

[9] Wang, Y., Pratt, W. P. & Birge, N. O. Area-dependence of spin-triplet supercurrent in ferromagnetic Josephson junctions. Phys. Rev. B **85**, 214522 (2012). URL https://link.aps.org/doi/10.1103/PhysRevB.85.214522.

[10] Robinson, J. W. A., Chiodi, F, Egilmez, M., Halász, G. B. & Blamire, M. G. Supercurrent enhancement in Bloch domain walls. Scientific Reports **2**, 699 (2012). URL https://doi.org/10.1038/srep00699.

[11] Sprungmann, D., Westerholt, K., Zabel, H., Weides, M. & Kohlstedt, H. Evidence for triplet superconductivity in Josephson junctions with barriers of the ferromagnetic Heusler alloy Cu_2MnAl. Phys. Rev. B **82**, 060505 (2010). URL https://link.aps.org/doi/10.1103/PhysRevB.82.060505.

[12] Anwar, M. S., Czeschka, F., Hesselberth, M., Porcu, M. & Aarts, J. Long-range supercurrents through half-metallic ferromagnetic CrO_2. Phys. Rev. B **82**, 100501 (2010). URL https://link.aps.org/doi/10.1103/PhysRevB.82.100501.

[13] Wang, J. et al. Interplay between superconductivity and ferromagnetism in crystalline nanowires. Nature Physics **6**, 389–394 (2010). URL https://doi.org/10.1038/nphys1621.

[14] Anwar, M. S., Veldhorst, M., Brinkman, A. & Aarts, J. Long range supercurrents in ferromagnetic CrO_2 using a multilayer contact structure. Applied Physics Letters **100**, 052602 (2012). URL https://doi.org/10.1063/1.3681138.

[15] Jiang, J. et al. Long-range superconducting proximity effect in nickel nanowires. Phys. Rev. Res. **4**, 023133 (2022). URL https://link.aps.org/doi/10.1103/PhysRevResearch.4.023133.

[16] Houzet, M. & Buzdin, A. I. Long range triplet josephson effect through a ferromagnetic trilayer. Physical Review B **76**, 060504 (2007).

[17] Halterman, K., Valls, O. T. & Barsic, P. H. Induced triplet pairing in clean s-wave superconductor/ferromagnet layered structures. Phys. Rev. B **77**, 174511 (2008). URL https://link.aps.org/doi/10.1103/PhysRevB.77.174511.

[18] Fominov, Y. V., Volkov, A. F. & Efetov, K. B. Josephson effect due to the long-range odd-frequency triplet superconductivity in SFS junctions with néel domain walls. Phys. Rev. B **75**, 104509 (2007). URL https://link.aps.org/doi/10.1103/PhysRevB.75.104509.

[19] Volkov, A. F. & Efetov, K. B. Odd triplet superconductivity in a superconductor/ferromagnet structure with a narrow domain wall. Phys. Rev. B **78**, 024519 (2008). URL https://link.aps.org/doi/10.1103/PhysRevB.78.024519.

[20] Buzdin, A. I., Mel'nikov, A. S. & Pugach, N. G. Domain walls and long-range triplet correlations in sfs josephson junctions. Phys. Rev. B **83**, 144515 (2011). URL https://link.aps.org/doi/10.1103/PhysRevB.83.144515.

[21] Eschrig, M. & Löfwander, T. Triplet supercurrents in clean and disordered half-metallic ferromagnets. Nature Physics **4**, 138–143 (2008). URL https://doi.org/10.1038/nphys831.

[22] Linder, J., Yokoyama, T. & Sudbø, A. Theory of superconducting and magnetic proximity effect in s/f structures with inhomogeneous magnetization textures and spin-active interfaces. Phys. Rev. B **79**, 054523 (2009). URL https://link.aps.org/doi/10.1103/PhysRevB.79.054523.

[23] Robinson, J. W. A., Samokhvalov, A. V. & Buzdin, A. I. Chirality-controlled spontaneous currents in spin-orbit coupled superconducting rings. Phys. Rev. B **99**, 180501 (2019). URL https://link.aps.org/doi/10.1103/PhysRevB.99.180501.

[24] Ando, F. et al. Observation of superconducting diode effect. Nature **584**, 373–376 (2020). URL https://doi.org/10.1038/s41586-020-2590-4.

[25] Singh, A., Jansen, C., Lahabi, K. & Aarts, J. High-Quality CrO_2 Nanowires for Dissipation-less Spintronics. Physical Review X **6**, 041012 (2016).

[26] Dai, J. et al. Characterization of the natural barriers of intergranular tunnel junctions: Cr_2O_3 surface layers on CrO_2 nanoparticles. Applied Physics Letters **77**, 2840–2842 (2000). URL https://doi.org/10.1063/1.1320845. https://pubs.aip.org/aip/apl/article-pdf/77/18/2840/10185525/2840_1_online.pdf.

[27] Cheng, R. et al. Characterization of the native Cr_2O_3 oxide surface of CrO_2. Applied Physics Letters **79**, 3122–3124 (2001). URL https://doi.org/10.1063/1.1416474. https://pubs.aip.org/aip/apl/article-pdf/79/19/3122/10190307/3122_1_online.pdf.

[28] Cheng, R. et al. Oxidation of metals at the chromium oxide interface. Applied Physics Letters **81**, 2109–2111 (2002). URL https://doi.org/10.1063/1.1506942.

Summary

CrO_2, a half-metal ferromagnet, has shown great promise for superconducting spintronics applications for nearly two decades. Josephson junctions consisting of superconducting (S) contacts on ferromagnetic (F) structures of CrO_2, have been shown to sustain remarkably high supercurrents (of the order of 10^{10} A/m^2) over hundreds of nanometers. However, advancements in this area have been hindered by the metastable nature of CrO_2 at ambient conditions. This results in a poorly controlled S-F interface transparency, which is critical for generation of spin triplets. This thesis explores the potential, challenges and possible solutions to overcome the issues with CrO_2 devices.

After an introduction of the subject matter in Chapter 2, in Chapter 3 we study the growth of high quality epitaxial CrO_2 wires on a TiO_2 substrate using Selective Area method via chemical vapor deposition. We focused on the wires grown along [001] c-axis and [010] b-axis of the substrate, which are the magnetically easy and hard axis of the wire, respectively. We investigated the morphology of the wires by high-resolution transmission electron microscopy (TEM) and measured their physical properties, in particular magnetoresistance (MR) and the Anomalous Hall Effect (AHE). TEM images showed that the morphology of the wires grown along the two axes is very different. For c-axis grown wires (the easy wires), the bulk of the CrO_2 grows epitaxially on the TiO_2 substrate, but some small regions near interface of TiO_2 and CrO_2 have a different crystal orientation than the TiO_2 substrate. The b-axis grown wire (the hard wire) has many crystal domains that are all rotated with respect to each other at specific angles. MR data show very sharp switching for the easy axis wires, even for quite large wire widths. In comparison, MR on hard wires reveal a dependence on the width. The AHE is found to be different for c-axis wires and b-axis wires, contradictory to the bars etched in films by Ar-ion etching. We argue this to be due to a different wire morphology on the nanoscale.

In Chapter 4, we investigate the pinning and depinning of a magnetic domain wall (DW), meaning the finite-volume interface separating two domains with different magnetization direction, in a nanowire, using using a triangular constriction (notch) in two ferromagnets. One is Permalloy (Py), which is used as a reference material, the other is CrO_2, to study a fully spin-polarized material. We designed a high

frequency setup to allow injection of current pulses to assist in depinning of the DW. We find that in general, the notch size affects the critical depinning current density (J_c). While a deep notch (> 50% of the wire width) increases the DW resistance, it also leads to a strong pinning potential for both Py and CrO_2 devices, which makes depinning difficult. Furthermore, and not surprisingly, we observe that CrO_2 devices are more sensitive to the notch depth, with a 5% deeper notch on a wire of similar size resulting in a 2.5 times higher J_c. The depinning critical current densities in CrO_2 are of the order of 10^{12} A/m^2 which is comparable to that of Py devices. It suggests that the high spin polarization does not necessarily lower J_c, contrary to some predictions. Additionally, we measured the domain wall resistance (DWR) and calculated its corresponding resistance-area product (RA_{DW}) in CrO_2. We found the DWR to decrease from 25 mΩ corresponding to RA_{DW} of 1.4×10^{-16} Ωm^2 at 10 K to 18.2 mΩ corresponding to RA_{DW} of 0.99×10^{-16} Ωm^2 at 80 K, then rise to roughly 23 mΩ at 300 K. The rise in DWR above 80 K could be attributed to spin disorder dominating over spin scattering which may be connected to the appearance of skyrmion-like topological defects in the magnetic state of CrO_2. The values of RA_{DW} are similar to the values reported for nanostructures of (La,Sr)MnO$_3$, another halfmetallic ferromagnet, and also similar to other conventional ferromagnets like Co and Py, suggesting that full spin polarization does not significantly change the values for DWRs.

In Chapter 5, we used a selective area chemical vapor deposition method to grow nanowires of RuO$_2$ on TiO$_2$ substrates, similar to CrO_2 wires growth. Subsequently, we characterize these RuO$_2$ nanowires through electrical and magnetotransport measurements. The Hall measurements indicate electron-like charge carriers and, interestingly, the charge carrier density decreases with temperature, which is unusual. Then we focus on making Josephson junctions (JJ) by depositing superconducting MoGe on top of RuO$_2$ nanowires, and making lateral gaps of varying size with a Focused Ion Beam. We find that such devices show a clear critical current, as well as a Fraunhofer-like damped oscillatory response to a magnetic field, for distances between the contacts below 70 nm. Such small distances point to pair breaking effects that are larger than expected for a normal metal. Rather, they are similar to what is found in weak ferromagnets. We estimate the induced singlet coherence length ξ to be about 12 nm, which seems a reasonable number when small magnetic moments are present.

As mentioned, CrO_2 holds great potential for superconducting spintronics but its reduction into insulating Cr_2O_3 at ambient temperatures makes the fabrication of Jospehson junction to show long range proximity effect difficult. In Chapter 6, we discuss the fabrication of CrO_2 junctions with two distinct methods to address this issue. The first method involves removing the Cr_2O_3 layer by standard

Ar-etching of the top surface of CrO_2. We evaluated the impact of etching on interface transparency in many (> 50) devices and observed a very wide spread of interface resistances for the same etch parameters, indicating lack of control and the consistency required to observe the desired effects. The second approach employs a protective layer of RuO_2 which was grown *in situ* with CrO_2 in CVD with customized arrangements. The RuO_2 layer results in low contact resistances of around 1 Ω. However, with our growth method, we found the thickness of RuO_2 to be above 50 nm for a very short growth time of 5 sec. Due to its short coherence length of 12 nm, the considerable thickness of RuO_2 prevents inducing long range proximity-induces supercurrents in these devices. Further optimization of growth settings is needed to attain the target thickness of around 5 nm.

Samenvatting

CrO$_2$, een halfmetallische ferromagneet, is al bijna twee decennia lang veelbelovend voor supergeleidende spintronica-toepassingen. Josephson-juncties gebaseerd op CrO$_2$, bestaande uit supergeleidende (S) contacten op ferromagnetische (F) structuren van CrO$_2$, hebben opmerkelijk hoge superstromen laten zien, van de orde van 10^{10} A/m^2 over honderden nanometers. De ontwikkelingen op dit gebied zijn echter belemmerd door de metastabiele aard van CrO$_2$ bij kamertemperatuur. Dit resulteert in een slecht gecontroleerde transparantie van het S/F-interface, die cruciaal is voor de generatie van de benodigde spin triplet paren. Dit proefschrift verkent het potentieel, de uitdagingen en mogelijke oplossingen om de problemen met CrO$_2$-devices aan te pakken.

Na een inleiding van het onderwerp in Hoofdstuk 2, bestuderen we in Hoofdstuk 3 de groei van hoogwaardige epitaxiale CrO$_2$-draden op een TiO$_2$-substraat met behulp van de Selective Area methode, gebaseerd op chemische dampafzetting. We hebben ons gericht op de draden die groeien langs de [001] c-as en [010] b-as van het substraat, respectievelijk de magnetisch gemakkelijke en moeilijke as van de draad. We hebben de morfologie van de draden onderzocht met behulp van transmissie-elektronenmicroscopie (TEM) met hoge resolutie, en ook hun fysische eigenschappen gemeten, met name de magnetoweerstand (MR) en het Anomale Hall Effect (AHE). TEM-beelden toonden aan dat de morfologie van de draden die langs de twee assen groeien zeer verschillend is. Voor draden die groeien langs de c-as (de 'gemakkelijke' draden), groeit het grootste deel van het CrO$_2$ epitaxiaal op het TiO$_2$-substraat, maar sommige kleine regio's in de buurt van het interface van TiO$_2$ en CrO$_2$ hebben een andere kristaloriëntatie dan het TiO$_2$-substraat. De draad die langs de b-as groeit (de 'harde' draad) heeft veel kristalgebieden die allemaal ten opzichte van elkaar zijn geroteerd onder specifieke hoeken. MR-gegevens tonen dat de magnetisatie van de draden langs de gemakkelijke as zeer scherp schakelt, zelfs voor vrij grote draadbreedtes. In vergelijking hiermee laten MR-gegevens voor harde draden een afhankelijkheid van de breedte zien. Het AHE is verschillend voor de c-as draden en b-as draden, in tegenstelling tot balkjes geëtst in films met behulp van Ar-ionenetsen. We suggereren dat dit te wijten is aan een verschillende draadmorfologie op nanoschaal.

In Hoofdstuk 4 onderzoeken we het vasthouden ('pinnen') en loslaten ('depinnen') van een magnetische domeinwand (DW) in een nanodraad. De DW, een eindig-volume interface dat twee domeinen met verschillende magnetisatierichtingen scheidt, wordt daarvoor aangebracht in een driehoekige vernauwing (inkeping) in twee ferromagneten. De ene is Permalloy, dat wordt gebruikt als referentiemateriaal, de andere is CrO_2, om een volledig spin-gepolariseerd materiaal te bestuderen. We hebben een opstelling ontworpen voor de injectie van hoog-frequent stroom-pulsen om de DW te depinnen. Over het algemeen blijkt dat de grootte van de inkeping de kritische stroomdichtheid J_c voor het depinnen beïnvloedt. Een diepe inkeping (> 50% van de draadbreedte) verhoogt de weerstand van de DW, maar leidt ook tot een sterke DW verankering in zowel Py- als CrO_2-draden, wat de-pinnen moeilijk maakt. Bovendien blijken CrO_2-devices gevoeliger te zijn voor de diepte van de inkeping, waarbij een inkeping die 5% dieper is, in een draad van vergelijkbare grootte resulteert in een J_c die 2,5 keer hoger is. De kritische depinning-stroomdichtheden in CrO_2 zijn van dezelfde orde van grootte als die in Py devices. Dit suggereert dat de hoge spin-polarisatie J_c niet noodzakelijker-wijs verlaagt, in tegenstelling tot sommige voorspellingen. Verder maten we de weerstand van de domeinwand (DWR) in CrO_2 en bepaalden het bijbehorende weerstand-oppervlakte product RA_{DW}. We vinden we dat de DWR afneemt van 25 mΩ (corresponderend met een RA_{DW} van 1.4×10^{-16} Ωm^2) bij 10 K tot 18,2 mΩ (0.99×10^{-16} Ωm^2) bij 80 K, om vervolgens weer toe te nemen tot ongeveer 23 mΩ bij 300 K. De stijging van de DWR boven 80 K kan worden toegeschreven aan spin-wanorde die de overhand heeft over spinverstrooiing, wat mogelijk verband houdt met het verschijnen van skyrmion-achtige topologische defecten in de magnetis-che toestand van CrO_2. De waardes van RA_{DW} zijn vergelijkbaar met de waardes gevonden voor nanostructuren van $(La,Sr)MnO_3$, een andere halfmetallische ferro-magneet, maar ook met die van conventionele ferromagneten zoals Co en Py, wat suggereeert dat volledige spinpolarizatie geen andere waardes geeft voor de DWR.

In Hoofdstuk 5 hebben we de Selective Area Chemical Vapor Deposition-methode gebruikt om nanodraden van RuO2 op TiO_2-substraten te laten groeien, vergelijk-baar met de groei van CrO_2-draden. Vervolgens karakteriseren we deze RuO2-nanodraden door middel van elektrische en magnetotransportmetingen. De Hall-metingen wijzen op elektronachtige ladingdragers en interessant genoeg neemt de dichtheid van de ladingdragers af met de temperatuur, wat ongebruikelijk is. Vervolgens richten we ons op het maken van Josephson-juncties (JJ) door supergelei-dend MoGe op RuO2-nanodraden te deponeren en laterale spleten van variërende grootte te maken met behulp van een Focused Ion Beam. Dergelijke devices ver-tonen een duidelijke kritische stroom, evenals een Fraunhofer-achtige gedempte oscillerende respons op een magnetisch veld, voor afstanden tussen de contacten onder de 70 nm. Deze kleine afstanden wijzen op paarbrekingseffecten die groter

zijn dan verwacht voor een normaal metaal. Ze zijn eerder vergelijkbaar met wat wordt gevonden in zwakke ferromagneten. We schatten de geïnduceerde singlet-coherentielengte ξ op ongeveer 12 nm, wat een redelijke waarde lijkt te zijn wanneer kleine magnetische momenten aanwezig zijn.

Zoals eerder vermeld, heeft CrO_2 veel potentieel voor supergeleidende spintronica, maar de omzetting naar isolerend Cr_2O_3 bij kamertemperatuur maakt de fabricage van Josephson juncties met een lange bereikproxiemethode moeilijk. In Hoofdstuk 6 bespreken we de fabricage van CrO_2-juncties met twee verschillende methoden om dit probleem aan te pakken. De eerste methode omvat het verwijderen van de Cr_2O_3-laag door standaard Ar-etsen van het bovenoppervlak van CrO_2. We hebben de impact van etsen op de interfacetransparantie geëvalueerd in veel (> 50) devices en hebben een zeer brede spreiding van interfaceweerstanden voor dezelfde etsparameters waargenomen, wat duidt op gebrek aan controle en consistentie die nodig is om de gewenste effecten waar te nemen. De tweede benadering maakt gebruik van een beschermende laag RuO_2, die in situ is gegroeid met CrO_2 in CVD met aangepaste opstellingen. De RuO_2-laag resulteert in lage contactweerstanden van ongeveer 1 Ω. Met onze groeimethode hebben we echter gevonden dat de dikte van RuO_2 boven de 50 nm ligt voor een zeer korte groeitijd van 5 sec. Vanwege de korte coherentielengtetijd van 12 nm voorkomt de grote dikte van RuO2 het bereiken van de lange-dracht proximity-geïnduceerde superstromen in deze devices. Verdere optimalisatie van de groeiparameters is nodig om de beoogde dikte van ongeveer 5 nm te bereiken.

List of Publications

- C. Yin, **K. Prateek**, W. Gelling and J. Aarts. Tunable Magnetic Scattering Effects at the $LaAlO_3$/$SrTiO_3$ Interface by Ionic Liquid Gating, *ACS Applied Electronic Materials* **2** (12), 3837-3842 (2020).

- **K. Prateek**, M. Bolhuis, A.B. Hamida, D. Scholma, S. C. Boj and J. Aarts. Magnetotransport properties of CrO_2 nanowires fabricated by Selective Area growth, *Journal of Physics and Chemistry of Solids* **178**, 111350 (2023).

- J. Yao, **K. Prateek**, M. Cabero-Piris and J. Aarts. Non-local Spin Transport based on a Half-metallic Ferromagnet, *Phys. Rev. Materials* **7**, 104408 (2023).

- **K. Prateek**, T. Mechielsen, A.B. Hamida, D. Scholma and J. Aarts. Fabrication and properties of lateral Josephson junctions with a RuO_2 weak link, *under review*.

CurriculumVitae

Kumar Prateek

Education

2005-09	SASTRA University
	BTech. in Electronics and Instrumentation Engineering
	Thesis: Monitor & Control of interdependent parameters using Fuzzy Logic Controller
	Supervisor: Dr. N. A. Kumar
2012-14	Leuven University and T.U. Dresden
	Erasmus Mundus Masters in Nanoscience and Nanotechnology
	Thesis: Aharonov-Bohm oscillations in a 3D long-perimeter Bi_2Te_3 nanowire
	Supervisor: Dr. R. Giraud
2017-23	Leiden University
	PhD in Physics
	Thesis: Towards Superconducting Spintronics with RuO_2 and CrO_2 nanowires
	Supervisor: Prof.dr. J. Aarts

Professional Experience

2009-12	Tata Consultancy Services, India
	Systems Engineer
2014-16	Robotics Core School, India
	Electronics Engineer

Acknowledgements

This thesis could not have been completed without the support of many people during my PhD time. First and foremost, I would like to express my sincere gratitude to Jan Aarts, my promoter, for giving me the opportunity to join his group and further my academic pursuits. I am deeply thankful of his unwavering guidance and support in spite of his extremely hectic schedule. I greatly value the extensive knowledge and comprehensive overview of physics that he graciously shared with compassion and modesty.

I would like to thank Sonia Conesa-Boj and Maarten Bolhuis, my collaborators at Delft, for the TEM measurements on the CrO_2 nanowires. I appreciate the insightful and stimulating discussions we had while writing the paper. I want to thank Aymen Ben Hamida, with whom I worked closely on most of the projects. I am thankful for his continuous mentorship and support, encompassing our numerous discussions and teaching me the intricacies of systematic measurement. My sincere thanks to Nikita Lebedev for acquainting me with PPMS and subsequently assisting me with the configuration for the pulse measurements. Douwe Scholma and Thomas Mechielsen deserve special recognition for their assistance with the fabrication process and discussions pertaining to CrO_2 and RuO_2 projects. I am grateful for their nearly instantaneous technical assistance, despite their packed schedule.

I am indebted to Marcel Hesselberth for his invaluable guidance and technical assistance. I could always count on him for solving the issues with ebeam lithography and evaporator. I want to thank and appreciate the technical support from Federica Galli for introducing me to AFM lab; Christian Penn and Ruud van Egmond from fine mechanical department for CVD setup; Peter van Veldhuizen of Electronics department who was consistently accessible to assist in resolving numerous PPMS issues and designing the high frequency pulse measurement setup. I express my gratitude to Danielle Duijn for her assistance pertaining to day to day administrative affairs.

I want to thank the former students Brecht Simon, Amber Zitman who made contributions to my research. I also want to thank all the current and former members of LION and MSM group: including Amrita Singh, Tamer Karaman, Chunhai Yin,